NONAQUEOUS ELECTROKINETIC TRANSPORT IN CHARGED POROUS MEDIA THEORY AND EXPERIMENTS

By

CHRISTOFOROS C. CHRISTOFOROU

A DISSERTATION PRESENTED TO THE GRADUATE SCHOOL
OF THE UNIVERSITY OF FLORIDA IN
PARTIAL FULFILLMENT OF THE REQUIREMENTS
FOR THE DEGREE OF DOCTOR OF PHILOSOPHY

UNIVERSITY OF FLORIDA

1985

ACKNOWLEDGEMENTS

I would like to express my sincere gratitude and thanks to Dr. G. B. Westermann-Clark for his guidance and encouragement during the course of this research. His accessibility and enthusiasm accelerated the work presented at every stage. Working with him has been a truly valuable and enjoyable experience.

I am grateful to Dr. D. O. Shah for chairing my supervisory committee, and for letting me use his word-processing equipment. I would like to thank Drs. J. P. O'Connell and T. E. Hogen Esch for serving on my supervisory committee, and Drs. T. J. Anderson and G. M. Schmid for their presence in my defense exam. I would also like to thank Mrs. Derbra Owete for her excellent technical typing.

Finally, I wish to acknowledge the financial support provided by the University of Florida and the National Science Foundation (Research Initiation Grant number CPE-8205076).

TABLE OF CONTENTS

Page

ACKNOWLEDGEMENTS ii

LIST OF TABLES v

KEY TO SYMBOLS vi

ABSTRACT ix

CHAPTER 1 INTRODUCTION 1

CHAPTER 2 MATHEMATICAL MODEL 6
- 2.1 Previous Work 6
- 2.2 Model Assumptions and Equations 8
- 2.3 Approximate Solutions to the Model Equations 12
- 2.4 Calculation of Fluxes Through the Pore 14
- 2.5 Calculation of Electrokinetic Parameters 16

CHAPTER 3 THE EXCLUSION-DIFFUSION POTENTIAL IN CHARGED MICROPOROUS MEMBRANES 20
- 3.1 Introduction 20
- 3.2 Models for the Exclusion-Diffusion Potential 23
- 3.3 Comparison of the Meyer-Sievers and the Space-Charge Models 30
- 3.4 Conclusions 41

CHAPTER 4 THE ENHANCED PORE FLUID CONDUCTIVITY IN CHARGED MICROPOROUS MEMBRANES 43
- 4.1 Introduction 43
- 4.2 Approximate Solutions of the Model Equations 47
- 4.3 Work by Others 50
- 4.4 Results and Discussion 53
- 4.5 Conclusions 69

CHAPTER 5 THE STREAMING POTENTIAL AND INADEQUACIES OF THE HELMHOLTZ EQUATION 71
- 5.1 Introduction 71
- 5.2 Approximate Solutions of the Model Equations 76
- 5.3 Comparison of Approximate Solutions 80
- 5.4 Conclusions 86

CHAPTER 6 EXPERIMENTS 88
6.1 Introduction 88
6.2 Apparatus 89
6.3 Experiments to Test the Model 93
6.4 Results of Preliminary Nonaqueous Electrokinetic Experiments 99

CHAPTER 7 EXPERIMENTAL INVESTIGATION OF THE SPACE-CHARGE MODEL IN NONAQUEOUS SOLVENTS 109
7.1 Introduction 109
7.2 Mica Wall Characterization 110
7.3 Nonaqueous Electrokinetic Experiments 121
7.4 Conclusions 140

CHAPTER 8 SUMMARY AND RECOMMENDATIONS 142

APPENDIX A NUMERICAL SOLUTION OF THE POISSON-BOLTZMANN EQUATION 152

APPENDIX B MODEL COEFFICIENTS 168

APPENDIX C APPROXIMATE SOLUTIONS TO THE POISSON-BOLTZMANN EQUATION IN CYLINDRICAL PORES 174

APPENDIX D MICA MEMBRANE PREPARATION 183

REFERENCES 187

BIOGRAPHICAL SKETCH 191

LIST OF TABLES

Page

Table 4-1 Constant Wall Charge Boundary Condition 57

Table 4-2 Constant Wall Potential Boundary Condition 58

Table 4-3 Comparison of the Ratio of Convection to Migration Terms 59

Table 7-1 Comparison of Calculated and Measured Streaming Currents 134

Table D-1 Membrane Irradiation and Etching Data 186

KEY TO SYMBOLS

a	equivalent pore radius (m)
A	fixed ionic concentration on pore (mol/dm^3)
$C_b(x)$	bulk concentration (mol/dm^3)
$C_i(r,x)$	concentration of species i inside pore (mol/dm^3)
d	half slit width (m)
D	Debye length, equation (2-1c), (m)
D_i	diffusion coefficient of i (m^2/sec)
d	half slit separation (m)
e	magnitude of charge on a proton (C)
I_x	current density through the pore (A/m^2)
I_s	streaming current (A/Pa)
J_s	solute flow through the pore (m^3/m^2)
k	Boltzmann constant (J/K)
ℓ	pore length (m)

L	characteristic pore cross sectional dimension, Chapter 2
n	number of pores on the membrane
N_i	flux of i (mol/m^{2}sec)
$P(x)$	equivalent bulk pressure (Pa)
q	solvent flow through the pore (m^3/m^2)
S_w	dimensionless pore surface charge
T	temperature (K)
U_i	absolute mobility of species i (m^{2}mol/Js)
$\underline{v}$	fluid velocity in pore (m/sec)
$V(x)$	electrical potential (V)
V_{ed}	exclusion-diffusion potential (V)
x	axial position in pore (m)
x_p	dimensionless pore cross sectional dimension
z_i	charge number of species i
ε	solvent dielectric constant
η	solvent viscosity (Pa.s)
κ	pore fluid conductivity (S/m)

κ_b	bulk fluid conductivity (S/m)
ν	streaming potential (V/Pa)
σ_w	pore wall surface charge density (C/m^2)
ϕ	total electrical potential in the pore (V)
ψ	electrostatic potential due to the charged wall (V)
Ψ	dimensionless potential due to the charged wall ($ze\psi/kT$)
$\Psi(1)$	dimensionless wall potential

Abstract of Dissertation Presented to the Graduate School
of the University of Florida in Partial Fulfillment of the
Requirements for the Degree of Doctor of Philosophy

NONAQUEOUS ELECTROKINETIC TRANSPORT IN CHARGED POROUS MEDIA THEORY AND EXPERIMENTS

By

Christoforos C. Christoforou

May, 1985

Chairman: Dr. D. O. Shah
Cochairman: Dr. G. B. Westermann-Clark
Major Department: Chemical Engineering

A mathematical model which describes electrokinetic transport across a charged porous medium is investigated. The model, called the space-charge model, uses the Nernst-Planck, Poisson-Boltzmann, and Navier-Stokes equations to describe the steady-state transport of ions, electrolyte, and solvent, through a charged capillary caused by electrolyte concentration, hydrostatic pressure, and electrical potential differences across the capillary. The pore size, the Debye length of the solution inside the capillary, and the pore wall charge density, or wall potential, must be known for the model equations to be solved. To overcome the numerical difficulties associated with the tedious numerical calculations required for the evaluation of the ionic fluxes through the porous medium, approximate solutions to the model equations are also presented.

The space-charge model predictions for three independent electrokinetic parameters, the exclusion-diffusion potential, pore fluid conductivity, and streaming potential, are examined and compared to other models in the literature. The space-charge model is shown to be superior in describing electrokinetic transport through charged porous media. Numerical solutions of the space-charge model are also compared to approximate analytical solutions in order to evaluate the range of applicability of these approximate solutions.

The model is also examined experimentally by comparing it with electrokinetic data in nonaqueous electrolyte solutions. Methanol solutions of LiCl were the nonaqueous medium used and track-etched mica membranes were the porous medium. The wall charge density of the mica membranes is shown to be stable as long as the electrolyte solution in contact with the pore wall has a pH greater than 7. The only unknown parameter for the model calculations is the pore wall charge density. Using wall charge densities from one electrokinetic experiment, the space-charge model is shown to be capable of predicting experimental results of other independent electrokinetic experiments. The good agreement between experiments and theory helps to confirm the correctness of the theory.

CHAPTER 1
INTRODUCTION

There is a large number of physical situations where a charged porous medium separates dilute salt solutions and where permeation of salt across the medium occurs. Examples include ion-exchange and ultrafiltration membranes, porous separators in electrolytic cells, and flow-through porous electrodes. In general, the salt solutions on each side of the porous medium are at different pressures, concentrations, and electrical potentials, and these differences result directly in solvent flow, solute diffusion, and electrical current, respectively. In addition, indirect coupling between driving forces for transport and fluxes often is observed, as in electrodialysis. This cross-coupling in charged porous media becomes increasingly important when the diffuse part of the double layer, caused by the charge on the pore walls, is large enough to occupy most of the pore volume.

The goal of the work presented in this dissertation is to investigate a model which describes the electrokinetic transport through a charged porous medium. The model, presented in Chapter 2, is called the space-charge model for electrokinetic transport here. The model uses the Nernst-Planck, Navier-Stokes, and Poisson-Boltzmann equations to predict ionic transport caused by pressure, electrolyte concentration, and electrical potential differences across a charged porous medium. The model can predict any electrokinetic effect in a medium whose charged pores are large enough to justify the use of continuum theory, as in the Nernst-Planck and Navier-Stokes equations. Other limitations of the model, detailed in Chapter 2, include the stipulation that the length of the pores be much larger than the pore radius, and that the electrolyte concentrations of the bulk solutions outside the porous medium are low. Finally, evaluation of the ionic fluxes through the porous medium using the space charge model requires somewhat tedious numerical calculations. To overcome this last problem approximate analytical solutions to the model predictions are also presented in Chapter 2.

The electrokinetic effects predicted by the model include the pore fluid conductivity, the exclusion-diffusion potential, the streaming potential, and the streaming current. These effects are introduced at the end of Chapter 2, and are only four among a number of effects that have been observed experimentally in the past and have appeared in the literature under various names (1). Briefly, these electrokinetic effects are caused by different driving forces across the porous medium. In a pore fluid conductivity experiment, an electrical current (or a potential) is applied across the porous medium and an electrical potential (or a current) is measured across the medium. The pore fluid conductivity can then be calculated using Ohm's law. The exclusion-diffusion potential is the electrical potential that develops across a porous medium when there are different electrolyte concentrations on each side of the porous medium. The streaming potential is the electrical potential that develops across the porous medium, while the streaming current is the electrical current that passes through the medium, when the electrolyte solutions on each side of the porous medium are at different pressures. The space-charge model predictions for the exclusion-diffusion potential, the pore fluid conductivity, and the streaming potential are analyzed and compared to predictions of other electrokinetic models in Chapters 3 to 5.

The space-charge model assumes that all the pores in the porous medium are identical. This assumption was valid for the track-etched mica membranes used as the porous medium in experiments. At large pore sizes, the pores in track-etched mica are 60^{0} rhombohedrons which go straight through the mica sheet. The number of pores and the radius of a circle with the same cross section as a rhombohedral pore in the membrane can be easily evaluated before the experiments start.

Chapter 6 describes the experimental apparatus and the method of preparing track-etched mica membranes. It also shows how the experimental data were taken and how they were compared to the space-charge model. Chapter 6 presents a set of preliminary electrokinetic experiments in methanol-water mixtures which indicate that the model is capable of predicting electrokinetic effects in nonaqueous solutions of LiCl. Mixtures of methanol and water were chosen as the nonaqueous solvents because these mixtures attain a wide range of dielectric constant and viscosity values, the only solvent parameters that enter the model.

The major obstacle in comparing the experimental results in methanol-water mixtures to the model is the scarcity of information in the literature on the diffusivities of Li^+ and Cl^- ions in the methanol-water mixtures. In addition, at this time no theory adequately predicts ionic conductivities and dissociation constants in solutions with concentrations above 10^{-2} M for solvents with dielectric constants in the range we are interested in. This is less of a problem in aqueous experiments, but it becomes much more serious for solvents with low dielectric constants where ions have a greater tendency to associate into nonconducting species.

Chapter 7 presents further experimental examination of the ability of the space-charge model to describe electrokinetic transport in nonaqueous solvents. The first part of Chapter 7 is devoted to the experimental examination of the surface characteristics of the mica wall when exposed to nonaqueous electrolyte solutions. The second part presents experimental tests of the validity of the model in nonaqueous solvents. These tests of the model were performed in methanol solutions of LiCl. The agreement between model predictions and experiments is viewed as good. The membrane wall surface charge density, the only unknown parameter in the model, was obtained by fitting the pore fluid conductivity experiments to the model predictions, and was then used to predict the results of the other experiments.

The significance of the work presented rests in its examination, both experimentally and theoretically, of the space-charge model for electrokinetic transport through charged porous media. The model is compared to other models in the literature and is shown to be superior in describing electrokinetic effects. For the first time, the model is also compared to experimental data in nonaqueous solvents and is shown to be capable of describing electrokinetic experiments. Further work that needs to done in testing the model is offered in Chapter 8.

Briefly, the model needs to be tested further in other nonaqueous solvents, and the model has been tested only with 1:1 electrolytes with the same anion, Cl^- (2,3). The model needs to be tested in solutions with electrolytes having different anions, like KBr, and different ionic valencies, such as $MgCl_2$. Finally, the model should be extended to cover porous media with nonidentical pore sizes, but known pore size distributions. This situation is not difficult to model mathematically, and can be easily attained experimentally with track-etched mica membranes.

CHAPTER 2
MATHEMATICAL MODEL

2.1 Previous Work

The earliest theoretical treatments of the effects of double layers on transport through long, charged, circular capillaries were by Dresner (1) and Osterle and coworkers (4,5,6). They predicted the rates of transport of electrolyte, solution, and charge using the Poisson-Boltzmann equation for the double layer potential in pores, the Nernst-Planck equation for the ionic fluxes, and the Navier-Stokes equation for the fluid velocity. Kobatake and coworkers used irreversible thermodynamics to derive equations for the ionic fluxes that were then applied to infinite slit pores (7). They used the Debye-Huckel approximation to the Poisson-Boltzmann equation, and set the fluid velocity to zero. If these approximations are not used, it can be shown that the approach used by Kobatake gives the same theoretical results as the approach used by Dresner and Osterle. This latter approach, called the space-charge model here, allows the transport coefficients for various driving forces to be computed for specific values of the pore wall charge, pore size, and electrolyte concentration.

One of the main differences between the space-charge model and other electrokinetic models is the use of the Poisson-Boltzmann equation to compute the space-charge density in the pore fluid.

Computations using the Poisson-Boltzmann equation, discussed below, give the variation of the space-charge radially in the pore fluid within a cylindrical pore. This differs from the Meyer-Sievers approach (8,9,10,11), for example, for which the radial variation of the charge in the pore fluid, arising from the charge on the pore walls, is not accounted for. Hence, the term space-charge model is used to distinguish this model from others that are available.

The space-charge model for electrokinetic effects in well-characterized, charged microcapillaries was first tested quantitatively by Westermann-Clark and Anderson (2), who examined aqueous solutions of an electrolyte (KCl) having nearly equal ionic mobilities. They used track-etched mica membranes whose pores in a given membrane are uniform, identical capillaries with predetermined size. By applying three different driving forces across each membrane, namely, electric potential, pressure, and concentration differences, three independent electrokinetic experiments (the pore fluid conductivity, the streaming potential, and the exclusion-diffusion potential) were performed on each membrane. They then fitted the measurements from one experiment (pore conductivity) to the space-charge model, and the value of the pore wall charge so obtained was used to test the model as applied to the other experiments. Good agreement was obtained between the theory and experiments for membranes having pore radii in the range $a = 3.5 - 26.5$ nm exposed to aqueous KCl solutions with concentrations up to 0.1 M. Westermann-Clark and Christoforou (3) performed the same test on solutions of aqueous NaCl, for which the ionic mobilities differ, and reached essentially the same conclusions.

2.2 Model Assumptions and Equations

The charged porous membrane is viewed as consisting of fine, straight, identical capillaries filled with an incompressible Newtonian fluid having a uniform dielectric constant and viscosity and containing a single completely dissociated electrolyte. Since the pores of the membrane are identical, the steady-state electrokinetic transport through the membrane can be described by the behavior of a single pore having a length (ℓ) much greater than its characteristic cross sectional dimension (L). The characteristic cross sectional dimension L is the pore radius (a) for a circular pore, and the half slit width (d) for an infinite slit pore (see Figure 2-1). The immobile charge on the pore wall is assumed to be uniformly distributed. The model pore is in contact with electrolyte solutions whose concentrations, pressures, and electrical potential can differ. The charge numbers of the ions of the electrolyte are z_+ and z_-. Ions resulting from solvent dissociation (e.g., H^+, OH^-) are ignored since it is assumed that their concentrations are negligible compared to the concentration of the electrolyte. The individual ionic mobilities (U_i) and diffusivities (D_i) are taken to be independent of electrolyte concentration and are assigned their values at infinite dilution. At the ends of the pores, at $x = 0$ and $x = \ell$, equilibrium is assumed between the bulk solution just outside the pore and the solution just inside the pore. Although boundary layer polarization effects are not considered here, if they exist at the ends of the pore, the term bulk solution refers to the solution at the membrane-bulk solution interface. Another important assumption is that the transport rates of ions do not prevent the establishment of

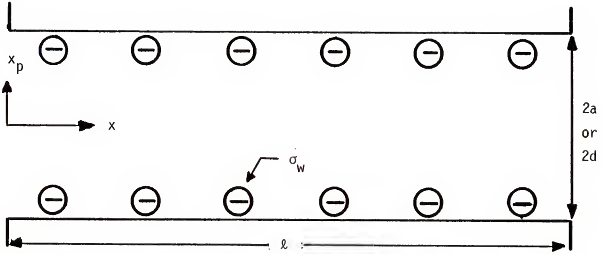

Figure 2-1 Model pore. The cylindrical pore radius is a, and the infinite slit half width is d. The length of the pore is ℓ; x denotes the axial direction in the pore, and x_p is the dimensionless radial direction. The immobile wall charge (negative here) is σ_w.

equilibrium concentration profiles within distances of order L of the pore entrance and exit. The latter assumption implies that $\langle v_x \rangle L/D_i \ll 1$, where $\langle v_x \rangle$ is the average fluid velocity through the pore.

The basic equations of the model (in SI units) are the Poisson-Boltzmann, Nernst-Planck, and Navier-Stokes (low Reynolds number form) equations, along with equations for the conservation of mass and charge

$$\nabla^2 \Psi = (L/D)^2 \left[\frac{\exp(-z_- \Psi) - \exp(-z_+ \Psi)}{z_+ - z_-} \right] \tag{2-1a}$$

$$\Psi = e\psi/kT \tag{2-1b}$$

$$D = \left[\frac{\varepsilon kT}{(z_+ - z_-) e^2 C_b} \right]^{1/2} \tag{2-1c}$$

$$\underline{N}_i = -D_i \nabla C_i - \frac{z_i e}{kT} D_i C_i \nabla\phi + C_i \underline{v} \tag{2-2}$$

$$\underline{0} = -\nabla P_o - e(z_+ C_+ + z_- C_-)\nabla\phi + \eta \nabla^2 \underline{v} \tag{2-3}$$

$$\nabla \cdot \underline{N}_i = 0 \tag{2-4}$$

$$\nabla \cdot \underline{v} = 0 \tag{2-5}$$

The Laplacian operator was made dimensionless by substituting $r = ax_p$ for the circular pore and $y = dx_p$ for a slit. L is the appropriate length scale in the pore cross section, i. e., the pore radius a in a circular pore, and the half slit width d in the slit pore. It should be mentioned that C_b is an apparent bulk concentration, that is, the bulk phase electrolyte concentration that would be in equilibrium with the fluid in the cross section x = constant inside the pore. The concentrations $C_b(0)$ and $C_b(\ell)$ are the bulk phase electrolyte concentrations on either side of the membrane. Manipulation of these equations is described elsewhere (2,4,5). The electrical potential inside the pore can be split into two parts, that is, the electrostatic potential of the double layer in the pore cross section, and the electromotive potential whose gradient drives ionic fluxes axially through the pore

$$\phi(x_p,x) = \psi(x_p,x) + V(x) \tag{2-6}$$

The boundary condition for the electrostatic potential at the pore wall can take either of two forms

$$x_p = 1: \quad \Psi = e\psi(1)/kT \equiv \Psi(1) \tag{2-7a}$$

$$\text{or} \quad \frac{\partial \Psi}{\partial x_p} = \frac{e}{\varepsilon kT} L\sigma_w \equiv S_w \tag{2-7b}$$

For both the slit and the cylinder, the boundary condition at the centerline ($x_p = 0$) is

$$\frac{\partial \Psi}{\partial x_p} = 0 \tag{2-8}$$

If the pore wall charge is constant, then the wall potential will be a strong function of the bulk electrolyte concentration, and vice versa. Since there is no general analytical solution for the Poisson-Boltzmann equation, we used a fourth order Runge-Kutta technique to obtain the electrostatic potential profile from the equation (2-1a) subject to either (2-7a) or (2-7b). Appendix A contains the numerical algorithm for the solution of the Poisson-Boltzmann equation and the calculation of the electrokinetic fluxes through the pore. In addition, we present below some useful approximate solutions to the Poisson-Boltzmann equation. It should be kept in mind that the ratio of L to the Debye length (L/D) in equation (2-1a), plays an important role in the electrokinetic calculations, and, as can be seen in equation (2-1c), it is proportional to the square root of the bulk electrolyte concentration $C_b^{1/2}$.

2.3 Approximate Solutions to the Model Equations

There is no generally applicable analytical solution of the Poisson-Boltzmann equation (equation (2-1a)) for circular cylindrical pores. However, approximate analytical solutions can be obtained when (i) the absolute value of the dimensionless potential inside pores is smaller than unity (low potential or Debye-Hückel approximation), or

(ii) when this potential is much larger than unity (high potential approximation) (12,13). For a negatively charged pore wall and an 1:1 electrolyte these approximations take the form

$$|\Psi_L| < 1: \qquad \frac{\exp(\Psi_L) - \exp(-\Psi_L)}{2} \approx \Psi_L \qquad (2\text{-}9a)$$

$$|\Psi_H| > 1: \qquad \frac{\exp(\Psi_H) - \exp(-\Psi_H)}{2} \approx - \frac{\exp(-\Psi_H)}{2} \qquad (2\text{-}9b)$$

We use negative potentials, but positive potentials are treated in the same way with an obvious sign change. Equation (2-1a) can be approximated by

$$|\Psi| = |\Psi_L| < 1: \quad \nabla^2\Psi_L = \left(\frac{L}{D}\right)^2 \Psi_L \qquad (2\text{-}10a)$$

$$|\Psi| = |\Psi_H| > 1: \quad \nabla^2\Psi_H = - \left(\frac{L}{D}\right)^2 \frac{\exp(-\Psi_H)}{2} \qquad (2\text{-}10b)$$

subject to the boundary conditions in equations (2-7a) and (2-7b). Depending on the value of the potential at the center line and at the wall, different solutions for potential profile can be derived. Levine and coworkers (12) solved both the high and low potential approximations for the potential profile when the potential at the pore wall is specified (equation (2-7a)), and we have solved for the potential profile when the wall charge density is specified (equation (2-7b)). The electrostatic condition at pore walls is usually determined by the chemical equilibrium between the pore wall charge and the surrounding solution, rather than by an externally controlled, applied electrical potential. Hence, our approximate solutions using the pore wall charge condition, rather than the pore wall potential, are generally more useful for charged membranes. Solutions to the Poisson-Boltzmann equation subject to different boundary conditions in various subdomains are presented elsewhere (12,14), and are shown in Appendix C.

2.4 Calculation of Fluxes through the Pore

The fluxes calculated for the electrokinetic transport through fine capillaries are the solvent flow (q), the solute flow (J_s), and the electrical current (I_x), averaged over the pore cross section

$$q = < v_x > \tag{2-11a}$$

$$J_s = < N_{+x} + N_{-x} > \tag{2-11b}$$

$$I_x = e< z_+N_{+x} + z_-N_{-x} > \tag{2-11c}$$

where the brackets < > indicate appropriate integration to obtain an area average (see Appendix B). At steady state, the fluxes in equations (2-11a) to (2-11c) are independent of axial position in the pore since the pore walls are impenetrable. Equations (2-3) and (2-5) can be solved for the axial velocity v_x and the pressure $P_o(x_p,x)$ inside the pore by using the equilibrium condition at each end of the pore to relate intrapore variables to bulk variables. Substituting the results into the x-component of the Nernst-Planck equation, and then averaging over the pore cross section, the following system of equations is obtained

$$q = L_{11}\frac{dP}{dx} + L_{12}kT\frac{d\ln C_b}{dx} + L_{13}\frac{dV}{dx} \tag{2-12a}$$

$$J_s = L_{21}\frac{dP}{dx} + L_{22}kT\frac{d\ln C_b}{dx} + L_{23}\frac{dV}{dx} \tag{2-12b}$$

$$I_x = L_{31}\frac{dP}{dx} + L_{32}kT\frac{d\ln C_b}{dx} + L_{33}\frac{dV}{dx} \tag{2-12c}$$

P is the bulk equivalent pressure which would be in mechanical equilibrium with the solution in the pore cross section at x. The coefficients L_{ij} are functions of (i) the mobilities (or diffusivities) of the individual ions, and (ii) the potential distribution in the pore, which is in turn a function of the dimensionless pore wall charge (S_w) and the ratio L/D. Formulas for the coefficients of interest in our experiments are in Appendix B. It should be noted that, under the assumptions of the space-charge model, it has been shown that the model is capable of describing transport in charged pores in contact with aqueous alkali chloride solutions, at least when the pores are 3.5 nm in radius or larger, and when ionic strength is 0.1 M or less (2).

2.5 Calculation of Electrokinetic Parameters

Four electrokinetic parameters are calculated theoretically and measured experimentally in later Chapters. For a membrane placed between two bulk reservoirs of electrolyte (see Figure 2-2), which in general could have different concentrations ($C_I \neq C_{II}$), electrical potentials ($V_I \neq V_{II}$), and/or hydrostatic pressures ($P_I \neq P_{II}$), the four electrokinetic quantities discussed in later Chapters are related to the flux equations (2-12a) to (2-12c) as follows.

Exclusion-Diffusion Potential

In an exclusion-diffusion potential (or concentration potential) experiment, the membrane is in contact with two reservoirs having different electrolyte concentrations C_I and C_{II}, with no pressure difference or current through the membrane. This concentration difference gives rise to an electrical potential (see equation (2-12c)) that can be measured in the bulk solutions outside the membrane. The predicted electrical potential (ΔV_{ed}) across the membrane, normalized with the Nernstian potential, can be evaluated from the space-charge model

$$\omega_{ed} = \left\{ \frac{V_{ed}/(kT/e)}{\Delta \ln C_b} \right\}_{\substack{\Delta P = 0 \\ I_x = 0}} = \frac{e}{\Delta \ln C_b} \int_{C_{II}}^{C_I} \frac{L_{32}}{L_{33}} \, d\ln C \qquad (2\text{-}13)$$

The differences denoted by Δ are taken as side II ($x = \ell$) minus side I ($x = 0$). Details of the calculations required to evaluate L_{32} and L_{33}, as well as space-charge model predictions for the exclusion-diffusion potential, are presented in the next Chapter.

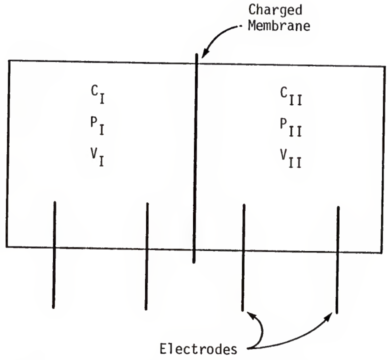

Figure 2-2 Charged porous membrane held between electrolyte solutions I and II which can be at different hydrostatic pressures, electrical potentials, and electrolyte concentrations. The electrical potential can be applied or measured with the double pair of electrodes placed in the bulk solutions.

Pore Fluid Conductivity

In an experiment to find the pore fluid conductivity, concentration and pressure differences across the membrane are zero. A current I_x is applied through the membrane, and an electrical potential (ΔV) is measured across the membrane. Using the space-charge model, the pore fluid conductivity can be calculated from equation (2-12c)

$$\kappa = \ell \left[\frac{I_x}{\Delta V}\right]_{\substack{\Delta C_b = 0 \\ \Delta P = 0}} = - L_{33} \tag{2-14}$$

In Chapter 4, the pore fluid conductivity is examined in more detail, and comparisons of the space-charge model predictions to other models in the literature are also presented.

Streaming Potential

In a streaming potential experiment, an applied pressure produces an electrical potential across the membrane where the current and the concentration difference across the membrane are zero. Using the space-charge model (see equation (2-12c)) the streaming potential can be calculated from

$$\nu = \frac{\Delta V_s}{\Delta P} = - \frac{L_{31}}{L_{33}} \tag{2-15}$$

In Chapter 5, the space-charge model predictions for the streaming potential are examined and compared to other models in the literature.

Streaming Current

In a streaming current experiment the electrodes in the two identical solutions in contact with the membrane are close-circuited. A pressure difference across the membrane produces a electrical current through the membrane. If A_p is the total pore cross section area, the streaming current, calculated from the space-charge model, is

$$I_s = \frac{A_p I_x}{\Delta P} = \frac{A_p L_{31}}{\ell} \qquad (2\text{-}16)$$

The streaming current I_s is the only electrokinetic parameter of the four shown above which we have not investigated in detail from a theoretical perspective. Space-charge model predictions for the other three electrokinetic quantities, the exclusion-diffusion potential, pore fluid conductivity, and streaming potential, are discussed in Chapters 3 to 5. Nonaqueous experiments using these electrokinetic predictions are then presented in Chapters 6 to 7.

CHAPTER 3
THE EXCLUSION-DIFFUSION POTENTIAL IN CHARGED MICROPOROUS MEMBRANES

3.1 Introduction

When two different solutions of an electrolyte are brought into contact, a region forms in which the composition varies from that of one solution to that of the other. We discuss situations in which this contact region is formed across a charged porous membrane. The junctions considered are junctions of the same 1:1 electrolyte, e.g., $NaCl(C_I)//NaCl(C_{II})$, but not junctions of different electrolytes, $LiCl(C_I)//NaCl(C_{II})$, or junctions that do not involve 1:1 electrolytes, $CuCl_2(C_I)//CuCl_2(C_{II})$. Because of the electrolyte concentration difference across the membrane, an electrical potential develops. This potential arises from two contributions that are called the exclusion and diffusion potentials here, and the combination of these potentials is called the exclusion-diffusion potential. This terminology is chosen to denote explicitly the origins of the exclusion-diffusion potential and to avoid confusion with other terms often used for this potential.

From work with charged porous membranes (2,15), we found that the Meyer-Sievers model for exclusion-diffusion potential sometimes compares favorably with theoretical predictions from the more detailed space-charge model, but in other situations the models disagree. To elucidate the behavior of the two models, and to ascertain those situations in which the much simpler and frequently used Meyer-Sievers model is adequate or inadequate, we undertook the investigations reported below. However, before the two models are compared, we describe the physical transport mechanisms that give rise to the exclusion-diffusion potential across charged porous membranes.

The diffusion portion of the exclusion-diffusion potential arises because the ions of a dissolved electrolyte have different mobilities. The mobility of the aqueous chloride ion, for example, is higher than that of the aqueous sodium ion. When a junction is formed between electrolyte solutions with different concentrations, electrolyte diffuses from the solution with the higher concentration to that with the lower concentration. Since the mobilities of the ions of an electrolyte differ in general, one type of ion diffuses more rapidly from the high concentration side of the contact zone, through the junction, to the low concentration side. Meanwhile, the less mobile ions are left behind on the high concentration side of the contact zone. Hence, a separation of charge across the contact zone would occur because of the difference in ionic mobilities. This type of separation of charge would cause an electrical potential. However, the solutions on each side of the contact zone are not connected except through this zone, so this potential develops in the absence of a current in order to help the less mobile ions across the contact zone and to retard the more mobile ions. This diffusion potential would arise across the contact zone even if a charged membrane were not in place.

The exclusion portion of exclusion-diffusion potential arises because of the charge on the pore walls of the membrane. This charge repels ions whose charge has the same sign as that of the pore wall (coions) and attracts ions whose charge has the opposite sign (counterions). There is therefore an excess of counterions in the pore and an exclusion (depletion or negative excess) of coions. In the presence of an electrolyte concentration difference across the membrane, the counterions would diffuse through the pores to the low concentration side of the membrane, but since they are excluded from pores, the coions would build up at the high concentration entrance to the pores. This separation of charge would result in an electrical potential that would retard counterions and help coions through the pores. In fact, this potential prevents the actual buildup of ions that would occur at the ends of the pores.

The exclusion potential often is called the "Donnan potential." However, Donnan exclusion can occur because of (i) steric exclusion, as with polymer molecules too large to enter pores, (ii) electrostatic repulsion, or (iii) a combination of steric and electrostatic effects. Our concern is with purely electrostatic exclusion, so to prevent confusion with steric effects we use the term "exclusion potential" instead of "Donnan potential." The diffusion potential also is known by various other names, including the "liquid-junction potential" and the "Henderson potential." We use the term "diffusion potential" because of the mechanism that produces this potential and because it is only one limiting case of the observable potentials across a junction formed with a charged porous membrane. When both the exclusion and diffusion effects are taken into account, the exclusion-diffusion potential results.

3.2 Models for the Exclusion-Diffusion Potential

Two 1:1 electrolytes are compared for each model: one with equal ionic diffusivities, $D_+ = D_- = 2\mathrm{x}10^{-9}$ m^2/s (aqueous KCl, for example), and another with unequal diffusivities, $D_+ = 1\mathrm{x}10^{-9}$ m^2/s and $D_- = 2\mathrm{x}10^{-9}$ m^2/s (aqueous LiCl, for example). It is assumed that these diffusivities apply at any electrolyte concentration. The models compared are called here (i) the Meyer-Sievers model, and (ii) the space-charge model, which uses the Poisson-Boltzmann equation to calculate the space-charge density in the pore fluid.

Meyer-Sievers Model

Since the Meyer-Sievers model is widely available in the literature (8,9,10,11,16,17), we merely outline its derivation in order to contrast some of its features with the space-charge model. The Meyer-Sievers model assumes that the ionic concentrations C_i in a charged pore are related to the bulk concentration C_b by

$$\text{coions:} \quad C_- = y \tag{3-1a}$$

$$\text{counterions:} \quad C_+ = y - A \tag{3-1b}$$

$$y(y - A) = C_b^2 \tag{3-1c}$$

$$A = 2\sigma_w/ae \tag{3-2}$$

where A is the charge per unit volume in a cylindrical pore. Although a negatively charged pore wall is assumed, a positively charged pore would require obvious changes. If a current were passed through the pore, the fraction of the current carried by ions of type i (= + or -) would be given by the transport number

$$t_i = \frac{U_i C_i}{\sum_i U_i C_i} \tag{3-3}$$

where C_i is a function of axial position x in the pore, and U_i is the mobility of "i." The Nernst-Einstein equation, $U_i = D_i/kT$, can be used to relate the ionic mobilities U_i to the ionic diffusivities D_i.

Two bulk electrolyte solutions with concentrations C_I and C_{II} are brought into contact across the charged pore whose length is ℓ. For any part of the contact zone with a thickness dx, the transfer of a faraday would require the migration of t_i/z_i moles of ions of type "i" in the direction of the sign of z_i, where z_i is the charge number of "i." This hypothetical current would result in a free energy change for each type of ion "i," with a net free energy change of

$$dG = -\,e\,dV = \sum_i \frac{t_i}{z_i}\,d\mu_i \tag{3-4}$$

If a_i is the activity of "i," then

$$dV = -\frac{kT}{e}\sum_i \frac{t_i}{z_i} d\ln a_i \tag{3-5}$$

where k is Boltzmann's constant and T is temperature.

Substituting equations (3-1a) to (3-1b) for the intramembrane ionic concentrations C_i into equation (3-3) for the transport numbers t_i, and substituting the t_i into equation (3-5), one obtains

$$\Delta V_{ed} = V_{II} - V_{I} = -\frac{kT}{e}\int_{y_I}^{y_{II}} \left[\frac{U_+(y - A) - U_-y}{U_+(y - A) + U_-y}\right] d\ln[y(y - A)] \tag{3-6a}$$

Since the individual ionic activities cannot be determined, Meyer and Sievers implicitly use

$$d\ln a_{\pm} = d\ln(C_+C_-)^{1/2} \tag{3-6b}$$

with unit activity coefficients assumed. After substituting,

$$X \equiv \frac{2y}{A} - 1 \tag{3-7}$$

which can be related to C_b by equations (3-1a) and (3-1b), equation (3-6a) gives

$$-\frac{\Delta V_{ed}}{kT/e} = U\ln\left(\frac{X_{II} - U}{X_I - U}\right) \qquad (3\text{-}8a)$$

DIFFUSION

$$+\frac{1}{2}\ln\left[\frac{(X_{II} + 1)(X_I - 1)}{(X_{II} - 1)(X_I + 1)}\right]$$

EXCLUSION

where

$$U \equiv \frac{U_+ - U_-}{U_+ + U_-} \qquad (3\text{-}8b)$$

The two terms in equation (3-8a), which is the final result of the derivation by Meyer and Sievers, are labeled with the limiting cases that they represent. The first term is Henderson's equation for the diffusion potential, and the second term is the Donnan electrostatic exclusion potential. When the electrolyte concentration (C_b or y) is much larger than the charge per unit pore volume, $C_b >> |A|$ only the diffusion term is important, and when $C_b << |A|$ only the exclusion term is important. These limits are shown in Figure 3-1 for $C_I = 2C_{II}$ and for a negative pore surface charge per pore volume of $A = -0.1$ mol/dm^3. At high electrolyte concentrations in Figure 3-1, the unequal ionic mobility electrolyte creates a nonzero diffusion potential across the membrane while the equal mobility electrolyte does not. At low concentrations, the potential goes to the Nernstian limit in both cases

$$\lim_{C_b \to 0} \Delta V_{ed} = \frac{kT}{e} \ln \frac{C_I}{C_{II}} \tag{3-9}$$

Since the exclusion-diffusion potential always goes to this limit, we define a dimensionless (normalized) exclusion-diffusion potential

$$\omega_{ed} = \frac{\Delta V_{ed}}{(kT/e)\ln(C_I/C_{II})} \tag{3-10a}$$

$$\lim_{C_b \to 0} \omega_{ed} = 1 \tag{3-10b}$$

$$\lim_{C_b \to \infty} \omega_{ed} = U \tag{3-10c}$$

where the limits of the exclusion-diffusion potential at high and low bulk electrolyte concentrations are noted in equations (3-10b) and (3-10c).

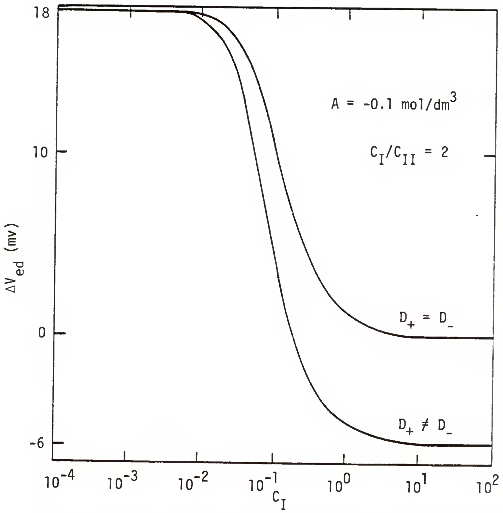

Figure 3-1 ΔV_{ed} versus C_I from the Meyer-Sievers model for $A = -0.1$ mol/dm^3. The exclusion-diffusion potential approaches the same limit at low concentrations regardless of ionic mobilities, but at high concentrations the limit of ΔV_{ed} depends on ionic mobilities.

Space-Charge Model

The space-charge model is presented in Chapter 2. This model can treat simultaneous driving forces for transport, including not only a concentration difference across a membrane, but also pressure and electrical potential differences. For all three of these driving forces, it has been shown that the space-charge model gives good predictions of experimental electrokinetic transport data for charged porous membranes in contact with aqueous 1:1 electrolyte solutions (2). However, the present discussion is confined to the exclusion-diffusion potential, for which a concentration difference is the only driving force. The normalized form of the exclusion-diffusion potential is given by the space-charge model (Chapter 2) as

$$\omega_{ed} = \left\{ \frac{-\Delta V_{ed}}{(kT/e)\Delta \ln C_b} \right\}_{\substack{\Delta P = 0 \\ I_x = 0}} = \frac{e}{\Delta \ln C_b} \int_{C_{II}}^{C_I} \frac{L_{32}}{L_{33}} \, d\ln C \qquad (2\text{-}13)$$

Equation (2-13) is the final result for exclusion-diffusion potential in the space-charge model, just as equation (3-8a) is the final result for the Meyer-Sievers model.

Both models assume uniform, immobile pore wall charge, complete dissociation of the electrolyte, and ionic mobilities that are independent of the electrolyte concentration. The pore geometry is specified in more detail for the space-charge model than for the Meyer-Sievers model, where no mention of the pore geometry is made. However, to relate the charge on the pore walls to the charge per unit pore volume A in the Meyer-Sievers model, a pore surface area per unit volume of the pore fluid must be known. The comparisons carried out below use the same pore surface area to pore volume ratio (2/a) for both the space-charge and Meyer-Sievers models. The variables A and X in the Meyer-Sievers model are therefore related to S_w and a/D in the space-charge model by

$$A = \frac{2\varepsilon kT}{e^2 a^2} S_w \qquad \text{(3-11a)}$$

$$X = \frac{S_w}{|S_w|}\left(1 + \frac{(a/D)^4}{4S_w^2}\right)^{\frac{1}{2}} \qquad \text{(3-11b)}$$

3.3 Comparison of the Meyer-Sievers and the Space-Charge Models

We compare predictions of the dimensionless exclusion-diffusion potential from the Meyer-Sievers and the space-charge models for dimensionless pore wall charge densities in the range $0.1 \leq |S_w| \leq 100$, and for pore radius to Debye length ratios in the range $0.4 \leq a/D \leq 25.0$. These ranges of the wall charge and the electrolyte concentration span the ranges of these variables that we have encountered in our experimental work with porous membranes (2,15), as well as the ranges of these variables for which the effects discussed are significant in studies that we have encountered in the literature. Figure 3-2a shows the dimensionless exclusion-diffusion potential for both models when the ionic mobilities of the electrolyte are equal ($U_+ = U_-$), while Figure 3-2b shows the unequal mobility case ($U_-/U_+ = 2$). Although the ratio of electrolyte concentrations outside the membrane was kept at

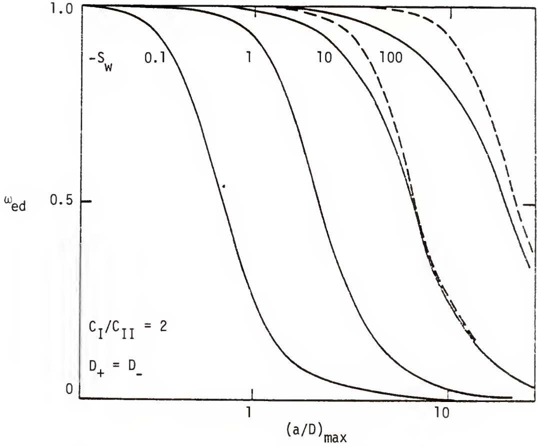

Figure 3-2 ω_{ed} versus a/D. S_w is the dimensionless pore wall charge. ———— Space-charge model predictions.------Meyer-Sievers model: (a) Equal ionic mobilities ($D_+ = D_- = 2x10^9\ m^2/S$)

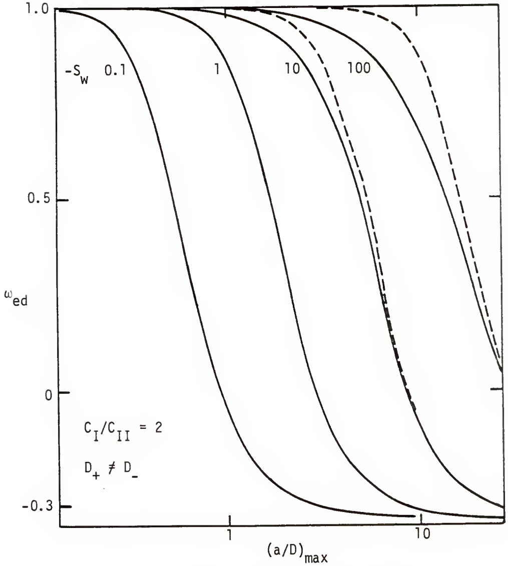

Figure 3-2 Continued: (b) Unequal ionic mobilities ($D_+ = 10^{-9}$, $D_- = 2 \times 10^{-9}$ m^2/S).

$C_I/C_{II} = 2$ in Figures 3-2a and 3-2b, other C_I/C_{II} ratios yield similar conclusions.

The Meyer-Sievers model calculations are the broken curves in Figures 3-2a and 3-2b, while the solid curves are the space-charge model results. As expected, both models go to the high and low concentration limits in equations (3-10b) and (3-10c). Furthermore, for low values of the pore wall charge ($|S_w| < 1$), where the excess of counterions in the pore caused by the charge on the pore wall is small, nearly identical results are also obtained, as expected, from the two models for both the equal and unequal ionic mobility cases and for any electrolyte concentration. However, as $|S_w|$ increases, discrepancies between the two models are observed, and to explain these discrepancies, we discuss below the effects of pore geometry, convective flow, and ionic distributions inside pores. To examine whether pore geometry has a significant effect on in the space-charge model results for the exclusion-diffusion potential, calculations of the dimensionless exclusion-diffusion potential were done for a cylindrical pore and for an infinite slit pore. For the two pore geometries the fixed charge per unit area on the pore wall, the fixed charge per unit pore volume, and the bulk electrolyte concentrations (or Debye lengths) outside the membrane were identical.[1] With the controlling variables for the two geometries so defined, the exclusion-diffusion potential calculated for either the slit or the cylinder is practically independent of pore geometry.

In Figure 3-3, the curves are the space-charge model calculations

---

[1] Although the actual pore wall charge (C/m^2) is the same for both the slit and the circular pore, the dimensionless wall charge $S_{w,slit}$ used in calculations was $S_{w,slit} = S_w/2$ as a result of the parameterizations used.

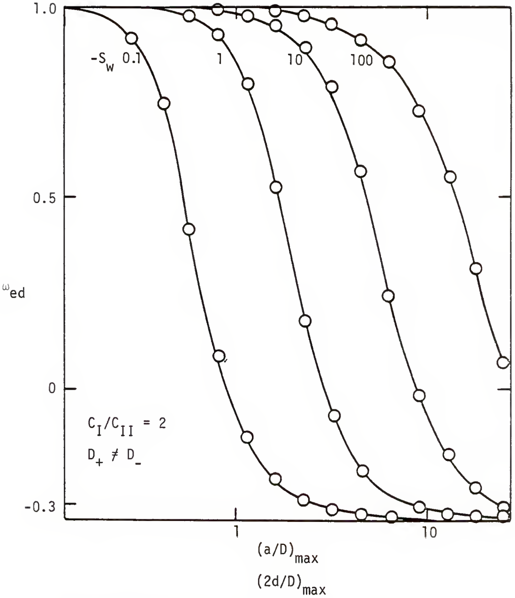

Figure 3-3 Comparison of the theoretical predictions ω_{ed} from the space-charge model for a cylindrical pore (curves) and an infinite slit pore (points). a is the cylindrical pore radius, and 2d is the infinite slit separation. The charge per unit pore area and per unit pore volume, as well as the bulk concentrations C_I and C_{II}, are the same for the slit and the cylinder.

for a cylindrical pore, and the points are the infinite slit calculations. The differences between infinite slit (points) and circular pore (curves) results for the dimensionless exclusion-diffusion potential from the space-charge model are small (3% at most) for the entire range of wall charges and concentrations examined in Figure 3-3. Although Figure 3-3 is for ions with unequal mobilities, similar results are obtained for an electrolyte whose ions have equal mobilities. Hence, while the Meyer-Sievers model does not depend on any particular pore geometry, it disagrees with the space-charge model whether slit pores or circular pores are used.

The Meyer-Sievers model ignores convection inside pores, while the space-charge model uses the Navier-Stokes equation for the fluid velocity inside a pore. Because of the convective term in the Nernst-Planck equation (equation (2-2)), the coefficients L_{32} and L_{33} include osmotic contributions. To evaluate the effects of convection on the exclusion-diffusion potential, we eliminated the convective terms in the space-charge model and recalculated the dimensionless exclusion-diffusion potential. This was done by setting v_x to zero in the Nernst-Plank equation, and carrying this approximation through the derivation of the coefficients L_{32} and L_{33}

$$L_{32} \doteq \frac{2eC_b}{kT} \int_0^1 x_p \left[D_- \exp(+\Psi) - D_+ \exp(-\Psi) \right] dx_p \qquad (3\text{-}12a)$$

$$L_{33} \doteq \frac{2e^2C_b}{kT} \int_0^1 x_p \left[D_- \exp(+\Psi) + D_+ \exp(-\Psi) \right] dx_p \qquad (3\text{-}12b)$$

Using equations (3-12a) and (3-12b) it can easily be shown that

$$\omega_{ed} \doteq \frac{1}{\Delta \ln C_b} \int_{C_{II}}^{C_I} \left[\frac{\langle t_+ \rangle}{z_+} - \frac{\langle t_- \rangle}{z_-} \right] d\ln C \tag{3-13}$$

For both the equal and the unequal ionic mobility cases, the use of equations (3-12a) and (3-12b) to approximate the exclusion-diffusion potential instead of the more accurate equations for L_{ij} in Appendix B leads to only small errors (less than 5% in the worst cases at high $|S_w|$ values). Hence, to a good approximation, the osmotic contribution to the calculated value of the exclusion-diffusion potential can be neglected. Consequently, the fact that the Meyer-Sievers model ignores convection inside pores, while the space-charge model does not, cannot explain the discrepancies between the two models in Figures 3-2a and 3-2b.

Kobatake and coworkers (7), who used the Debye-Hückel approximation to the Poisson-Boltzmann equation (equation (2-1)) inside infinite slit pores, also concluded that neglecting convection has only a small effect on calculated exclusion-diffusion potentials. It should be noted that the use of the Debye-Hückel approximation is restricted to low pore wall potentials. This restriction can be a severe limitation. Quantitatively, this restriction can be expressed as

$$S_w < \frac{aI_1(a/D)}{DI_0(a/D)} \tag{3-14}$$

where I_j is the modified Bessel function of the first kind and order j

(14). Hence, to assert that the use of the Debye-Hückel approximation "corresponds to the limiting case in which the charge density fixed on the capillary wall is high" (7) can be very misleading. Moreover, our experimental experience with porous membranes (2,15) shows that the pore wall charge density is often produced by a reaction at the pore wall. For example, the extent to which -OH groups on the pore wall dissociate often can be controlled by the pH. Hence, it is frequently more realistic to specify S_w, as is done here, than to specify the wall potential as Kobatabe et al. did.

With convection eliminated from the exclusion-diffusion potential as in equations (3-12a) and (3-12b), it deserves note that the effects of the dielectric constant and the viscosity, the only fluid properties that enter the model, are somewhat indirect. The dielectric constant affects the ionic distributions $C_i(r,x)$ via the Poisson-Boltzmann equation. The viscosity affects D_i, but this influence is no greater in the space-charge model than in the Meyer-Sievers model.

Also affecting the performance of the two models are the distributions of ions inside pores. But before delineating the differences between the Meyer-Sievers and space-charge models, we note their points of agreement. In both models, ionic concentrations C_i inside the pore differ from the bulk ionic concentrations because of the fixed charge on the pore walls. Therefore, in both models the ionic transport numbers in the pore differ from their bulk values. In addition, for a negatively charged pore wall, as the electrolyte concentration approaches zero, the cationic transport number in the pore approaches its highest value ($t_+ = 1$), and the anionic transport number approaches its lowest value ($t_- = 0$). And in either model, as the electrolyte concentration becomes large, both transport numbers in the pore are unaffected by the charge on the pore wall. It should also be noted that the space-charge model satisfies the electroneutrality condition

$$-\sigma_w = \frac{1}{a}\int_0^a \rho_e r dr = \frac{ae}{2}(\langle C_+\rangle - \langle C_-\rangle) \tag{3-15}$$

where the result on the right is found from the solution of the space-charge model equations, and where the $\langle C_i \rangle$ are the area averages of the ionic concentrations in the pore. Equation (3-15) shows that $\langle C_+\rangle - \langle C_-\rangle = -A$, and equations (3-1a) and (3-1b) show that the Meyer-Sievers model also satisfies the condition that the charge in the pore fluid ($C_+ - C_-$) balances the pore wall charge (A). Hence, the Meyer-Sievers and the space-charge models both agree that (i) the coion and counterion concentrations and transport numbers inside the pore are affected by the charge on the pore walls, that (ii) the charge on the pore wall is balanced by the charge in the pore fluid, and that (iii) the limits of the normalized form of the exclusion-diffusion potential are given by equations (3-10b) and (3-10c).

Nonetheless, this does not imply that the C_i values calculated with the Meyer-Sievers model are correct. As discussed below, the space-charge model explicitly calculates the radial variation of the ionic concentrations $C_i(r,x)$ inside the pore, from which average transport numbers at any cross section (x = constant) inside the pore can be deduced. On the other hand, the Meyer-Sievers model ignores the radial variation of C_i inside pores (see equations (3-1a) and (3-1b)) and assumes the transport numbers to be constant at any particular cross section inside the pore.

To simplify comparisons between the two models, we can omit convective flow from the space-charge model as in equations (3-12a) and (3-12b). As noted above, the effects of convection on the exclusion-diffusion potential in the space-charge model are negligible, and using equations (3-12a) and (3-12b) does not affect comparisons between the two models significantly. At first glance, equation (3-13) strongly resembles the exclusion-diffusion potential in the Meyer-Sievers model (see equation (3-5)). The primary difference between equations (3-5) and (3-13) is that the $\langle t_i \rangle$ in equation (3-13) are based on the area-average values of the concentrations $\langle C_i \rangle$ in a cross section of a cylindrical pore (see equation (3-12b)) while the transport numbers t_i in equation (3-5) do not account for the radial variation of C_i.

For the space-charge model, there is a particular bulk-equivalent concentration $C_b(x)$ at any axial position x in the pore, and given S_w, the potential profile at x can be calculated. With the potential profile known, the $C_i(r,x)$ can be found from the Poisson-Boltzmann equation (equation (2-1)) and area-averaged to obtain $\langle C_i(x) \rangle$. Finally, the $\langle C_i \rangle$ can be substituted into equations (3-12) to obtain $\langle t_i \rangle$. In general, these values of $\langle t_i \rangle$ calculated for the space-charge model differ from the values assigned to the transport numbers t_i in the Meyer-Sievers model which uses the C_i from equations (3-1a) and (3-1b). At high electrolyte concentrations the effect of the pore wall charge on the ionic distribution at any cross section inside the pore is small. As a result, $\langle t_i \rangle$ is approximately equal to t_i and the two models should give similar results, a conclusion supported in Figures 3-2a and 3-2b for large values of the ratio of the pore radius to the Debye length. In addition, at low values of the pore wall charge $|S_w|$, the number of excess counterions inside the pore is small, and again the two models behave similarly. For example, if we set $a/D = 10$, at $S_w = -1$ we calculate $\langle t_+ \rangle = t_+ = 0.51$ for the equal mobility case, and the two models give similar results, but at $S_w = -100$ we find $\langle t_+ \rangle = 0.878$, and $t_+ = 0.974$, and the two models give quite different results, as in Figure 3-2a. Thus, the values of the transport numbers inside the pore explain the discrepancies between the two models, discrepancies that originate in the failure of the Meyer-Sievers model to account for the variation of ionic concentrations with radial position inside the pores.

The inadequacies of the Meyer-Sievers model can be attributed to the inappropriateness of the relations used. Equations (3-1a) and (3-1b) show that the Meyer-Sievers model does satisfy the electroneutrality condition, namely, that the charge in the pore fluid balances the pore wall charge. Nonetheless, this does not imply that the C_i values calculated from equations (3-1a) and (3-1b) are correct, or that the intrapore concentrations are constant throughout a cross section of the pore as these equations imply. In the Meyer-Sievers model, the coion concentration y is not equal to $\langle C_- \rangle$ calculated from the space-charge model in those situations in which the models disagree. Equations (3-1a) and (3-1b) oversimplify the ionic distributions inside the pore and lead to the calculation of inaccurate concentrations and transport numbers in the pore.

3.4 Conclusions

For the broad range of dimensionless electrolyte concentrations and pore wall charge densities examined, the exclusion-diffusion potential calculated with the space-charge model does not depend to any significant extent on pore geometry or on convection inside pores. These results imply that the exclusion-diffusion potential is affected less by viscous flow phenomena in pores than by the distributions of ions. The space-charge model attempts to account for the ion-pore wall electrostatic interactions that cause ionic concentrations to vary radially within a pore at any pore cross section. This radial variation of ionic concentrations results in ionic transport numbers that differ from those calculated using equations (3-1a) and (3-1b) in the Meyer-Sievers model. These equations are the major source of error in the Meyer-Sievers model, and because of the inadequacies of equations (3-1a) and (3-1b), any theory for electrokinetic phenomena based on these equations would be expected to fail.

These results can have significant implications for the interpretation of experimental results for liquid junctions formed across charged porous media. Two of the ways that these theoretical results can be used are (i) predicting the exclusion-diffusion potential from pore surface charge densities known from other experiments, and (ii) ascertaining the wall charge densities from experiments by plotting data for the exclusion-diffusion potential as in Figures 3-2a and 3-2b. As Figures 3-2a and 3-2b show, both of these procedures require accurate estimates of the exclusion-diffusion potential at low and high electrolyte concentrations. The former procedure (i) is used in

Chapter 7 in experimental examinations of the space-charge model in track-etched mica membranes. Nonetheless, there is a drawback to using the space-charge model for calculating the exclusion-diffusion potential in that it requires the use of numerical methods. The main drawback to the much simpler Meyer-Sievers model is that, since it ignores the effects of radially nonuniform ionic distributions inside pores, unreliable values can be predicted for the exclusion-diffusion potential. Hence, it is useful to note those situations in which the much simpler calculations with the Meyer-Sievers model apply.

The Meyer-Sievers model is shown here to be a good approximation when (i) the pore wall charge is small, $|S_w| < 1$, and when (ii) the exclusion of coions is total (low electrolyte concentrations) or insignificant (high electrolyte concentrations). It becomes a poor approximation when $|S_w| > 1$. Values of $|S_w| > 1$ are fairly common, since a pore size of a = 100 nm and a pore wall surface charge density of 100 nC/cm^2, for example, would give a value of S_w for an aqueous solution of $|S_w| = 5.6$, which would be a common value for S_w in experiments with microporous media. In view of the theoretical results presented, it seems prudent for many commonly encountered physical situations to calculate the exclusion-diffusion potential using the space-charge model.

CHAPTER 4
THE ENHANCED PORE FLUID CONDUCTIVITY IN CHARGED MICROPOROUS MEMBRANES

4.1 Introduction

When a non-conducting charged solid is brought into contact with an electrolyte solution, the configuration of the solid plays an important role in determining the path of the conducting species. Because the solid is charged, the electrical conductivity of the solution increases, and this increase is most marked with solids that have a high surface area to volume ratio, such as a porous membrane. This phenomenon, often referred to somewhat misleadingly as "surface conductance," results from the increased ionic concentration in the electrical double layer and from the electroosmotic flow near the solid-liquid interface.

One of the earliest attempts to analyze the conductivity enhancement near a solid-electrolyte solution interface was by Bikerman (18,19), who introduced the idea that the electrical conductivity near an electrified solid surface was the result of three contributions: the bulk fluid conductivity, the conductivity arising from the excess of ions in the electrical double layer, and the electroosmotic flow near the solid surface. He studied a slit pore consisting of two noninteracting plates. He neglected end effects and used the Gouy-Chapman view of the electrical double layer, with a constant wall potential assumed, to calculate the space charge density in the double layer. However, Bikerman's work applies only to values of the Debye length which are small compared to the plate separation. Overbeek (19) noted that Bikerman's method usually predicts pore conductivities that are lower than experimentally determined conductivities. Urban and coworkers adapted Bikerman's view of the conductivity near an electrified interface by using Stern's view for the electrical double layer, and by adding another term to Bikerman's results to account for the ionic mobility in the inner Helmholtz region (19,20,21,22). Urban et al. found good agreement between their theory and careful experiments using compacted layers of glass particles, while calculations using Bikerman's model predicted conductivities that were far too low. However, the use of a fitted ionic conductivity inside the Stern layer is ad hoc, and the fair agreement between theory and experiments which Urban et al. obtained does not prove much in view of the wide discrepancies encountered by other experimentalists (19).

Another approach was developed by Schmid (23) who studied porous membranes. In this approach the detailed description of ionic distributions in the electrical double layer is eliminated by use of the argument that the radius of the pores is so small that the charge density can be considered to be uniform in the whole pore (Teorell-Meyer-Sievers, or TMS theory). In addition to the conductivity of the ions in the pore, another term is added to account for the electroosmotic flow of solution inside the pore. Schmid's model was examined by Schlögl (24), and Klump and Woermann (25) used the model to interpret experimental results using porous mica membranes. Toyoshima et al.

(26) used the TMS theory to calculate the membrane resistance but neglected any electroosmotic contribution to the pore fluid conductivity.

Drost-Hansen et al. (27,28) considered the increase of the pore fluid conductivity to be primarily due to changes in the solvent (water) structure near the solid surface. This change in the solvent structure was viewed as extending much further into the electrolyte solution near the solid-liquid interface than the electrical double layer. However, the ion-wall electrostatic interactions are much longer range than the polar solvent-wall interactions. According to recent calculations (29), these wall-solvent interactions should have only a secondary effect and, should be confined to a region not extending more than a few solvent diameters away from the surface. This latter view was supported by experimental work by Anderson and Quinn (30) on the ionic mobility within well-characterized microcapillaries. The same conclusion was reached by Bean (31), whose experiments on diffusion and flow through fine, well-characterized pores indicated that the structure and dynamics of water are those of the bulk within about 1.0 nm from the solid surface.

Levine et al. (12) developed an approximate solution for the Poisson-Boltzmann equation and used it to calculate the electric current through a charged circular pore. This approach was also used by Anderson and Koh (32) to calculate the electroosmotic coefficient inside a charged pore, and by Van der Put and Bijsterbosch (33) to calculate the electrical resistances of their membranes. Finally, we (2,15) have used the space-charge model for electrokinetics through porous media to calculate the pore fluid conductivity for aqueous and nonaqueous electrolyte solutions, and found good agreement between the model and experiments using mica membranes.

The pore fluid conductivity is found from the electrical current generated by an applied electrical potential passed through the porous membrane. The conductivity is the inverse of the resistivity of the pore. Appropriately averaging the transport equations (Chapter 2) over the pore cross section gives

$$\kappa = ze^2 C_b \langle U_- e^{\Psi} + U_+ e^{-\Psi} \rangle + \frac{2\varepsilon C_b kT}{z\eta} \langle (\Psi(1) - \Psi)\sinh\Psi \rangle \tag{4-1}$$

where the brackets < > denote an area average over the pore cross section (2).

Here we examine the predictions of the space-charge model of electrokinetics for the electrical conductivity of a porous membrane. Because a constant pore wall charge and a constant pore wall potential imply very different electrostatic behavior, we examine both here and compare their effects on predictions. Since wall charge densities and wall potentials can always be mutually converted using diffuse double layer theory, either approach does not imply any mathematical limitations. The results of the model are also compared to the pore fluid conductivity calculated when approximate analytical solutions of the Poisson-Boltzmann equation (see Appendix C) inside a pore are applied

(12,14). Finally, Bikerman's and Schmid's models are compared to the space-charge model results.

4.2 Approximate Solutions of the Model Equations

Analytical results for the pore conductivity are given below for the cases when the low potential approximation fills the whole pore (subdomain I in Appendix C), or when the high potential approximation fills the whole pore (subdomain III). Within these two subdomains the evaluation of the pore fluid conductivity is straightforward. When neither approximation applies throughout the pore (subdomain II), numerical methods must be used to evaluate the area averages in equation (4-1).

Low Potential Approximation

For the low potential approximation in a circular pore, two analytical solutions for the pore conductivity are possible depending on whether the wall potential boundary condition (2-7a) or the wall charge condition (2-7b) is used.

Wall Potential Boundary Condition

$$\kappa_p^L = e^2 C_b z\left[U_+ + U_-\right] - 2e^2 C_b z\left[U_+ - U_-\right]\frac{\Psi(1)}{a/D}\,\frac{I_1(a/D)}{I_0(a/D)} \tag{4-2}$$

$$+\; e^2 C_b z\left[U_+ + U_-\right]\Psi(1)^2\,\frac{I_0^2(a/D) - I_1^2(a/D)}{I_0^2(a/D)}$$

$$+\; \frac{4\varepsilon C_b kT}{\eta}\left[\frac{\Psi(1)^2}{a/D}\,\frac{I_1(a/D)}{I_0(a/D)} - \frac{\Psi(1)^2}{2}\,\frac{I_0^2(a/D) - I_1^2(a/D)}{I_0^2(a/D)}\right]$$

Wall Charge Boundary Condition

$$\kappa_c^L = e^2 C_b z\left[U_+ + U_-\right] - 2e^2 C_b z\left[U_+ - U_-\right]\frac{S_w}{(a/D)^2} \tag{4-3}$$

$$+\; e^2 C_b z\left[U_+ + U_-\right]\left[\frac{S_w}{a/D}\right]^2\frac{I_0^2(a/D) - I_1^2(a/D)}{I_1^2(a/D)}$$

$$+\; \frac{4\varepsilon C_b kT}{\eta}\left[\frac{S_w^2}{(a/D)^3}\,\frac{I_0(a/D)}{I_1(a/D)} - \frac{S_w^2}{2(a/D)^2}\,\frac{I_0^2(a/D) - I_1^2(a/D)}{I_1^2(a/D)}\right]$$

High Potential Approximation

As with the low potential approximation, the high potential approximation has two analytical solutions, depending on which boundary condition at the wall is used.

Wall Potential Boundary Condition

$$\kappa_p^H = e^2 C_b z U_+ \frac{16}{(a/D)^2}\,\frac{1}{B-1} \tag{4-4a}$$

$$- \frac{\varepsilon C_b kT}{\eta}\,\frac{16}{(a/D)^2}\,\frac{1}{B-1}\left[\Psi(1) - \ln\frac{(a/D)^2}{16B} - 2\left\{B\ln\frac{B-1}{B} + 1 + \frac{1}{2}\ln(-B)^2\right\}\right]$$

$$B = \frac{[4\exp(\Psi(1)) + (a/D)^2]^{\frac{1}{2}} + 2[\exp(\Psi(1))]^{\frac{1}{2}}}{[4\exp(\Psi(1)) + (a/D)^2]^{\frac{1}{2}} - 2[\exp(\Psi(1))]^{\frac{1}{2}}} \tag{4-4b}$$

Wall Charge Boundary Condition

$$\kappa_c^H = -4e^2 C_b z U_+ \frac{S_w}{(a/D)^2} \tag{4-5}$$

$$- \frac{8\varepsilon C_b kT}{\eta}\,\frac{S_w}{(a/D)^2}\left[1 + \frac{4}{S_w}\ln\left(\frac{4-S_w}{4}\right)\right]$$

The behavior of these approximate solutions for the pore fluid conductivity is discussed below.

4.3 Work by Others

For a slit pore consisting of two parallel solid surfaces separated by a distance 2d, Bikerman (18) found that for large values of the ratio of d to the Debye length (d/D) the pore fluid conductivity is

$$\kappa_p^B = ze^2C_b\left[U_+ + U_-\right] \tag{4-6}$$

$$+ \frac{1}{d}\left[\frac{2\varepsilon kTC_b}{z^2e^2}\right]^{\frac{1}{2}}\left[\exp\left(-\frac{\Psi(1)}{2}\right) - 1\right]\left[ze^2U_+ + \frac{2\varepsilon kT}{\eta}\right]$$

$$+ \frac{1}{d}\left[\frac{2\varepsilon kTC_b}{z^2e^2}\right]^{\frac{1}{2}}\left[\exp\left(+\frac{\Psi(1)}{2}\right) - 1\right]\left[ze^2U_- + \frac{2\varepsilon kT}{\eta}\right]$$

The first term in equation (4-6) represents the bulk fluid conductivity, while the other two terms represent the so-called surface conductivity arising from the cation and the anion and are the result of the excess or the depletion, respectively, of the ion concentrations inside the double layer, with each term multiplied by the sum of the contributions of the ionic and the electroosmotic mobilities. This surface conductivity is the result of ions in the pore fluid and not just at the wall-fluid interface.

Schmid analyzed the conductivity of circular pores by using the TMS theory to calculate the ionic concentrations inside the pore. For Schmid's analysis, the size of the circular cylindrical pore must be assumed to be large compared to the Debye length. The pore fluid conductivity is taken to be the result of two contributions: the conductivity of the ions inside the pore, and the convective (electroosmotic) conductivity caused by a translation of the electrically charged pore fluid relative to the pore wall (1:1 electrolyte assumed)

$$\kappa_p^S = e^2\left[U_+C_+ + U_-C_-\right] + e^2A^2D_h \tag{4-7}$$

where C_i is the concentration of the mobile species "i" in the pore given by the TMS theory (equations (3-1a) to (3-1c) in Chapter 3), and D_h is the mechanical permeability of the membrane

$$D_h = \frac{n_a \pi a^4}{8\eta} \tag{4-8}$$

with n_a being the number of pores per unit membrane area.[1] Equation (4-8) was derived with the oversimplification that there is parabolic flow inside the pore. Figure 4-1 compares a dimensionless velocity profile calculated from the space-charge model

$$v_x(x_p)/(\varepsilon kT/e\eta)(dV/dx) \equiv \Psi(1) - \Psi(x_p) \tag{4-9a}$$

to a parabolic flow with the same maximum velocity U_{max}

$$u(x_p) = U_{max}\left(1-x_p^2\right) \tag{4-9b}$$

---

[1] We take $n_a = 1$ since we are considering only one pore here.

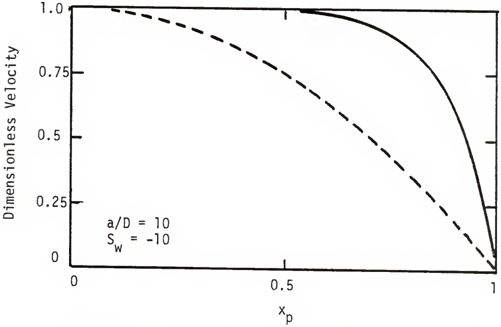

Figure 4-1 Comparison of dimensionless velocity profiles in a cylindrical pore ——— Space-charge model. ----- Parabolic flow. Both profiles have the same maximum velocity.

The two profiles give a completely different picture of flow in the pore. It deserves note that in Schmid's model the contribution of the electroosmotic term in equation (4-7) to the overall conductivity was at least 10 orders of magnitude less than the migration term for all our calculations. Such was not the case for the space-charge model, as discussed below.

4.4 Results and Discussion

This section examines the predictions of the space-charge model for the pore fluid conductivity, and compares them with the approximating solutions as well as with the predictions of the models by Bikerman and Schmid. The ionic diffusivities used in all calculations were $D_+ = D_- = 2\times10^{-9} m^2/s$, as for aqueous KCl, the characteristic pore cross sectional dimension (a or d) was taken to be 10 nm, and the pore walls were taken to be negatively charged. The use of electrolytes with different diffusivities, such as LiCl or NaCl, as well as the use of a different pore size or pore wall polarity does not change the qualitative features of the results presented.

Space-Charge Model

The predictions of the space-charge model using a constant wall potential or a constant wall charge boundary condition are very different, as shown in Figure 4-2 where the space-charge model predictions for pore conductivity are plotted for both boundary conditions. At high electrolyte concentrations the model predictions using either boundary condition approach the bulk solution conductivity. When the

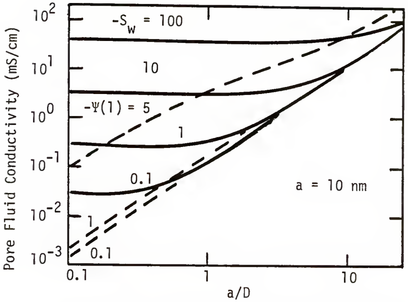

Figure 4-2 Comparison of the space-charge model pore fluid conductivity predictions when different boundary conditions are used.
——— Constant wall charge boundary condition.
------Constant wall potential boundary condition.

wall charge boundary condition is used, the space-charge model predictions for the pore fluid conductivity achieve a constant value at low electrolyte concentrations. On the other hand, when the wall potential boundary condition is used, the model predictions for the pore fluid conductivity approach zero at low electrolyte concentrations.

For either boundary condition, the space-charge model predictions for the pore fluid conductivity at low electrolyte concentrations approach the limit:

$$\lim_{a/D\to 0} \kappa = z_+\left\{e^2U_+<C_+> - \frac{\varepsilon kT}{\eta}<C_+(\Psi(1)-\Psi)>\right\} \tag{4-10}$$

The first term results from the presence of counterions in the pore, where $z_+e^2U_+$ is the counterion conductance. The second term is the electroosmotic contribution to the conductivity. In both terms of equation (4-10) the influence of the coions (negative here) is absent because coions are virtually excluded from the pore at low electrolyte concentrations. This limit for the pore conductivity strongly depends on the average counterion concentration $<C_+>$ in the pore, which in turn depends on the electrostatic potential profile. When the wall charge boundary condition is used, changing a/D dramatically changes the potential profile in the pore. However, at low concentrations, since the wall charge is constant, the concentration of excess counterions $<C_+>$ inside the pore that balance the pore wall charge reaches a constant limiting value, i.e. $<C_+>$ becomes constant. At very low wall charges (e.g. $|S_w| < 1.0$) this limiting value can be reached only at extremely low dilutions. On the other hand, when the constant wall potential boundary condition is used, changing a/D does not significantly affect the potential profile at low electrolyte concentrations. Furthermore, when the constant wall potential condition is used, the predicted pore wall charge decreases as the electrolyte concentration decreases, and as a result the value of $<C_+>$ decreases monotonically as the electrolyte concentration decreases. These conclusions concerning $<C_+>$ are supported by the calculations in Tables 4-1 and 4-2. The electroosmotic contribution to the conductivity in equation (4-10) is also shown in Tables 4-1 and 4-2. As the electrolyte concentration decreases, this contribution approaches a constant value when the constant wall charge condition is used, and it approaches zero when the constant wall potential condition is used. Hence, as the bulk electrolyte concentration decreases, the space-charge model predictions for the pore fluid conductivity approach a limiting value when the wall charge boundary condition is used, but approach zero when the wall potential boundary condition is used.

Table 4-3 shows the ratio of the convection to migration contributions to the pore conductivity at different electrolyte concentrations for both boundary conditions (constant wall charge or constant wall potential). When the constant wall charge condition is used this ratio decreases as the electrolyte concentration increases. On the other hand, when the wall potential boundary condition is used, this ratio has a maximum for intermediate values of a/D. Table 4-3 also shows that at low values of the wall charge (or the wall potential) convective flow contributes insignificantly to the total conductivity.

Table 4-1
Constant Wall Charge Boundary Condition

S_w	a/D	$\Psi(1)^*$	$\Psi(0)^*$	$\langle C_+\rangle^{**}$	$\langle C_+(\Psi(1) - \Psi)\rangle^{**}$
-0.10	0.1	-3.71	-3.66	$3.72\text{x}10^{-4}$	$-9.16\text{x}10^{-6}$
	0.3	-1.55	-1.50	$3.90\text{x}10^{-4}$	$-9.60\text{x}10^{-6}$
	1.0	-1.78	-0.13	$1.40\text{x}10^{-3}$	$-3.30\text{x}10^{-5}$
-1.00	0.1	-6.21	-5.77	$3.72\text{x}10^{-3}$	$-7.99\text{x}10^{-4}$
	0.3	-4.00	-3.56	$3.72\text{x}10^{-3}$	$-7.99\text{x}10^{-4}$
	1.0	-1.45	-1.01	$4.08\text{x}10^{-3}$	$-8.66\text{x}10^{-4}$
-10.0	0.1	-9.55	-7.04	$3.72\text{x}10^{-2}$	$-3.71\text{x}10^{-2}$
	0.3	-7.34	-4.83	$3.72\text{x}10^{-2}$	$-3.71\text{x}10^{-2}$
	1.0	-4.69	-2.19	$3.72\text{x}10^{-2}$	$-3.72\text{x}10^{-2}$
-100.	0.1	-13.81	-7.34	$3.89\text{x}10^{-1}$	$-5.99\text{x}10^{-1}$
	0.3	-11.60	-5.13	$3.89\text{x}10^{-1}$	$-5.99\text{x}10^{-1}$
	1.0	-8.95	-2.48	$3.89\text{x}10^{-1}$	$-5.99\text{x}10^{-1}$

*: calculated quantities
**: in mol/dm^3

Table 4-2

Constant Wall Potential Boundary Condition

$\Psi(1)$	a/D	S_w^*	$\psi(0)^*$	$\langle C_+\rangle^{**}$	$\langle C_+(\psi(1) - \psi)\rangle^{**}$
-0.01	0.1	-5.00×10^{-5}	-9.90×10^{-3}	9.40×10^{-6}	-1.17×10^{-10}
	0.3	-4.50×10^{-4}	-9.80×10^{-3}	8.55×10^{-5}	-9.58×10^{-9}
	1.0	-5.60×10^{-3}	-7.40×10^{-3}	1.21×10^{-3}	-1.61×10^{-9}
-0.10	0.1	-5.00×10^{-4}	-9.90×10^{-2}	1.03×10^{-5}	-1.28×10^{-9}
	0.3	-4.50×10^{-3}	-9.80×10^{-2}	9.35×10^{-5}	-1.05×10^{-7}
	1.0	-5.60×10^{-2}	-7.41×10^{-2}	1.30×10^{-3}	-1.73×10^{-5}
-1.00	0.1	-5.86×10^{-3}	-9.97×10^{-1}	2.52×10^{-5}	-3.70×10^{-8}
	0.3	-5.26×10^{-2}	-9.74×10^{-1}	2.27×10^{-4}	-2.96×10^{-6}
	1.0	-6.22×10^{-1}	-7.20×10^{-1}	2.83×10^{-3}	-3.92×10^{-4}
-5.00	0.1	-3.42×10^{-1}	-4.84×10^{0}	1.27×10^{-3}	-1.03×10^{-4}
	0.3	-2.18×10^{0}	-4.13×10^{0}	8.13×10^{-3}	-3.28×10^{-3}
	1.0	-1.20×10^{1}	-2.23×10^{0}	4.46×10^{-2}	-4.79×10^{-2}

*: calculated quantities

**: in mol/dm^3

Table 4-3
Comparison of the Ratio of Convection to Migration Terms

a/D	$S_w = -0.1$	$\Psi(1) = -0.1$	$S_w = -5.0$	$\Psi(1) = -5.0$
0.1	6.33×10^{-3}	3.21×10^{-6}	1.81×10^{-1}	2.08×10^{-2}
0.2	6.06×10^{-3}	1.85×10^{-5}	1.81×10^{-1}	8.00×10^{-2}
0.6	3.14×10^{-3}	9.90×10^{-5}	1.81×10^{-1}	1.89×10^{-1}
1.4	5.49×10^{-4}	3.65×10^{-4}	1.75×10^{-1}	3.02×10^{-1}
3.4	5.95×10^{-5}	4.88×10^{-4}	9.26×10^{-2}	3.65×10^{-1}
8.3	4.50×10^{-6}	2.71×10^{-4}	1.07×10^{-2}	3.07×10^{-1}
20.0	3.18×10^{-7}	1.22×10^{-4}	7.91×10^{-4}	1.57×10^{-1}
25.0	1.65×10^{-7}	9.80×10^{-5}	4.06×10^{-4}	1.23×10^{-1}

However, at high values of the wall charge (or the wall potential) the contribution of the convective flow may not be negligible.

Our experimental experience with porous mica membranes (2,15) shows that at low concentrations the measured values of the pore fluid conductivity do not go to zero, as the constant wall potential boundary condition suggests. The solid lines on Figure 4-3 are calculations from the space-charge model using the constant wall charge and the constant wall potential boundary conditions. The experimentally determined pore fluid conductivity in Figure 4-3 levels off at low electrolyte concentrations and is orders of magnitude larger than the bulk fluid conductivity outside the pores (dashed curve). Similar conclusions were reached by Van der Put and Bijsterbosch (33), who used polystyrene membranes for experiments. The trend of the available experimental data, when compared to predictions with the space-charge model, lead us to conclude that the constant wall charge boundary condition is usually preferable to the constant wall potential condition.

High and Low Potential Approximations

Because the pore fluid conductivity in the space-charge model, as presented above, requires somewhat tedious numerical calculations, approximate analytical solutions for the pore fluid conductivity have been derived (see equations (4-2) to (4-5)). When the wall potential is specified as a boundary condition, the ranges of applicability of the analytical solutions are quite clear: when the dimensionless potential at the centerline of the pore is greater than unity the high potential approximation applies, and when the centerline potential is

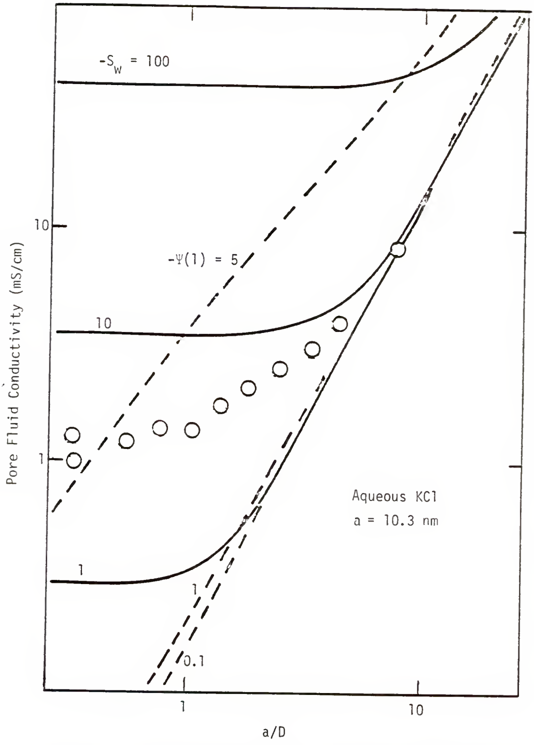

Figure 4-3 Comparison of aqueous KCl pore fluid conductivity experimental data to space-charge model predictions. ——— wall charge boundary condition. ----- wall potential boundary condition.

less than unity the low potential approximation applies. When the pore wall charge is specified as a boundary condition, the ranges of applicability of the high and low approximating analytical solutions have been presented elsewhere (14), and are shown in Chapter 5.

For a range of values of the dimensionless wall charge S_w, Figure 4-4 compares the pore fluid conductivity for the space-charge model and for the high and low potential analytical approximations. The dashed portions of the curves are regions in which the analytical solutions do not apply. The "exact" predictions in Figure 4-4 were made by solving the Poisson-Boltzmann equation using a fourth order Runge-Kutta method. For all S_w values in Figure 4-4, the high potential approximating solution is an excellent estimator for the pore fluid conductivity at low electrolyte concentrations, while the low potential approximation gives predictions identical to the "exact" solution at high electrolyte concentrations. At low electrolyte concentrations, the low potential approximation deviates tremendously from the exact solution, as does the high potential approximation at large electrolyte concentrations. The high potential approximation (see equation (4-4)) is independent of the bulk electrolyte concentration. On the other hand, the low potential approximation (equation (4-3)) is strongly dependent on the electrolyte concentration, and shows a minimum at intermediate values of the ratio of the pore radius to the Debye length, above which it rapidly approaches the behavior of the exact solution, that is, it approaches the bulk solution conductivity.

For the constant wall potential boundary condition, Figure 4-5 compares the pore fluid conductivity from the exact solution and from

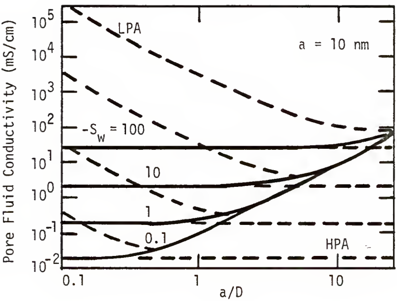

Figure 4-4 Space-charge model predictions for the pore fluid conductivity when the wall charge boundary condition is used. The numerical solution (————) is compared to the low (LPA) and high (HPA) potential approximations (------).

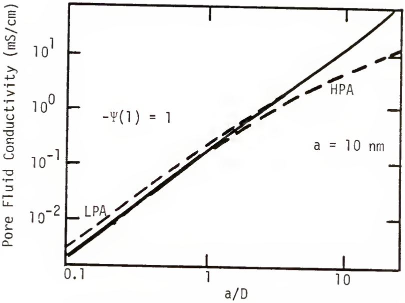

Figure 4-5 Space-charge model predictions for the pore fluid conductivity when the wall potential boundary condition is used. The numerical solution (———) is compared to the low (LPA) and high (HPA) potential approximations (-------).

the high and low potential approximations for a constant value of the wall potential. The dashed curves are regions in which these approximations do not apply. As with the constant wall charge boundary condition, the low potential approximation agrees well with the exact solution at high electrolyte concentrations while the high potential approximation agrees well with the exact solution at low electrolyte concentrations. At high electrolyte concentrations the low potential approximation always approaches the bulk solution conductivity. As expected, for much lower values of the constant wall potential than in Figure 4-5, the low potential approximation coincides with the bulk solution conductivity for the entire range of the electrolyte concentrations examined. For higher values of the wall potential than in Figure 4-5, the high potential approximation approaches the exact solution except at high electrolyte concentrations.

Other Models

The model developed by Schmid (23) for the pore fluid conductivity (equation (4-7)) is compared with the predictions from the space-charge model in Figure 4-6. The models predict similar trends for the pore fluid conductivity and both approach the bulk solution conductivity at high electrolyte concentrations. At low electrolyte concentrations, both models approach constant values. However, these limiting values differ for the two models at large wall charge values ($|S_w| > 1$). The reason for these discrepancies is that different radial concentration profiles are calculated for each model. Both models satisfy the electroneutrality condition inside the pore, but while the space-charge

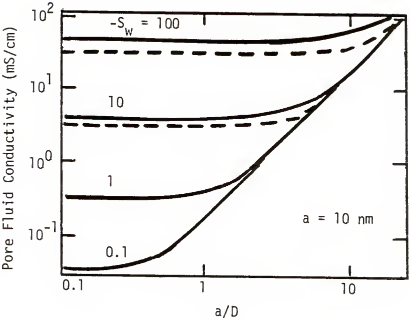

Figure 4-6 Comparison of the space-charge model predictions (————) to Schmid's model predictions (-------) for the pore fluid conductivity.

model attempts to account for the effects of the ion-pore wall electrostatic interactions, the model by Schmid ignores them. These interactions cause the intrapore ionic concentrations to vary radially within the pore at any cross section. Schmid's approach is based on the TMS theory (8,9,10,11) which assumes a uniform ionic concentration profile within the pore at any cross section (see equations (3-1) and (3-2)). At high electrolyte concentrations, most of the pore fluid is virtually unaffected by the wall charge. At low electrolyte concentrations, the models agree only when the value of the wall charge is $|S_w| < 10$ (34). It should be mentioned that, according to Schmid's model, the convection contribution to the overall conductivity (second term in equation (4-7)), is predicted to be concentration independent. Furthermore, the electroosmotic contribution in Schmid's model is always orders of magnitude lower than the electroosmotic contribution calculated from the space-charge model.

Figure 4-7 compares the predictions of Bikerman's model, which uses an infinite slit pore, with the space-charge model, also calculated using an infinite slit. Because the pore conductivity in both models approaches the bulk electrolyte solution conductivity as the wall potential goes to zero, identical results are obtained at low wall potentials. At low values of the dimensionless wall potential, the two models predict identical pore conductivities for a large range of concentrations. However, as the wall potential increases, the predictions of the two models begin deviating from each other, especially at low concentrations. This is the result of the assumption made in Bikerman's derivation that the centerline potential for all values of

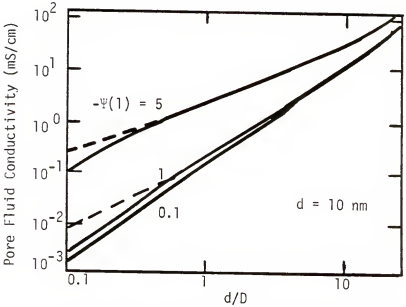

Figure 4-7 Comparison of the space-charge model predictions for the pore fluid conductivity in an infinite slit (————) to Bikerman's model predictions (-------).

d/D is zero, thereby restricting the applicability of the model to large electrolyte concentrations only. It should be mentioned that, if the cation mobility is taken to be less than the anion mobility, for a negative wall, the difference between the pore and bulk fluid conductivities for Bikerman's model (see equation (4-6)) is negative in sign, which is opposite to the sign of this difference for the space-charge model. In addition, using a slit with the same pore surface area to volume ratio as that of a cylindrical pore does not improve the ability of Bikerman's model to approach the results of the space-charge model for cylindrical pores.

4.5 Conclusions

Predictions of the pore fluid conductivity using the high potential approximation are adequate only at low electrolyte concentrations, while the low potential approximation is adequate only for high electrolyte concentrations. When special care is taken not to use the approximate solutions when they are not applicable, combining the high and low potential approximations can be a powerful and simple method for estimating the pore fluid conductivity for a wide range of concentrations. These approximating methods can be easily used by experimentalists who do not wish to use the strenuous numerical methods required for the space-charge model. In addition, while using the wall potential as a boundary condition is somewhat easier than using the wall charge, one must recognize that the available experimental data more closely resemble calculations using a constant wall charge than those using a constant wall potential.

Schmid's model, despite its simplistic approach to the calculation of the fluid flow inside the pore, can be applied in the whole range of concentrations examined for small values of the wall charge ($|S_w| < 10$). While Schmid's model is easy to use for routine calculations within the range of its applicability, it is more complicated than the approximate solutions to the space-charge model presented here. Bikerman's approach, because of its assumptions, is restricted to large electrolyte concentrations and small wall potential values.

CHAPTER 5
THE STREAMING POTENTIAL AND INADEQUACIES OF THE HELMHOLTZ EQUATION

5.1 Introduction

The streaming potential is among the most convenient techniques for determining the magnitude and polarity of the surface charge density of a system with a large surface-to-volume ratio. For example, Jacazio et al. (35) measured the charge on soils using the streaming potential. Briggs checked the surface charge of albumin-coated quartz particles obtained from electrophoretic mobility measurements with streaming potential data for an albumin-coated diaphragm made of quartz powder (36,37). The streaming potential is found by applying a pressure ($P_{II} - P_I$) across a porous medium and by measuring the resulting electrical potential ($V_{II} - V_I$) with electrodes in the bulk electrolyte solutions outside the porous medium (see Figure 2-2).

Despite the ease with which they can be measured, streaming potentials are often misinterpreted. Usually implicit in the analysis of streaming potential data is the assumption that the Debye length of the solution filling pores is small compared to the average cross section for flow through pores. The well-known Helmholtz expression for the streaming potential is then used to obtain the electrostatic condition of the pore wall

$$\nu \equiv \frac{\Delta V_s}{\Delta P} = \frac{\varepsilon}{\eta \kappa_b} \psi(1) \qquad (5\text{-}1)$$

where the conductivity of the solution inside pores is typically assumed to be the bulk conductivity κ_b of the solution outside the porous medium. Since the Debye length is a rough measure of the thickness of the diffuse part of the double layer near a charged interface, the assumption of a thin double layer implies that ions in the diffuse layer interact with the charged interface as if it were a flat surface. Hence, the electrostatic potential at the wall is assumed to be related to the pore wall charge density by the flat interface result from Gouy-Chapman theory

$$\sigma_w = \frac{2\varepsilon kT}{zeD} \sinh\left(\frac{ze\psi(1)}{2kT}\right) \qquad (5\text{-}2)$$

where equation (5-2) is for a z:z electrolyte, and SI units are used. Equations (5-1) and (5-2) have often been used to determine the wall charge density in charged porous media (36,38,39). However, note that the Helmholtz limit (equations (5-1) and (5-2)) contains no information about the size of pores.

Since the streaming potential is the electromotive potential difference generated by an applied pressure difference at zero current across the membrane, appropriately averaging the transport equations (equations (2-12a) to (2-12c)) over the pore cross section gives (2)

$$\nu \equiv \left(\frac{\Delta V_s}{\Delta P} \right) = \frac{-L_{31}}{L_{33}} \qquad (2\text{-}15)$$

The Helmholtz expression for the streaming potential in equation (5-1) is derived by considering the limit of a/D approaching infinity, in which case the coefficients L_{31} and L_{33} become

$$L_{31} \rightarrow \frac{\varepsilon\psi(1)}{\eta} \qquad (5\text{-}3a)$$

$$L_{33} \rightarrow -\kappa_b \qquad (5\text{-}3b)$$

Substituting these asymptotic results into (5-2) gives the Helmholtz result in equation (5-1). Solving (2-1) for a planar geometry, with the condition (2-7b) and with the potential set equal to zero far from the wall, relates the wall charge density to the wall potential as in equation (5-2). By determining the streaming potential experimentally and applying equations (5-1) and (5-2), the charge density of a porous medium can be estimated (36,38,39). What is often forgotten is that this procedure is correct only when the pore radius is much larger than the Debye length.

The conditions under which the Helmholtz expression does not apply are illustrated in Figure 5-1. The data (2) are for aqueous KCl in pores with a radius of 10.3 nm. The Helmholtz equation (dashed curves) predicts much higher values of the streaming potential than are found experimentally at low electrolyte concentrations or low a/D. The theoretical results for the streaming potential (solid curves) were

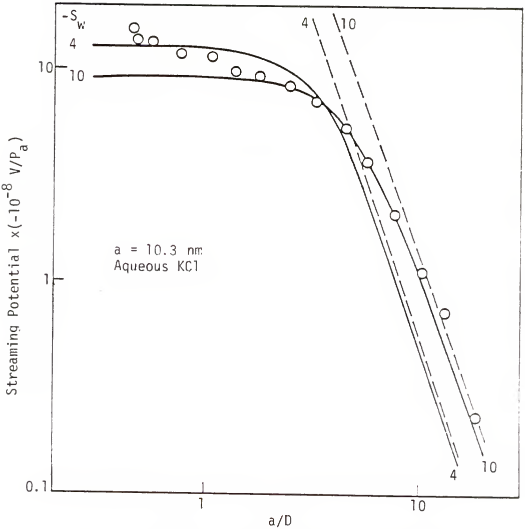

Figure 5-1 Streaming potential data for KCl in a = 10.3nm pores. ——— Space-charge model predictions. ----- Helmholtz limit.

obtained using the space-charge model discussed in Chapter 2. At low concentrations streaming potentials predicted with the model (solid curves) actually decrease as the wall charge density S_w increases for the range of S_w values shown, and in the range from $1 \leq a/D \leq 3$, the uniqueness of the wall charge predicted with streaming potential measurements disappears. This contradicts the insight provided by the Helmholtz limit, equations (5-1) and (5-2).

Discrepancies between the Helmholtz limit and experiments are a result of two assumptions implicit in equations (5-1) and (5-2). First, the diffuse layer may not be much smaller than the average cross section for flow in a pore. The Debye length is proportional to the square root of the bulk concentration (C_b), and as the concentration decreases the diffuse layer may fill the entire pore, which obviates the assumption of a flat double layer. Second, the conductivity of the solution inside pores may be much larger than the conductivity of the bulk solution outside pores (see Chapter 4), and the Helmholtz limit does not take into account the enhancement of the electrical conductivity of the fluid inside pores. It has been shown (2,40) that experimentally measured pore conductivities can be orders of magnitude larger than bulk solution conductivities. This enhancement of the pore conductivity occurs because the charge on the pore walls is balanced by an excess of counterions in the solution inside pores. At low concentrations, this excess forces the concentration of ions in pores to be much larger than the bulk electrolyte concentration, which in turn forces the pore fluid conductivity to be much larger than the bulk conductivity. To clarify the behavior of the streaming potential, the following section discusses the model that was used to compute the solid curves in Figure 5-1. Later sections compare the Helmholtz limit with this model. Finally, it should be mentioned that, although this Chapter deals with positive pore walls, this affects only the sign of the quantities calculated.

5.2 Approximate Solutions of the Model Equations

One reason for the wide currency enjoyed by the Helmholtz expression is that calculations using this equation are simple. Unfortunately, there is no generally applicable analytical solution of the Poisson-Boltzmann equation (equation (2-1)) for circular cylindrical pores. However, the approximate analytical solutions to the Poisson-Boltzmann equation in Appendix C can be used for the analytical evaluation of the coefficients L_{31} and L_{33}.

Analytical results for the streaming potential are given below for the cases when the low potential approximation fills the whole pore (subdomain I in Appendix C), or when the high potential approximation fills the whole pore (subdomain III). Within these two subdomains the evaluation of the streaming potential is straightforward. In subdomain II, where neither of the approximations applies throughout the entire pore, numerical methods must be used to evaluate the coefficients. The Helmholtz equation is also compared below with the low and high potential approximations. To simplify this comparison, we define a dimensionless streaming potential Y, which is a function of the wall charge density (S_w) and the bulk electrolyte concentration

$$Y \equiv \left(\frac{ze\eta\kappa_b}{\varepsilon kT}\right)\nu \tag{5-4}$$

Low Potential Approximation

In subdomain I we define Y^*_{LP} as

$$Y_{LP} = \left(\frac{a}{D}\right)^2 Y^*_{LP} \tag{5-5a}$$

where the dimensionless streaming potential Y^*_{LP} is

$$Y^*_{LP} = \frac{S_w}{(a/D)^3}\frac{I_0(a/D)}{I_1(a/D)}\left[1 - \frac{2}{(a/D)}\frac{I_1(a/D)}{I_0(a/D)}\right] \tag{5-5b}$$

I_j is the modified Bessel function of the first kind and order "j." Since the dimensionless electrostatic potential inside the pore must be less than unity for the low potential approximation to apply, equation (5-5b) is accurate only when

$$\frac{a}{D}\frac{I_1(a/D)}{I_0(a/D)} \geq S_w \tag{5-5c}$$

Y_{LP} is proportional to S_w, and equation (5-5b) has an error of order S_w^3 associated with it. For very small a/D values, Y_{LP} approaches the limit $0.25S_w$.

High Potential Approximation

The dimensionless streaming potential in subdomain III is

$$Y_{HP} = \left(\frac{a}{D}\right)^2 Y^*_{HP} \tag{5-6a}$$

$$Y^*_{HP} = \frac{F(S_w)}{G(S_w)} \tag{5-6b}$$

$$F(S_w) = \left(\frac{4 + S_w}{S_w}\right) \ln\left(\frac{4 + S_w}{4}\right) - 1 \tag{5-7a}$$

$$G(S_w, B_D) = S_w\left[1 + B_D\left(\frac{4}{S_w} \ln\left(\frac{4}{S_w + 4}\right) + 1\right)\right] \tag{5-7b}$$

$$B_D = \frac{4\varepsilon(kT/e)^2}{zn(D_+ + D_-)} \tag{5-7c}$$

To assure that the dimensionless potential at the centerline is greater than unity, the following condition must be met

$$a/D \leq 2.462(S_w/(S_w + 4))^{1/2} \tag{5-8}$$

Changing B_D (i.e., changing the electrolyte) affects Y^*_{HP} only slightly. The limiting values of Y^*_{HP} in terms of S_w are

$$S_w \rightarrow 0: \quad Y^*_{HP} \rightarrow 0.125 \tag{5-9a}$$

$$S_w \rightarrow \infty: \quad Y^*_{HP} \rightarrow \left[\frac{S_w^{-1}}{(B_D + 1)}\right] \ln(S_w/4) \tag{5-9b}$$

Since Y^*_{HP} is a decreasing function of S_w and approaches zero at very large values of the wall charge, the high potential approximation predicts that, for a given a/D the magnitude of the streaming potential decreases as S_w increases. Note that Y^*_{HP} depends only on S_w and B_D and is independent of the ratio of the pore radius to the Debye length.

Helmholtz Limit

Combining equations (5-1) to (5-2) with the definition of Y in (5-4) we have the following for the Helmholtz limit

$$Y_{FP} = 2\sinh^{-1}\left[\frac{S_w}{2(a/D)}\right] \tag{5-10}$$

where the subscript FP stands for "flat plate" to emphasize that this relationship is strictly valid only when the pore wall is flat on the scale of the double layer thickness. Y_{FP} is quite sensitive to a/D at low S_w values but becomes less sensitive at high wall charge values.

5.3 Comparison of Approximate Solutions

The low potential, high potential, and Helmholtz approximations for the streaming potential have a similar form, and in this section we compare the predictions of the these approximations for the dimensionless streaming potential Y as defined in equation (5-4). The values of the ionic diffusivities used for all calculations were $D_+ = D_- = 2.0\text{x}10^{-9}\ m^2/s$. The ranges of applicability of the high and low potential approximating solutions, given by equations (5-5c) and (5-8) are shown in Figure 5-2.

Figure 5-3a compares Y for the high potential, low potential, and Helmholtz approximations for one a/D value. The dashed portions of the curves for Y_{HP} and Y_{LP} are regions in which these approximations do not apply (see Figure 5-2). For the range of S_w values shown in Figure 5-3a, the solid curves for Y_{HP} and Y_{LP} are excellent approximations except near their junction, and they compare favorably with numerical computations for Y (see below). Note that Figure 5-3a implies that there is a maximum in the dimensionless streaming potential Y because Y_{HP} decreases as S_w increases.

The Helmholtz approximation Y_{FP} is also shown in Figure 5-3a. At low S_w values, Y_{FP} is parallel to Y_{LP}. This is true for all a/D (for example, see Figure 5-3b). In Figure 5-3b, the solid portions of the curves for Y_{HP} and Y_{LP} are excellent approximations to the dimensionless streaming potential Y, and as in Figure 5-3a a maximum is indicated as S_w increases. For the moderately high a/D value in Figure 5-3b, Y_{FP} approaches Y_{LP} at low S_w values. However, Y_{FP} can never show

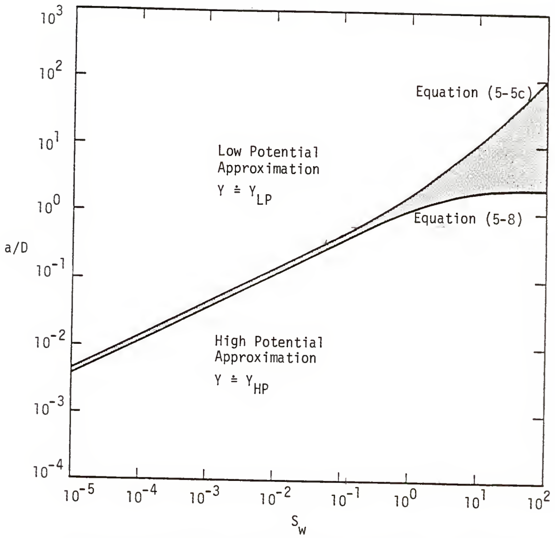

Figure 5-2 Regions of applicability of the low potential approximation (subdomain I) and the high potential approximation (subdomain III). In the shaded region, neither approximation applies.

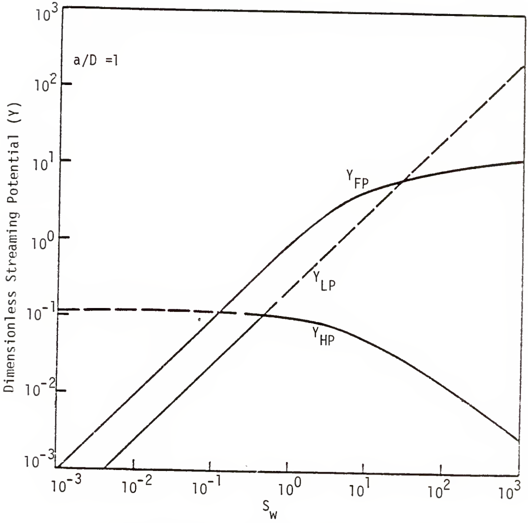

Figure 5-3 Comparison of the dimensionless streaming potential for the low potential, high potential, and Helmholtz (flat plate) approximations: (a) for a/D = 1

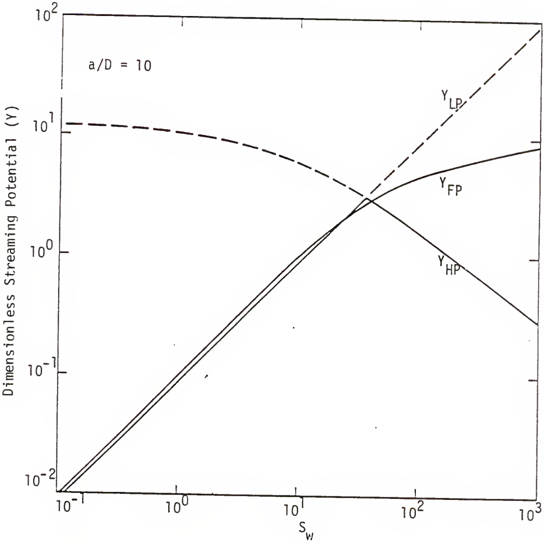

Figure 5-3 Continued: (b) for a/D = 10

a maximum in Y as S_w increases. Our computations have led us to conclude that Y_{FP} should be used only when $S_w < 10$ and $a/D > 10$.

The ease with which Y can be computed using Y_{HP} and Y_{LP} compares favorably with the ease of using the Helmholtz expression for Y_{FP}. Furthermore, the range of applicability of Y_{HP} and Y_{LP}, when used together as in Figures 5-3a and 5-3b, is considerably larger than the range of applicability of Y_{FP}. Nonetheless, one must be careful not to use Y_{HP} and Y_{LP} when they do not apply (see Figure 5-2). We have used a variety of numerical methods, including a Runge-Kutta technique and quasilinearization, to solve the Poisson-Boltzman equation for the potential distribution inside the pore. We have found a fourth-order Runge-Kutta routine having a Newton-Raphson shooting correction to one boundary condition to be the most convenient method for routinely obtaining "exact" numerical estimates for the potential distribution and hence Y.

These "exact" estimates are illustrated in Figure 5-4, where each solid curve is the result of calculations using the Runge-Kutta method for a particular a/D. As the pore wall charge S_w is increased, the streaming potential does not increase without limit but goes through a maximum. Note that the maximum in Y can be quite broad when the pore radius is smaller than the Debye length. Experimental investigators should keep the existence of this maximum in mind since a particular experimental determination of the streaming potential at a particular C_b could result in two estimates of the pore wall charge S_w.

The Helmholtz expression cannot predict the existence of a maximum in Y, and as noted above, the range of applicability of Y_{FP} is quite

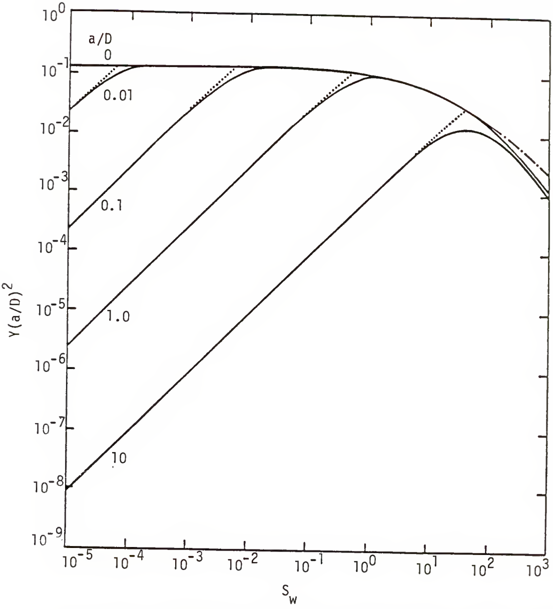

Figure 5-4 Dimensionless streaming potential $(Y/(a/D)^2)$ versus S_w for various a/D values. The electrolyte has ionic diffusivities of $D_+ = D_- = 2\times10^{-9}$ m^2/S. Numerical solutions for $\Psi(x_p)$ ———. Approximating solutions of equations (5-5) ……… and (5-7) -.-.-.

limited. The high and low potential approximations for Y, when used together as in Figure 5-3, have a much wider range of usefulness than Y_{FP}. But as already noted, Y_{HP} and Y_{LP} have their own limitations. Also shown as dashed curves in Figure 5-4 are the low and high potential approximations for Y. Over much of the range of S_w and bulk concentrations (or a/D) shown in Figure 5-4, these approximations coincide with the exact numerical calculations. In Figure 5-4 the dashed curves merely indicate those situations in which Y_{HP} and Y_{LP} do not apply, and these situations are adequately predicted by Figure 5-2.

In the Appendix C we discuss a matching solution (subdomain II) for Y between the ranges of applicability of Y_{HP} and Y_{LP}. We have found that this matching solution is relatively easy to use if its limitations are understood. The matching solution has been found to be especially useful when the region of inapplicability of Y_{HP} and Y_{LP} in Figure 5-2 is narrow, i.e., at low S_w and low a/D.

5.4 Conclusions

Figures 5-1 and 5-3 show that the Helmholtz equation is not correct for porous media when a/D is of order 10 or less. The full model, based on the Poisson-Boltzmann description of the double layer and the Nernst-Planck equations for the transport of ionic species, accounts for the enhanced conductance inside small pores (see Chapter 4). This enhanced conductance in turn causes the streaming potential to decrease as the pore wall charge density, or wall potential, increases in magnitude when the pore radius and the Debye length are comparable. As shown in Figure 5-4, the streaming potential exhibits a maximum as wall charge is varied, all other variables held constant. The Helmholtz equation, of course, predicts Y to be a monotonically increasing function of S_w and hence does not display such a maximum. These results suggest that a flag of caution be raised to experimenters who, working under conditions where the pore radius is of the same order of magnitude as the Debye length, such as with nonaqueous solvents, use the Helmholtz equation to deduce the electrostatic condition of the porous media from measured streaming potentials: besides yielding quantitatively incorrect estimates of surface charge, such a practice could imply a charging mechanism (increase in streaming potential) when actually the data are consistent with a discharging process.

The Helmholtz expression is accurate when the pore radius is much larger than the Debye length and when the charge on the pore wall is small. When the Helmholtz expression is invalid, the approximations Y_{LP} and Y_{HP} can be used with little error over a wide range of conditions, as shown in Figure 5-2. In the intermediate region, where neither of these approximations is valid, a numerical matching procedure, described in the Appendix C, can be used to compute the electrical potential within a pore, from which the dimensionless streaming potential can be obtained.

CHAPTER 6
EXPERIMENTS

6.1 Introduction

The space-charge model has been examined for strong 1:1 electrolytes in aqueous solvents, and the model has been found to be valid within the expected range of its applicability, that is, in dilute solutions up to 0.01-0.1 M. However, electrokinetic phenomena have rarely been examined for nonaqueous solvents, and the space-charge model has never been applied to electrokinetic effects in nonaqueous media. Because the verification of the space-charge model in aqueous media may have been fortuitous, and because the space-charge model has never been examined in nonaqueous media, it was important to examine the space-charge model experimentally in nonaqueous solvents. The first part of this chapter discusses the apparatus and the experiments for testing the space-charge model, presented in chapter 2, in nonaqueous solvents. The latter part of this chapter presents the results of preliminary electrokinetic experiments using LiCl in methanol-water mixtures. This preliminary set of experiments was done to explore whether electrokinetic experiments could be done in nonaqueous solvents. The nonaqueous experiments for the actual verification of the model are presented in the next chapter.

6.2 Apparatus

This section describes the mica membranes and the electrokinetic cell used for experiments. The electrolyte (LiCl) and the methanol used were reagent grade (Baker®). Deionized water with very low conductivity ($< 10^{-6}$ S/cm) was used.

Mica Membranes

The membranes used in experiments were made from mica sheets that were irradiated by a collimated Cf^{252} radiation source. Our Cf^{252} source is described in detail elsewhere (2). The fission-fragment tracks left on the mica sheet were etched in aqueous hydrofluoric acid, which attacked only the tracks (41). The thickness of a membrane, which was equal to the pore length ℓ because of fission fragment collimation, was determined very accurately from the weight of the membrane (42). Two membranes were irradiated at the same time in the irradiation chamber, one on top of the other. The top membrane was etched overnight, and the number of tracks on it were counted under a microscope. This count gave the number of fission fragments, and therefore the number of pores on the membrane (n), that had penetrated the bottom membrane, which was the one used in the experiments. The porosity of the membranes was always very low (less than 0.001%). Electronmicrographs of mica pores by Munch (43) show pores that are only slightly elliptical when the pore radious is as small as 30 nm. Much larger mica pores (44) are rhombohedral in shape. In addition, all pores have identical cross sections in a given membrane. The pore cross sectional area was very accurately measured using the resistance method described later in this section.

Electrokinetic Cell

The glass cell used in all experiments was made entirely from Pyrex® glass, Teflon®, and Viton®. A diagram of one half cell is shown in Figure 6-1. There were six ports in each glass half cell for inserting electrodes and valves for getting solutions into and out of the cell. The valves and electrode holders were made of Teflon®, and the gaskets that held a membrane were made of Viton®. The cell design is described in detail elsewhere (45), with two minor modifications made to the original design. The volume of the cell was larger, that is, with its gaskets, stirrers, valves, and electrodes in place, the cell contained V_c = 18.5 ml per half cell. Also, each magnetic stirrer was held by a hollowed out Teflon rod attached to a glass shaft that was in turn held by a threaded Teflon tube (Figure 6-2). The ends of the Teflon shell that contained the magnets were covered with Teflon 7A (Du Pont Corporation), ensuring no contact of the magnets with electrolyte solutions. The threaded tube that held the glass stirrer shaft was screwed to a Teflon stopper that fitted into the back of the glass half cell (Figure 6-1). The magnets were rotated by a large horseshoe magnet outside the cell. No glue of any kind was used in the cell. Electrodes made of Ag/AgCl were used because of their reversibility to the Cl^- ion in the solutions used (46,47). The electrodes were prepared by anodizing approximately 1 cm long Ag wires in 0.1 M aqueous

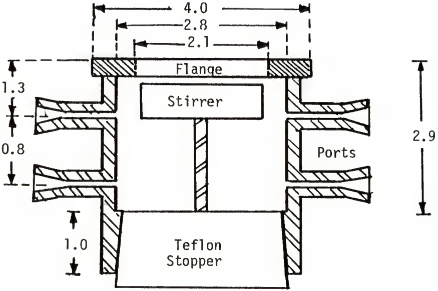

Figure 6-1 Glass half cell. All dimensions are in cm.

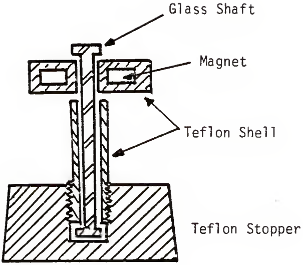

Figure 6-2 Electrokinetic half cell stopper.

KCl solutions with 1 mA each for 45 min. This gave us stable electrodes with low biases.

6.3 Experimental Test of the Model

The solution inside the cell was changed regularly and always before an experiment. At least five half cell volumes of new solution were put in each well stirred half cell to ensure complete exchange of the solution. Samples were always taken before and/or after each experiment. From the volume (V_s) and the electrolyte concentration (C_s) found in the sample the concentration inside the half cell (C_b) was calculated

$$C_b = C_{in} \pm \frac{(V_s/V_c)(C_s - C_{in})}{\exp(\pm V_s/V_c) - 1} \tag{6-1}$$

where + (or -) indicates that the sample was taken before (or after) the experiment. The concentration of the stock solution was C_{in}. The sample concentration was evaluated from the sample conductivity using the methods presented in the next Chapter. During all experiments, other than those done to characterize the mica wall charge, the bulk solution pH was kept in the range 7-10 with the addition of 10^{-4} M KOH (see Chapter 7). The temperature during all experiments was 25 ± 2 $^{\circ}$C.

Membrane Resistance and Pore Size

The resistance of the cell was found by applying a known current across electrodes on either side of the membrane, and by measuring the resulting electrical potential across the cell with a second pair of electrodes in the bulk solutions outside the membrane. The total resistance R_t of the cell determined in this way was

$$R_t = R_m + R_s \tag{6-2}$$

where R_m is the resistance of the membrane. The resistance of the solutions outside the membrane R_s was ignored because the porosity of the membranes was extremely low, so that R_m was much larger than R_s. The impedance of the electrometer for measuring the voltage across the membrane (Keithley Model 642) was several orders of magnitude larger than R_m. To cancel the effects of electrode biases several values of the current were passed in both directions through the membrane, and the average R_m was calculated. Currents as small as 0.5 nA were applied using a current source (Keithley Model 225). During experiments, the pressure in both cells was equilibrated by leaving one valve in each half cell open to the atmosphere.

The equivalent radius of cylindrical pores (a) was determined from the cell constant (K_c). The cell constant is the product of the pore fluid conductivity and the membrane resistance. At high ionic strengths the pore fluid conductivity approaches the bulk conductivity κ_b, and K_c is

$$K_c = \kappa_b R_m \tag{6-3a}$$

If n is the number of pores through the membrane and if ℓ is the pore length, then

$$a = \left(\frac{\ell}{n\pi K_c}\right)^{1/2} \tag{6-3b}$$

The membrane cell constant was experimentally determined using concentrated (0.316 or 1 M) solutions.

Pore Fluid Conductivity

After the pore size was determined, the measurement of the pore fluid conductivity was straightforward. With both half cells having the same electrolyte concentration and the same pressure, the membrane resistance R_m was determined. The pore fluid conductivity was calculated from

$$\kappa = \frac{K_c}{R_m} \tag{6-4}$$

As with any membrane resistance measurement, several current values were used to ensure that the pore fluid conductivity measurement was independent of the current used. The uncertainty in the pore fluid conductivity was always below 1.5%.

Streaming Potential Experiments

The streaming potential was determined by applying a pressure to one of the half cells while the other half cell was open to the atmosphere. Pressure was applied through the stock solution, and was measured with both a mercury-air manometer and a pressure transducer. No noticeable differences were observed between the pressure measurements of the two devices. The potential produced across the membrane by this pressure difference was measured with an electrometer (Keithley Model 642). The sign of the measured potential represents the sign of the membrane pore wall charge as long as the pressure is applied to the half cell connected to the positive terminal of the electrometer. This measurement consistently gave us a negative sign for the mica pore wall charge. The same pressure was applied to each side of the membrane, thereby eliminating the effects of the biases due to the Ag/AgCl electrodes. Three different pressures were applied to each half cell, and a least squares fit to the ΔP versus ΔV_s data was used to calculate the best slope for the six experimental points. Values of $\Delta V_s/\Delta P$ always had standard deviations of less than 3%.

Streaming Current Experiments

The same procedure used for the streaming potential experiments was used for the streaming current experiments as well, except that a current was measured instead of a potential. However, the streaming current was the most difficult experiment performed. The currents measured were very small, of order 10^{-10} A, which made measurements susceptible to outside interference, such as movement of the magnetic stir bars. Stirring was found to complicate the measurement by inducing a periodic current due to the magnet movement. Hence, during streaming current experiments, stirring was not used. This procedure probably had little if any effect on measurements because the porosity of mica membranes is extremely low; others who worked with these membranes (2) have found that boundary layer polarization effects are insignificant. It should also be mentioned that the electrometer used for the streaming current measurements (Keithley Model 642) had an error of 1% plus 3×10^{-14} A for currents in the range 10^{-10} A; therefore the uncertainty in measurements because of the presence of the electrometer in the circuit was negligible.[1] The standard deviation of the streaming current measurements was of order 2-5%.

Exclusion-Diffusion Potential Experiments

During exclusion-diffusion potential experiments a potential was measured with $C_{II}/C_I = 10^{1/2}$, and with no current or pressure across the membrane. The Ag/AgCl electrodes biases, as well as the Nernstian potential developed due to the fact that the electrodes were in different solutions, were substracted from the measurement. Each exclusion-diffusion potential was measured four times. The first measurement was taken immediately after the concentrations in the two half cells had been established, and the second about half an hour later to confirm that the measurement was not changing with time. Then a second set of measurements was taken with the solutions in each half cell reversed. The standard deviation of these experiments was less than 2%.

Sequence of Experiments to Test the Model

Others (45) have found the etching rate of the mica membranes in 10 wt.% hydrofluoric acid at 30 °C to be about 2.2 nm/min. We used this number only as a guide for estimating the pore size of our membranes at the same conditions. After the membrane was etched to approximately the desired pore size, it was placed in the cell and was exposed to a 1 M aqueous solution of LiCl to determine the actual pore size using the membrane resistance method (see equations (6-3a) and (6-3b)). The pore size was measured in aqueous solutions because, when we tried to measure the pore size using 1 M LiCl in methanol, the pore wall charge was irreversibly reduced to zero. Immediately after the pore size determination, 10^{-4} M aqueous LiCl solution was placed inside the cell until the membrane had stabilized, that is, until the membrane resistance and the streaming potential had reached constant values. This stabilization generally required about 48 hours. If we tried to replace the 10^{-4} M aqueous LiCl solution with the 10^{-4} M LiCl solution in methanol, cloudiness appeared initially, and then disappeared as more methanol solution was introduced into the cell. To avoid this problem, pure water was introduced into the cell, then pure methanol, followed by a 10^{-4} M solution of LiCl in methanol. The experiments started after the membrane had stabilized in 10^{-4} M LiCl in methanol (48 hours). All solutions were kept at pH around 9 by adding KOH.

---

[1] Based on communications with technical representatives at Keithley, Inc.

The next section describes preliminary experiments to examine the electrokinetic behavior of mica membranes in contact with LiCl solutions in methanol-water mixtures, while the actual test of the model in nonaqueous solvents is presented in the next Chapter.

6.4 Results of Preliminary Nonaqueous Electrokinetic Experiments

We present here the results of preliminary experiments to examine the space-charge model of electrokinetics in charged capillaries with nonaqueous solutions of lithium chloride. This is the first report that we are aware of in which electrokinetic experiments have been done using nonaqueous solutions having Debye lengths of the same order of magnitude as the radius of pores. One goal of our work was to investigate how changing the solvent properties (e.g., the dielectric constant) affects the ability of the model to describe the physical phenomena that take place inside charged pores. Methanol-water mixtures were chosen as the solvent because of the ease with which a continuous range of solvent dielectric constants could be obtained. In these preliminary experiments, solutions were made with low conductivity water ($< 10^{-6}$ S/cm) and reagent grade methanol (Baker®). The electrolyte used was reagent grade LiCl (Baker®), chosen because of its relatively high solubility in methanol.

The characteristics of the charge on the mica pore wall in aqueous solutions are discussed in detail elsewhere (2). For aqueous electrolyte solutions in contact with the mica pore surface, there is a region of constant wall charge when the pH of the bulk solution is in the range 7-10. In the nonaqueous experiments discussed here the measured pH was kept in this range by adding KOH in negligible amounts in comparison with the LiCl concentration. The hydrogen ion activity referred to the standard state in the mixed solvent (a_H) is related to the experimentally measured pH by $pa_H = pH - d_H$ where $d_H < 0.51$ for all methanol-water mixtures used and $d_H = -2.34$ for pure methanol (48);

hence, pa_H was close to the measured pH except in pure methanol. For these preliminary experiments, we assumed that in mixed solvents and methanol the dependence of the wall charge behavior on the H^+ activity does not differ significantly from its dependence in pure water. The dependence of pore charge on pH is discussed further in Chapter 7.

Pore Fluid Conductivity

An example of the experimental results for the pore fluid conductivity are plotted in Figure 6-3 versus the ratio of the pore radius to the Debye length for a membrane exposed to LiCl in 73 wt.% methanol in water. The horizontal coordinate corresponds to the square root of the electrolyte concentrations (see equation (2-1c)). The pore size of this membrane was a = 8.53 nm. The solid curves were computed from the space-charge model and each curve corresponds to a constant dimensionless pore wall charge S_w, known to be negative from aqueous solution experiments with mica membranes. The bulk conductivity was independently determined (dashed line in Figure 6-3), and the enhancement of the pore conductivity due to the wall charge is quite large for low electrolyte concentrations. The trend of the pore fluid conductivity data in Figure 6-3 is consistent with the results of aqueous experiments.

That the model is inadequate for the data at high a/D in Figure 6-3, or at high electrolyte concentrations, was expected since the assumption of complete dissociation breaks down at high ionic concentrations. Because a solvent with a dielectric constant lower than that of water tends to enhance the formation of ion-pairs in solution, the

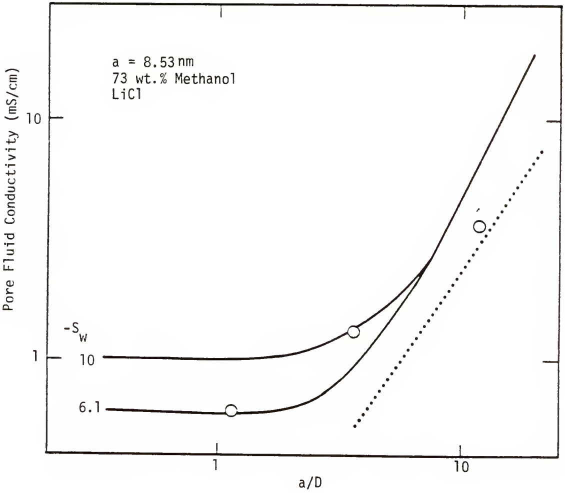

Figure 6-3 Pore fluid conductivity in 73 wt.% methanol-water mixtures. The theoretical predictions (———) were made from the space-charge model and the bulk fluid conductivity (.....) was independently measured.

concentration of the free current carriers (ions) is lowered substantially below the nominal concentration. For a symmetric electrolyte like LiCl, ion-pairs would have a dipole moment but no net charge, and as a rough first approximation, they should make no contribution to the electrical conductivity of the pore fluid. According to the Bjerrum theory (49) we can calculate the association constant (K_A) of ions in solution (cgs units)

$$K_A = \int_{r_o}^{d_B} 4\pi N_A r^2 \exp\left[\frac{|z_+ z_-| e^2}{r \varepsilon kT}\right] dr \qquad (6\text{-}5a)$$

$$d_B = \frac{|z_+ z_-| e^2}{2\varepsilon kT} \qquad (6\text{-}5b)$$

where N_A is Avogadro's number, and d_B is assumed to be the distance where the electrostatic energy of interaction of the two ions is twice their average kinetic energy. Note that d_B is inversely proportional to the dielectric constant. The distance r_o, the distance of closest approach of the ions, is often taken to be the sum of the crystallographic radii of the cation and the anion (r_o = 0.249 nm for LiCl). Assuming that the activity coefficients of the free ions and the ion-pairs are unity the law of mass action gives the fraction of dissociated ions γ

$$K_A = \frac{1 - \gamma}{\gamma^2 C_b} \qquad (6\text{-}6)$$

where C_b is the nominal concentration of the electrolyte. For LiCl in pure methanol, K_A is 52.5 dm^3/mol, and the dissociation constant begins to fall significantly below unity for concentrations above $C_b = 10^{-2}$ M. Others have noted that, while the Bjerrum theory is the best base case for evaluating the association constant, especially for large ions in neutral solvents, the Bjerrum theory may provide only a rough estimate of K_A (50). For the conductivity experiments reported here, we tried using the dissociated electrolyte concentration instead of C_b as an estimate of the free current carriers in solution. At low concentrations, this procedure has almost no effect. And as expected, at high concentrations this procedure does not affect the data enough so that they fall within the range of space-charge model predictions.

Figure 6-4 shows theoretical and experimental results for the change of the pore fluid conductivity versus the square root of the dielectric constant. The data are for a nominal electrolyte concentration of 10^{-3} M. To eliminate the effects of slight differences in the actual concentrations, each theoretical curve was calculated for a/D values of the actual experimental points, with the dimensionless pore wall charge density (S_w) kept constant. The theoretical curves in Figure 6-4 show a dramatic change of the pore fluid conductivity with the addition of methanol to water. The viscosities of methanol-water mixtures tend to be higher than the viscosities of the pure solvents (51), and it is shown elsewhere (15) that the mobilities of both ions are higher in pure water and pure methanol than in mixtures of water and methanol. Hence, the model predicts higher pore conductivities in the pure solvents than in the mixed solvents.

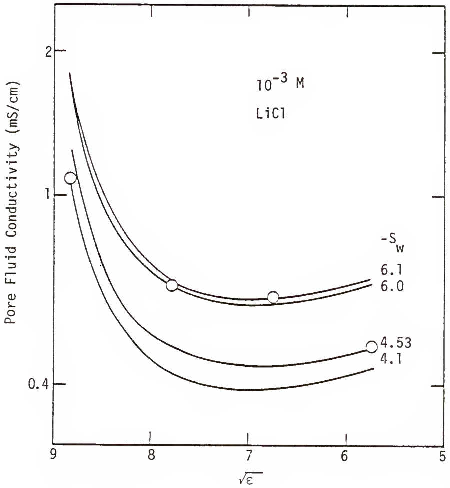

Figure 6-4 Pore fluid conductivity versus the square root of the dielectric constant of the solvent ($\sqrt{\varepsilon}$). The S_W values are scaled with respect to a/D values of the actual experimental data in order to eliminate the effect of differences in actual concentrations.

Unfortunately, there is no way to directly determine the electrostatic condition of mica membrane pore walls with titration. This limitation arises because mica membranes can be etched only up to porosities of about 1% before they begin to fall apart. At such low porosities the effects of Cl^- on the cleavage plane of mica (the front and back faces of a membrane) would still obscure the effects of Cl^- on the pore walls, and the use of titration to deduce the membrane pore wall charge would be futile. However, the pore wall charge density can be estimated from Figure 6-4 and equation (2-7b). Using pore conductivity data to evaluate the charge density is justified because the error in measuring the pore fluid conductivity was quite small. Values of the wall charge density deduced from conductivity data are plotted in Figure 6-5 versus the square root of the bulk dielectric constant. There is a strong dependence of the wall charge density on the bulk dielectric constant for both concentrations examined. As a general trend, it appears that the lower the dielectric constant the lower the absolute value of the wall charge density, which apparently means the lower the tendency of SiOH and/or AlOH groups on the mica wall to dissociate. Also, Cl^- ions appear to adsorb more onto the pore wall at the higher Cl^- concentration (10^{-2} M). It can be noted from Figure 6-5 that, for these preliminary experiments in pure methanol the wall charge density appears to be unaffected by the Cl^- concentration, suggesting that anion adsorption may be negligible and in fact may be inhibited by solvent (methanol) adsorption.

In past experiments with water as solvent (2) the Cl^- ion appeared to affect the mica pore wall charge. Hence, these results for pure

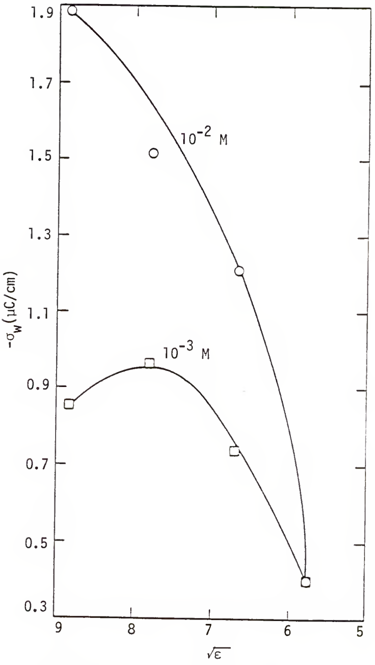

Figure 6-5 Wall charge density (σ_w) versus the square root of the dielectric constant of the solvent ($\sqrt{\varepsilon}$). Each curve represents a different nominal electrolyte concentration.

methanol appeared to be useful because they suggested that electrokinetic experiments in pure methanol could be done over several orders of magnitude in electrolyte concentration without having to be concerned about the effects of Cl^- on the pore wall charge density. However, it should be noted that the validity of the electrokinetic theory used here does not rest on the pore wall charge being constant irrespective of Cl^- concentration. Performing independent electrokinetic experiments (e.g., pore conductivity, exclusion-diffusion potential, streaming potential, and streaming current) and deducing the pore wall charge from each experiment, as done in experiments reported in Chapter 7, provides a rigorous, unambiguous test of the theory. Furthermore, these electrokinetic methods provide useful information about the ion-exchange properties of mica in contact with nonaqueous solutions.

Conclusions

This work represents the first time that we are aware of that nonaqueous electrokinetic experiments in a well characterized microporous medium have been reported for pore radii less than or equal to the Debye length. In addition, the results of this work showed some interesting trends. The data follow the trend of the space-charge model predictions for the pore conductivity. For high electrolyte concentrations the model fails, probably because the assumption that ion-ion interactions are negligible no longer holds. Our efforts to use the Bjerrum theory to account for ionic association were unsuccessful, pointing out the need to use more reliable methods for predicting ion-

ion interactions in nonaqueous solvents at high electrolyte concentrations.

In these preliminary experiments, the mica wall charge density appears to depend not only on the methanol concentration (Figure 6-5) but also on the coion (Cl^-) concentration. Figure 6-5 appears to indicate that, at low Cl^- concentrations, Cl^- adsorption may not occur to any significant extent in pure methanol. This result was quite encouraging since it would have allowed experiments to evaluate the space-charge model to be simplified. If the pore wall charge in pure methanol were constant irrespective of coion concentration, the number of experiments needed to verify the space-charge model in a nonaqueous solvent would be reduced considerably.

CHAPTER 7
EXPERIMENTAL INVESTIGATION OF THE SPACE-CHARGE MODEL IN NONAQUEOUS SOLVENTS

7.1 Introduction

This Chapter presents our experimental efforts to test the ability of the space-charge model to describe electrokinetic transport through charged porous media in nonaqueous solvents. The work in this Chapter goes beyond the preliminary experiments in Chapter 6. Here we fit the results of one electrokinetic experiment to the model in order to find the wall charge density (S_w), the only unknown parameter in the model. This S_w value is then used in the model to predict the other electrokinetic measurements performed. Comparison of model predictions with experimental data shows that the model is capable of describing electrokinetic transport through charged porous media in nonaqueous solvents for low electrolyte concentrations.

In aqueous solutions, the surface charge characteristics of the mica pore wall have been examined by others (2,3,45). After exposure to an aqueous electrolyte solution, the mica wall charge takes about 48 hours to stabilize to a constant value which is negative when the wall is in contact with 1:1 electrolytes. In addition, the charge remains essentially constant when the pH of the bulk electrolyte solution has a value of 7-10. The first section of this Chapter examines how these conclusions are affected by the use of methanol as solvent.

The second section of this Chapter describes our experimental efforts to verify the ability of the space-charge model to describe electrokinetic transport through charged porous media in nonaqueous solvents. Pure methanol was the solvent used, and LiCl was chosen as the electrolyte because of its high solubility in methanol. Four independent electrokinetic experiments (pore fluid conductivity, streaming potential, streaming current, and exclusion-diffusion potential) are described. The wall charge density deduced from pore fluid conductivity experiments is used to predict the results of the other experiments.

7.2 Mica Wall Characterization

The pore walls in track-etced mica membranes are perpendicular to the basal (cleavage) plane. To study the pore wall charge, we used streaming potential measurements on large pores (a = 145 nm) in contact with LiCl solutions for which the Debye length was relatively small (D << a). Under these circumstances, the wall charge density could be computed from the Helmholtz equation for the streaming potential, and the "flat-wall" relationship between the wall potential and charge (equations (5-1) and (5-2)). The wall charge characteristics of the mica were examined in three different solvents, water, 50 wt.% methanol-water mixtures, and pure methanol. The electrolyte used was 10^{-2} M LiCl, while the pH of the solution was controlled with the addition of KOH.[1] The LiCl (from Baker®) and KOH (from Mallinkrodt®) used for all work presented in this Chapter were reagent grade; the methanol was HPLC grade (Baker®) and the deionized water had a very low conductivity ($< 10^{-6}$ S/cm).

---

[1] Since it was desired to control the pH of solutions as much as possible, and since KOH takes up water from the atmosphere much more slowly than LiOH during the preparation of solutions, KOH was used instead of LiOH.

The purpose of the work presented was not to investigate the origin of the charge on the mica pore wall, or to develop a mechanism for the appearance of the surface charge. We are only interested in what experimental conditions give a membrane that exhibits a stable wall charge for the duration of our experiments. The sequence of the experiments done on the membrane used (membrane 17NOV4B) was as follows. The membrane was exposed to 10^{-2} M aqueous LiCl at a pH of about 9, and to study the time evolution of the mica wall charge, the streaming potential was measured till it reached a constant value. After the wall charge had stabilized, the effect of the pH on the wall charge was investigated. The pH of the bulk solution was then lowered until it reached a value of about 6, and then it was brought back up to about 9. We examined the pH dependence of the surface charge only for pH in the range 6-9 since this range covered the pH values which we expected to use in experiments. Later, solutions of 50 wt.% methanol in water mixtures, as well as pure methanol were put in the cell, and the same sequence of experiments was repeated.

Before presenting the experimental results, the meaning of the pH needs clarification. The term pH represents the experimentally found pH obtained from a pH meter standardized with aqueous buffer solutions. This means that the pH value does not necessarily represent the hydrogen ion activity referred to the standard state in the solvent used

(a_H). The relationship between a_H and the measured pH is given by (48)

$$pa_H = pH - d_H \tag{7-1}$$

In aqueous solutions, $d_H = 0$; in 50 wt.% methanol-water mixtures $d_H = 0.13$; and in pure methanol $d_H = -2.34$. It is only in pure methanol that the hydrogen ion activity defers much from the measured value. To avoid confusion that might be caused by using the a_H scale, and since one can always convert measured pH values to hydrogen ion activities, we present our results using the experimentally found pH.

Aqueous Experiments

The time evolution of the surface charge of the mica wall in 10^{-2} M aqueous LiCl solutions is shown in Figure 7-1. All the experiments in Figure 7-1 were done at pH values greater then 8.5. The wall charge, calculated from streaming potential measurements, was always negative, and for the first 30-48 hours after etching was continuously decreasing (in absolute value) until it reached a fairly stable value (about 0.5 $\mu C/cm^2$) which continued to slowly decrease with time over the next several days. Figure 7-2 presents the effect of pH on the mica wall charge (after the mica wall charge had stabilized). As Figure 7-2 shows the wall charge remains essentially the same for pH values in the range 7-10. Westermann-Clark (45) in similar experiments noted the same behavior of the mica wall charge.

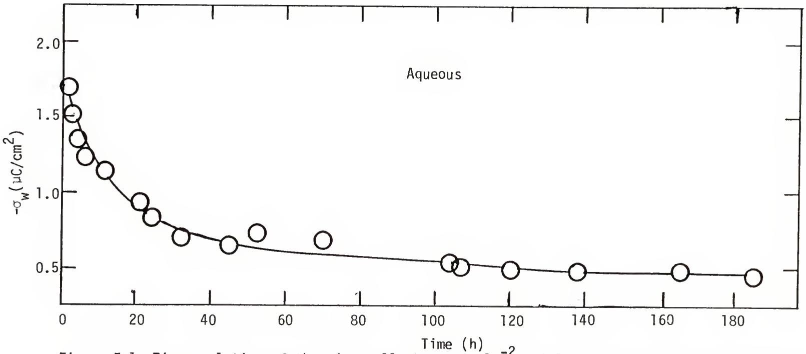

Figure 7-1 Time evolution of the mica wall charge in 10^{-2}M LiCl aqueous solutions at pH greater than 8.5. The pore size a = 145.0 nm. The solid line connects the experimental points.

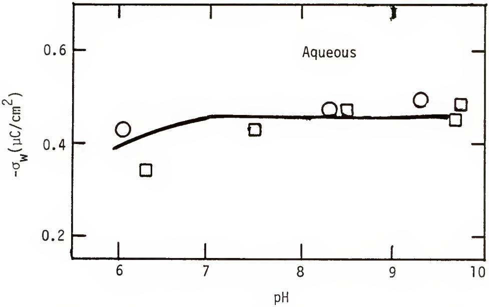

Figure 7-2 Surface charge density versus pH in 10^{-2} M LiCl aqueous solutions. The pore size was a = 145.0 nm. Circles: experiments while lowering the pH. Squares: experiments while increasing the pH. The solid line merely connects the experimental points.

Methanol-Water Mixture Experiments

After the aqueous experiments were finished, 10^{-2} M LiCl solutions in 50 wt.% methanol-water mixtures at pH greater than 8 were introduced into the cell. Figure 7-3 shows that the wall charge immediately reached a new value (about 0.35 $\mu C/cm^2$) which remained nearly constant for the duration of experiments in this solvent. The wall charge in methanol-water mixtures was lower in absolute value than the wall charge achieved in aqueous experiments. Figure 7-4 presents the pH dependence of the surface charge in methanol-water mixtures. As Figure 7-4 shows, the wall charge remains nearly constant for pH values greater than 7. Hence, using solutions having a pH in the range 7-10 assured that the mica wall charge density would remain nearly constant in 50 wt.% methanol-water mixtures.

Methanol Experiments

A 10^{-2} M LiCl in methanol solution at a measured pH greater than 8 was introduced into the cell after the experiments in methanol-water mixtures were completed. The time evolution of the mica wall charge in methanol is shown in Figure 7-5. As Figure 7-5 shows, there is an initial drop of the absolute value of the wall charge (from about 0.35 to 0.15 $\mu C/cm^2$), after which the charge remained fairly stable. Figure 7-6 shows that, as in the other solvents, the charge density of the mica wall in methanol is fairly stable as long as the measured pH is in the range 7-10. Finally, Figure 7-7 presents the effect of changing the electrolyte concentration on the mica wall charge in methanol solutions of LiCl at a pH greater than 8. As can be seen from Figure 7-7,

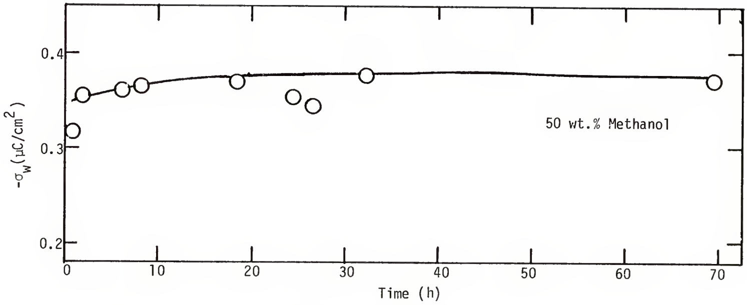

Figure 7-3 Time evolution of the mica wall charge in 10^{-2}M LiCl in 50 wt.% methanol-water solutions at pH greater than 8.0. The pore size a = 145 nm. The solid line connects the experimental points.

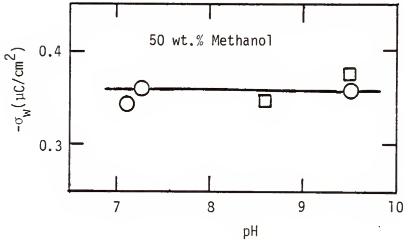

Figure 7-4 Surface charge versus pH in 10^{-2} M LiCl in 50 wt.% methanol-water solutions. The pore size a = 145 nm. Circles: experiments while lowering the pH. Squares: experiments while increasing the pH. The solid lines connect the experimental points.

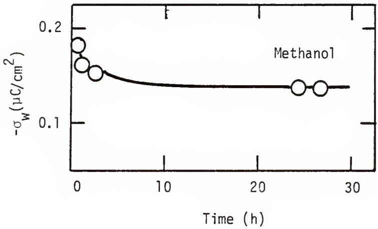

Figure 7-5 Time evolution of the mica wall charge in 10^{-2}M LiCl methanol solutions at pH greater than 8.0. The pore site a = 145 nm.

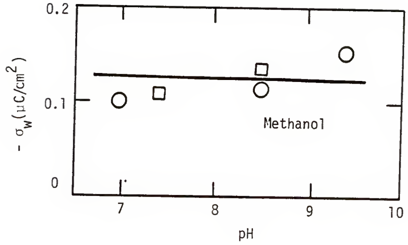

Figure 7-6 Surface charge density versus pH in 10^{-2}M LiCl in methanol solutions. The pore size a = 145 nm. Circles: experiments while lowering the pH. Squares: experiments while increasing the pH. The solid line represents an attempt to connect the experimental points.

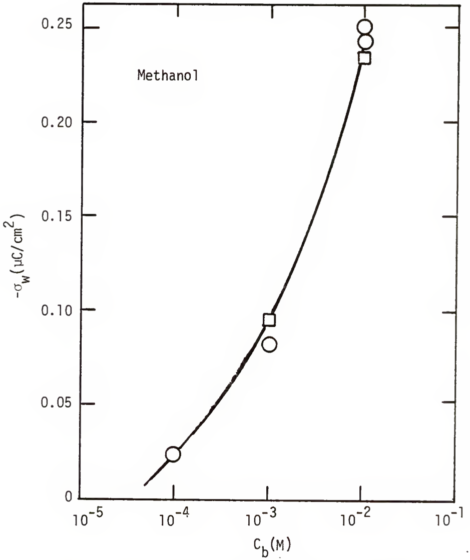

Figure 7-7 Surface charge density versus bulk LiCl concentration (C_b) in methanol. The pore size was a = 145 nm, and the pH was greater than 8.0. Circles: experiments while lowering C_b. Squares: experiments while increasing C_b. The solid line connects the experimental points.

the absolute value of the wall charge density decreases with electrolyte concentration, which suggests that the lower the electrolyte concentration, the lower the tendency of the Cl^- ions to adsorb on the mica pore wall.

Summarizing the results of our experiments to characterize the mica pore wall charge, we can say that the mica wall charge requires about 48 hours after the wall is exposed to an electrolyte solution to reach a constant value. This value shows a slight but definite tendency to decrease with time. In all solvents examined the wall charge density remains fairly constant as long as the experimentally measured pH value is in the range 7-10. Lowering the dielectric constant of the solvent (or equivalently, increasing the methanol content of the solvent) lowers the absolute value of the wall charge. Unfortunately, our speculation based on the preliminary experiments in Chapter 6, that the wall charge in pure methanol seems to be unaffected by the Cl^- ion concentration, was not confirmed here: as Figure 7-7 shows, the pore wall charge in methanol strongly depends on the bulk Cl^- ion concentration.

7.3 Nonaqueous Electrokinetic Experiments

This section presents our experimental efforts to examine the ability of the space-charge model to describe electrokinetic transport through charged porous media in nonaqueous solvents. Based on the characterization of the mica wall charge in the previous section, we were relatively confident that we could control the wall charge sufficiently to carry out this experimental examination of the model. All experiments were done with LiCl solutions in pure methanol at pH values greater than 8. It should be mentioned that the pH of the bulk solutions in the cell showed a tendency to decrease with time, suggesting an ion-exchange reaction of H^+ or OH^- ions with the glass cell walls or with the mica itself. To overcome this problem, fresh methanol solutions were put into the cell at least daily. The sequence of experiments immediately after etching to measure the pore size and to stabilize the membrane charge in 10^{-4} M LiCl in methanol have been described in section 6.3. The membrane used here (membrane 15JAN5B) had a pore size of 10.5 nm (± 2.4%). All the experiments presented below were done within a 24 hour period.

Bulk solutions were prepared in advance by successive dilutions of concentrated solutions with KOH in methanol added just before a solution was placed into the cell. Records of the solution volumes used were kept so that the amount of KOH in the final solution could be calculated. From the amount of KOH in the solution, the contribution to the conductivity by KOH was calculated using Onsager's relation (52)

$$\kappa_{KOH} = C_{KOH}(\Lambda_0 - SC_{KOH}^{1/2}) \tag{7-2}$$

where the infinite dilution conductance is $\Lambda_0 = 115.3$ cm^2/Ω mol calculated from the value of $\Lambda = 90$ in 10^{-2} M KOH in methanol[1] and from the value of S given in the literature (51,52). The contribution of LiCl to the bulk fluid conductivity was then calculated from the measured conductivity (LiCl plus KOH) with the conductivity of the KOH in the solution subtracted out. From the LiCl conductivity found in this way, the bulk LiCl concentration was calculated from Justice's adaptation of the method by Fuoss (50,52,53,54)

---

[1] With less accurate conductivity measurements than in the literature, we obtained $\Lambda_0 = 108$.

$$\kappa = C_b\left[\Lambda_0 - S(C_b\gamma)^{1/2} + EC_b\gamma\log(C_b\gamma) + JC_b\gamma - K_F f_{ij}^2\Lambda_0 C_b\gamma\right] \qquad (7\text{-}3)$$

where the values of the solvent dependent constants S, E, J are given in the literature (52), and f_{ij} is the electrolyte activity coefficient given by Fuoss. The association constant K_F was calculated by using d_B (the Bjerrum distance parameter) from equation (6-5b) in the Fuoss association constant (cgs units)

$$K_F = \frac{4\pi N_A}{3000} d_B^3 \exp \frac{|z_+z_-| e^2}{d_B \varepsilon kT} \qquad (7\text{-}4)$$

The fraction dissociated γ was calculated using K_F and equation (6-6).

Pore Fluid Conductivity

Experimental results for the pore fluid conductivity versus the ratio of the pore radius to the Debye length (a/D) are plotted in Figure 7-8 for LiCl solutions in methanol. Each solid curve was computed from the space-charge model (see Chapter 4) and corresponds to a constant value of the wall charge (S_w), known to be negative from streaming potential and streaming current experiments (see below). The reason for using the wall charge boundary condition (equation (2-7b)) instead of the constant wall potential condition is that the data in Figure 7-8 more closely resemble predictions using the wall charge condition (see, for example Figure 4-2). That is, the pore fluid

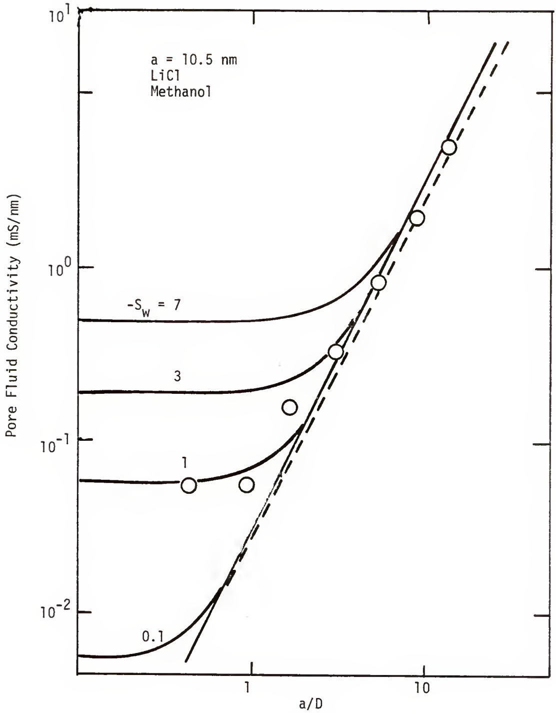

Figure 7-8 Pore fluid conductivity in LiCl methanol solutions. The theoretical predictions were made from the space-charge model (———) and the bulk fluid conductivity (-----) was measured during the experiments.

conductivity appears to approach a constant value at low a/D rather than continue to decrease as it would if the wall potential were constant. Aqueous experiments (45) have also shown that the mica wall charge more closely follows a constant wall charge condition than a constant wall potential condition, and the superficial features of the data in Figure 7-8 are similar to those in aqueous experiments.

The enhancement of the pore fluid conductivity due to the wall charge is quite large at low concentrations, and the pore conductivity approaches the bulk conductivity at high concentrations. The bulk solution conductivity, measured for each bulk solution prepared, is shown in Figure 7-8 (dashed line). Also plotted is the calculated bulk conductivity (solid line) assuming that the infinite dilution diffusivities[1] (D_+, D_-) apply over the entire range of electrolyte concentrations, even at high concentrations. This solid line represents the theoretically calculated bulk conductivity assuming complete ion dissociation, and at high electrolyte concentrations it coincides with model predictions, which also assumes complete dissociation. As can be seen in Figure 7-8 the calculated and experimental bulk conductivities do not coincide, as expected, since LiCl does not dissociate completely in methanol at high electrolyte concentrations. We did experiments in bulk concentrations up to $7\text{x}10^{-2}$ M, and our calculations using equation (7-3) showed that only 82% of the ions present dissociated at this highest concentration.

---

[1] The diffusivities $D_+ = 1.05\text{x}10^{-9}$ and $D_- = 1.40\text{x}10^{-9}$ m^2/s were found from infinite dilution ionic conductance data in Vidulich et al. (55).

Figure 7-9 shows the wall charge densities obtained by fitting the pore fluid conductivity experiments to the model. The wall charge densities were found from the S_w values through (equation (2-7b))

$$\sigma_w = \frac{\varepsilon kT}{ae} S_w \tag{7-5}$$

The wall charge remains essentially constant at very low electrolyte concentrations (below 3.16×10^{-4} M), but it increases with electrolyte concentration at higher concentrations. Unfortunately, at concentrations of 10^{-2} M and higher the pore fluid conductivity essentially equals the bulk solution conductivity, as Figure 7-8 shows. Hence, it was difficult for high concentrations to calculate a pore wall charge density. The values of the wall charge densities found in Figure 7-8 were used below to predict the other electrokinetic experiments. The use of conductivity data to determine S_w, the only adjustable parameter in the model, is justified because of the small error in measuring the pore fluid conductivity, and its sensitivity to the wall charge at low electrolyte concentrations (Chapter 4). Because the pore size had to be specified to deduce S_w from the pore conductivity as in Figure 7-9, the uncertainty in Figure 7-9 is at most 7% (see Appendix D for a discussion of uncertainties in the pore size determination). Nevertheless, the polarity of the wall charge still must be ascertained from the streaming potential.

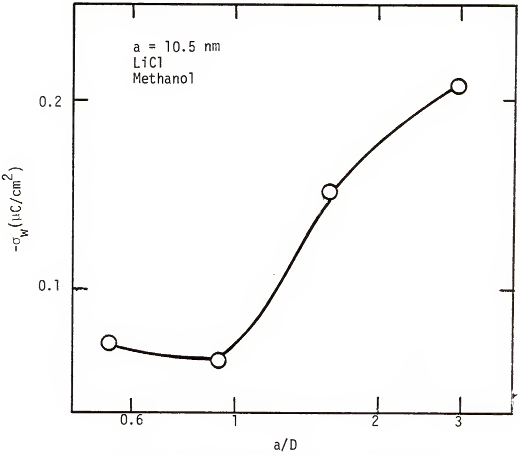

Figure 7-9 Surface charge densities determined by fitting the space-charge model to pore fluid conductivity data versus a/D. The solid line connects the experimental points.

Streaming Potential

The streaming potential data for LiCl in methanol are shown in Figure 7-10. The magnitude of the streaming potential is quite sensitive to S_w for the high electrolyte concentrations, somewhat less sensitive for low electrolyte concentrations, and completely insensitive at intermediate concentrations. The data show the same superficial trends as in aqueous solutions. It is interesting that the experimental point at a/D = 1.64 in Figure 7-10 represents a maximum value for the streaming potential at the corresponding wall charge density (Figure 5-4). This is the first time that we are aware of that this maximum has been observed experimentally, despite the categorical assertions by other experimental investigators that no such maximum exists (56).

Figure 7-11 compares the measured streaming potential with predictions from the space-charge model using wall charge densities from the pore fluid conductivity in Figure 7-9. Both the pore fluid conductivity and the streaming potential experiments can be measured with high accuracy, and they are much less susceptible to outside interference than the other electrokinetic experiments. Since there are no adjustable parameters in the comparison in Figure 7-11, the good agreement is solid evidence for the correctness of the theory. The uncertainty in S_w values used to obtain the solid curve in Figure 7-11 leads to a maximum uncertainty of about 7% for the solid curve, and with the maximum uncertainty in the streaming potential measurements of 3%, the combined uncertainties of theoretical predictions and experiments in Figure 7-11 give complete overlap of predictions and experiments.

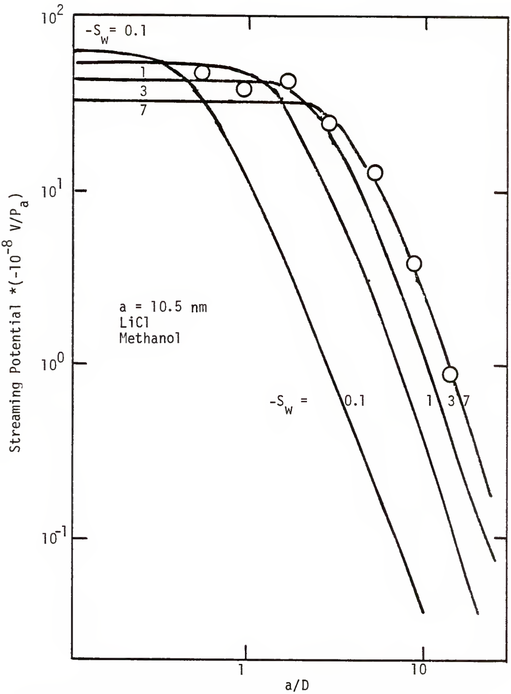

Figure 7-10 Streaming potential data in LiCl methanol solutions. The theoretical predictions were calculated from the space-charge model (———).

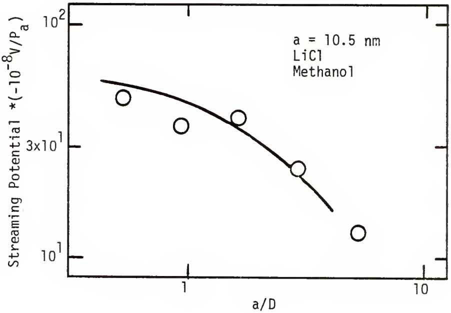

Figure 7-11 Theoretical predictions (———) versus experiments for the streaming potential with LiCl methanol solutions. The solid curve is predicted from the space-charge model using values of σ_w determined from Figure 7-9 for each a/D. The solid line connects the theoretical predictions.

Since the pore conductivity and the streaming potential are our most accurate electrokinetic measurements, the test of the model in Figure 7-11 is the best means available to us to verify the model at this point.

Streaming Current

The streaming current, measured by applying a pressure ΔP and measuring a current I_s across the membrane, has been less extensively studied than other electrokinetic phenomena. The streaming current data for LiCl in methanol are shown in Figure 7-12. Slight differences in concentrations that usually existed between the two half-cells gave rise to a current which was subtracted out from the data. It should be mentioned that streaming current experiments were difficult to perform and were very susceptible to outside interference, since the currents measured were of order 10^{-10} A. At high electrolyte concentrations it was especially difficult to measure the streaming current because of its small value. Others (56) have faced the same problems. Because the magnetic stirrers caused large current oscillations during streaming current experiments, we did not stir the solutions during the streaming current experiments. The possible concentration polarization fields induced as a result might account for the slight differences observed between theory and experiments (below).

Although the streaming current experiments were not as accurate as the pore conductivity or the streaming potential experiments, the streaming current is the only experiment done that unambiguously gives both the wall charge density and the valency of the wall charge. Each

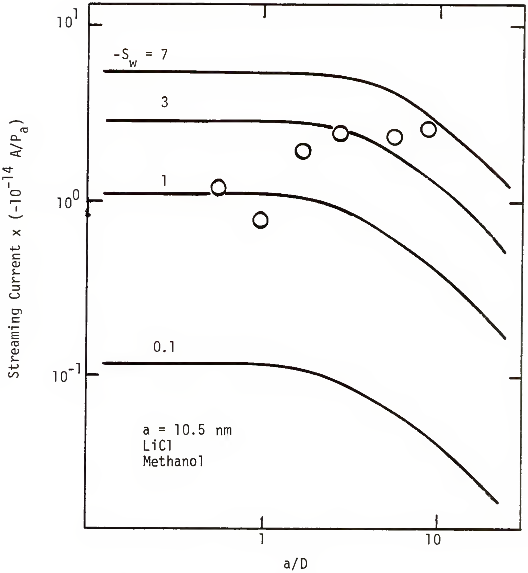

Figure 7-12 Streaming current in LiCl in methanol solutions. The theoretical predictions were calculated from the space-charge model (———).

solid line in Figure 7-12 represents the space-charge model predictions for a constant value of the dimensionless pore wall charge density S_w. The model predictions reach a constant value at low electrolyte concentrations, while they tend to zero at high electrolyte concentrations. The sign of the streaming current is the same as the sign of the pore wall charge, so unlike the pore fluid conductivity, the streaming current indicates the sign of the pore wall charge. Unlike streaming potential predictions (Figure 7-10), the streaming current predictions at constant S_w values do not intersect one another, and the model predictions do not show any maxima or minima.

The streaming current data in Figure 7-12 also do not show a maximum or minimum. This is in contrast to what Van der Put and Bijsterbosch (33) found for polystyrene membranes. Their work is the only extensive examination of the streaming current that has been published. While their model, like ours, does not predict any maximum or minimum for the streaming current, their streaming current experiments showed a definite maximum at intermediate concentrations. However, Van der Put (56) was forced to calculate some of his experimental "streaming currents" from the membrane resistance and the streaming potential. Table 7-1 compares streaming currents, calculated from our experimental membrane resistances and streaming potentials, with streaming currents measured directly, and as Table 7-1 shows, there is a maximum in the calculated streaming currents, but not in the directly measured streaming currents. At low a/D values, obtaining streaming current data from the membrane resistance and streaming potential appears to be useful means of checking streaming currents measured directly. However, at

Table 7-1
Comparison of Calculated and Measured Streaming Currents

a/D	Calculated Streaming Current (A/Pa)	Experimentally Measured Streaming Current (A/Pa)
0.5	-0.96×10^{-14}	-1.16×10^{-14}
0.9	-0.74×10^{-14}	-0.77×10^{-14}
1.6	-2.19×10^{-14}	-1.93×10^{-14}
2.9	-2.72×10^{-14}	-2.45×10^{-14}
5.2	-3.66×10^{-14}	-2.40×10^{-14}
8.9	-2.65×10^{-14}	-2.59×10^{-14}
13.7	-1.52×10^{-14}	-

high a/D this procedure loses validity, and the maximum in Van der Put's streaming current data is probably the result of using other data to obtain streaming currents.

Figure 7-13 compares the measured streaming currents with predictions from the space-charge model using charge densities from the pore conductivity experiments in Figure 7-9. The uncertainty in S_w values used to obtain the solid curve in Figure 7-13 leads to a maximum uncertainty of about 7% for the solid curve, and with the maximum uncertainty in the streaming current measurements of 5%, the combined uncertainties of theoretical predictions and experiments in Figure 7-13 give complete overlap of predictions and experiments. There are no adjustable parameters in this comparison, so the agreement between theory and experiments, given the difficulties encountered in streaming current measurements, is quite good. Along with the streaming potential results (Figure 7-11), these streaming current results point strongly to the correctness of the space-charge model.

Exclusion-Diffusion Potential

Results for the dimensionless exclusion-diffusion potential experiments using LiCl in methanol are in Figure 7-14. In Figure 7-14 the Debye length was calculated from the smaller of the two electrolyte concentrations in the cell with the concentration ratio for LiCl fixed at $C_{II}/C_I = 10^{1/2}$. The theoretically predicted diffusion limit at high concentrations (equation (3-10c)) is $\omega_{ed} = -0.141$. As can be seen from the data in Figure 7-14, the pore wall charge increases as electrolyte concentration increases. At the very lowest LiCl concentrations (10^{-4}

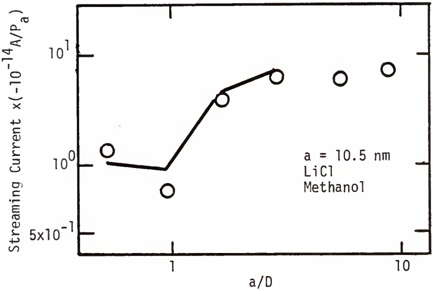

Figure 7-13 Theoretical predictions (———) versus experiments for the streaming current with LiCl in methanol solutions. The solid curve is predicted from the space-charge model using values of σ_w determined from Figure 7-9 for each a/D. The solid line connects the theoretical predictions.

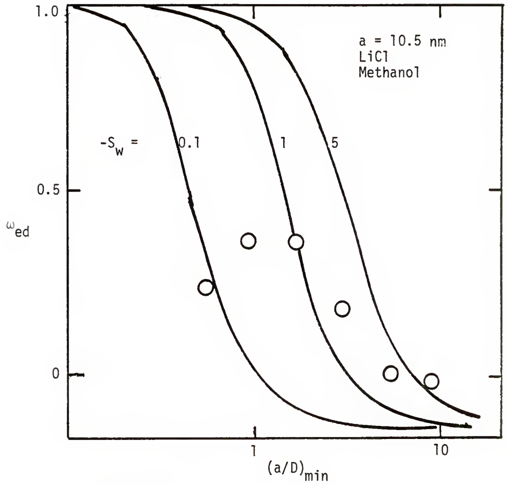

Figure 7-14 ω_{ed} in LiCl methanol solutions. The theoretical predictions were calculated from the space-charge model (———).

to 10^{-3} M), the presence of the pH-controlling electrolyte (10^{-4} M) KOH appears to complicate the measurement of ω_{ed}. With KOH added, the ratio C_{II}/C_I, based on the total electrolyte concentration, is no longer $10^{1/2}$ when C_I or C_{II} is of order 10^{-3} or smaller. Hence, the exclusion potential limit (equation (3-10b)) based on $C_{II}/C_I = 10^{1/2}$ is no longer valid, and the data do not follow the S-shaped form of the theoretical curves at low a/D. In future work, the exclusion-diffusion potential theory needs to be extended to the case where more than a single electrolyte is present.

Using the exclusion-diffusion potential results, the space-charge model is tested again by using Figure 7-9 to obtain the wall charge density for the given membrane and solution conditions. The numerical integrations from C_I to C_{II}, or $(a/D)_{min}$ to $(a/D)_{max}$, required for calculations (equation (2-13)), were done with interpolated values of σ_w from Figure 7-9. Comparison of the model predictions and the exclusion-diffusion data is in Figure 7-15, where it can be seen that at low electrolyte concentrations, where the pH-controlling electrolyte KOH constituted a significant fraction of the total electrolyte present, the agreement between the model and experiments is poor. The direction of the disagreement, that is, lower ω_{ed} values than predicted assuming $C_{II}/C_I = 10^{1/2}$, was expected. At high electrolyte concentrations, where the amount of KOH present was small in comparison to the total electrolyte concentration, the data and predictions appear to approach one another more closely. Before the data in Figure 7-15 can be used to confirm or invalidate the model, the space-charge model needs to be extended to the case of more than one electrolyte in solu-

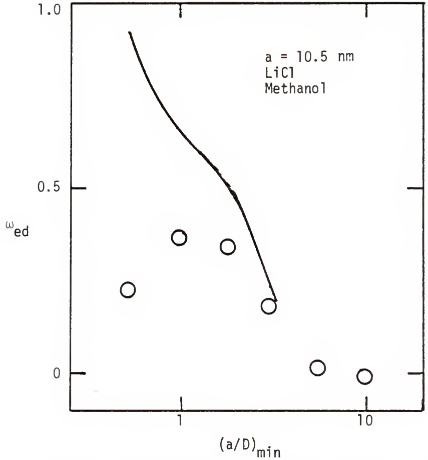

Figure 7-15 Theoretical predictions (-) versus experiments for ω_{ed} with LiCl methanol solutions. The solid curve is predicted from the space-charge model using values of σ_w determined from Figure 7-9 for each a/D. The solid line connects the theoretical predictions.

tion. Note that the other electrokinetic experiments performed (pore fluid conductivity, streaming potential, and streaming current) are much less dependent on the presence of a pH-controlling electrolyte at low electrolyte concentrations since the total electrolyte concentration present directly affects ΔV_{ed}, whereas its effect on κ, ΔV_s, or I_s is only indirect. For example, for the lowest concentrations used in Figure 7-14 ($3.2\text{x}10^{-4}/10^{-4}$ M LiCl), the addition of KOH (10^{-4} M) to both sides of the cell gives a total electrolyte concentration ratio of 2.1 instead of 3.2, and a Nernstian (low a/D) potential limit of 19 mV instead of 30 mV, or a limiting value of ω_{ed} in Figure 7-14 which is 0.6 instead of 1.0. This may be contrasted with the effect of the added KOH at the lowest concentrations in the other electrokinetic experiments. That is, the added KOH affects the other measurements only insofar as it affects the product of the mobilities and the intrapore concentrations of the counterions (Li^+ and K^+), whose mobilities are not different enough to make large differences in the measured quantities.

7.4 Conclusions

For the work presented in this Chapter, several useful conclusions can be drawn. When the pore surface charge density is deduced from one experiment, as was done here using the pore fluid conductivity, and when this surface charge is used to predict the results of other, independent electrokinetic experiments, such as the streaming potential and the streaming current, the resulting predictions compare quite well with the experimental measurements. This comparison of experiments and theory, with no adjustable parameters, lends strong support to the correctness of the space-charge model when used for dilute electrolytes in nonaqueous solvents. This support for the space-charge model in nonaqueous media agrees with what has been observed for aqueous solutions (2). Alternative procedures for carrying out the theoretical and experimental comparisons could have been used, such as deducing the membrane pore wall charge from the streaming potential, and predicting the results of the other electrokinetic experiments. However, because the pore conductivity measurements had the smallest errors, they were used to deduce the pore wall charge density. The procedure used to examine the model experimentally breaks down for the exclusion-diffusion potential. However, as noted already, the exclusion-diffusion potential is especially susceptible to the total electrolyte concentration, and at low concentrations the pH-determining electrolyte (KOH) complicated matters tremendously. What is needed is an extension of the space-charge model to situations in which more than one electrolyte is present.

CHAPTER 8
SUMMARY AND RECOMMENDATIONS

The first five Chapters of the work presented examine theoretical predictions from the space-charge model for electrokinetic transport through charged porous media separating dilute electrolyte solutions. The model uses the Navier-Stokes and Nernst-Planck equations to predict transport caused by electrolyte concentration, pressure, and electrical potential differences across a charged porous medium. The model also uses the Poisson-Boltzmann equation to account for the radial variation of ionic concentrations inside a charged pore. While the use of the Poisson-Boltzmann equation is the major advantage of the space-charge model over other electrokinetic models, the use of the Poisson-Boltzmann equation nevertheless complicates the numerical computations to evaluate the fluxes through a porous medium. To overcome this problem, approximate analytical solutions to the Poisson-Boltzmann equation were developed and compared to numerical results. The ranges of applicability of the low and high potential approximating solutions have been delineated, and we have extended the use of approximating solutions for the case in which the pore wall charge is specified. Using the pore wall charge, instead of the pore wall potential, is generally more realistic in electrokinetic calculations, since the pore wall electrostatic condition usually arises from a dissociation and/or adsorption equilibrium with the surrounding electrolyte solution.

Thus, the pore wall potential is a derived condition, and it is less directly related to other measured quantities (by titration, for example) than the wall charge density. For experimentalists, our description of the high and low approximating solutions, with the pore wall charge specified, should be very useful when applied under the proper circumstances. Furthermore, the approximating solutions offer the best first estimate of the pore wall potential for much more precise calculations using a Runge-Kutta method to calculate the radial variation of the electrical potential in the pore fluid.

Three electrokinetic effects were examined in detail from a theoretical perspective: the exclusion-diffusion potential, the pore fluid conductivity, and the streaming potential. The exclusion-diffusion potential develops across a charged porous medium separating two solutions having different electrolyte concentrations. The space-charge model predictions for the exclusion-diffusion potential were compared to the predictions of the Meyer-Sievers model for a wide range of wall charge densities and electrolyte concentrations. The two models give similar results for the whole range of electrolyte concentrations at low wall charge densities, but the Meyer-Sievers approach deviates from the space-charge model predictions at higher wall charge densities. Possible reasons for these deviations, examined in detail in Chapter 3, include the pore geometry, convective flow inside the pore, and the different ionic distribution profiles that the two models calculate inside the pore. The Meyer-Sievers model fails to account for the pore geometry and the convective flow inside the charged pores, but these two inadequacies of the TMS theory were shown not to have any significant effect on the space-charge model predictions either. However, the failure of the Meyer-Sievers model to adequately account for the ion-pore wall electrostatic interactions, and therefore the radial variation of ionic concentrations inside the pore, was shown to result in erroneous predictions for the ionic transport numbers inside the pore. This failure of the Meyer-Sievers causes it to incorrectly predict the exclusion-diffusion potential at high values of the pore wall charge density.

The enhancement of the conductivity of the fluid in the pores of a charged membrane separating two electrolyte solutions at the same concentration and pressure occurs because the pore wall charge is neutralized in the diffuse layer of the pore fluid, even at very low electrolyte concentrations. Space-charge model predictions for the pore fluid conductivity were compared when two different boundary conditions, the constant pore wall charge or the constant wall potential boundary condition, were applied to the model. To our knowledge, this is the first time that the effect of the pore wall boundary condition on the predictions of an electrokinetic effect has been examined in detail. Since pore wall charge densities and wall potentials can always be mutually converted using diffuse double layer theory, neither approach implies any mathematical limitations. However, the two approaches imply very different electrostatic responses of pore walls to their surroundings, and the two approaches have very different effects on the space-charge model predictions of the pore fluid conductivity, especially at low electrolyte concentrations. For low electrolyte concentrations, the use of the constant wall charge boundary condition in the space-charge model was shown to predict a limiting value for the pore fluid conductivity, while the use of the constant wall potential condition does not. At high electrolyte concentrations, both approaches predict pore fluid conductivities equal to the bulk fluid conductivities. While using the wall potential as a boundary condition is somewhat easier mathematically than using the wall charge, one must recognize that the available experimental data more closely resemble calculations using a constant wall charge than those using a constant wall potential.

Space-charge model predictions for the pore fluid conductivity, when the potential distribution inside the pore is found by numerical solution of the Poisson-Boltzmann equation, were compared to predictions when the potential profiles were obtained from the high and low potential approximating solutions. Predictions for the pore fluid conductivity using the high potential approximation were shown to be adequate only at low electrolyte concentrations, while the low potential approximation was shown to be adequate only for high electrolyte concentrations. When care is taken not to use the approximate solutions when they are not applicable, combining the high and low potential approximations can be a powerful and simple method for estimating the pore fluid conductivity for a wide range of concentrations and pore wall charge densities.

The predictions of the space-charge model for the pore fluid conductivity were also compared to the predictions of other electrokinetic models in the literature. It was shown that Schmid's model, despite its simplistic approach to the calculation of the fluid flow inside the pore, can be used to predict the pore fluid conductivity for the whole range of electrolyte concentrations examined and for small values of the pore wall charge ($|S_w| < 10$). Nevertheless, while Schmid's model is easy to use for routine calculations within the range of its applicability, it was shown to be more complicated to use than the approximate solutions to the space-charge model presented here. Bikerman's approach, because of its severe assumptions, was shown to be restricted to large electrolyte concentrations and small pore wall potential values.

The streaming potential develops across a charged porous medium when the two electrolyte solutions adjacent to it are at different hydrostatic pressures. The space-charge model predictions for the streaming potential were compared to the streaming potential predicted using the approximating solutions developed here, and to the well known Helmholtz equation. Because of the enhancement of the pore fluid conductivity at low electrolyte concentrations, the streaming potential was shown to exhibit a maximum as pore wall charge was varied, all other variables held constant. This is the first time that such a maximum in the streaming potential has been shown to exist, and its existence should have important implications for experimentalists. On the other hand, the Helmholtz equation predicts the streaming potential to be a monotonically increasing function of the absolute value of S_w, and hence does not display a maximum. It was shown that using the Helmholtz equation could yield quantitatively incorrect estimates of the pore surface charge, and could incorrectly indicate a pore wall charging or discharging mechanism. The Helmholtz equation was shown to be incorrect when the ratio of the pore radius to the Debye length is of order 10 or less. When the Helmholtz expression is invalid, the low and high potential approximations Y_{LP} and Y_{HP}, developed here for the constant wall charge condition and discussed in Chapter 5, are shown to apply with little error over a wide range of conditions.

Our experimental investigation of the space-charge model for electrokinetic effects, using a nonaqueous solvent in charged porous membranes, is the first such investigation ever conducted. We showed that the mica pore wall charge could easily be characterized in nonaqueous media with the methods used here. The time studies of the pore wall charge, using the streaming potential to obtain the charge density, showed that, as in aqueous solvents (2), the pore wall charge takes 24 to 48 hours to achieve a relatively stable value in nonaqueous solvents. The pH studies of the pore wall charge showed that the charge is nearly constant in pure water, methanol-water mixtures, and methanol when the measured pH is in the range 7-10. This allowed a fairly stable pore wall charge to be produced and controlled in mica membranes after 48 hours in solutions with pH greater than 7. Our studies of the pore wall charge versus LiCl concentration in methanol, while indicating no dependence on LiCl concentration in preliminary experiments, later showed that LiCl concentration can alter the pore wall charge, probably as a result of Cl^- adsorption onto the pore wall. While this creates a complication in examinations of the validity of the space-charge model in nonaqueous media, this complication was not insurmountable.

With our studies of the time, pH, and electrolyte concentration dependence of the mica pore wall charge completed, we were ready to examine the validity of the space-charge model in a nonaqueous solvent (methanol). Values of the wall charge deduced from the pore fluid conductivity experiments were used along with the model to predict the other electrokinetic results. The wall charge densities deduced from from the pore fluid conductivity experiments depended on the bulk electrolyte concentration, that is, the higher the bulk electrolyte concentration, the higher the absolute value of the pore wall charge density, which suggests the higher the tendency of the Cl^- ions to adsorb on the mica pore wall. Although this variation of the pore wall charge complicated the experimental examination of the model, and although it would have been convenient if the pore wall charge were not affected by electrolyte concentrations, it in no way deterred us from testing the theoretical model with other experiments.

The streaming potential experiments showed that the mica wall in contact with methanol is negatively charged. Using pore wall charge densities from pore conductivity measurements, the streaming potential was predicted using the theoretical model, and compared with experiments (Figure 7-11). This comparison by itself gives strong support to the ability of the space-charge model to describe electrokinetic transport through charge porous media in nonaqueous solvents. However, since streaming potential experiments do not give an unambiguous value of the pore wall charge at intermediate electrolyte concentrations (Chapter 5), we decided to test the ability of the model to predict other electrokinetic parameters as well.

Streaming current experiments verified the negative sign of the charge on the mica pore wall obtained from streaming potential measurements. We were also able to show that the use of measured membrane resistances and streaming potentials to calculate streaming currents is an invalid procedure at high electrolyte concentrations. The ability of the theoretical model to predict experimental streaming currents was also examined. Pore wall charge densities from pore conductivity data were used to predict experimental streaming currents. Given the difficulties in obtaining streaming current measurements, the streaming current predictions compare very favorably with the experimental data (Figure 7-13). This test of the space-charge model with no adjustable parameters is another strong indication of the correctness of the theory.

Since the theoretical curves for the streaming current do not intersect, as in the streaming potential, and since they do not merge even at reasonably high a/D values, as does the pore fluid conductivity, the streaming current is a very useful experimental method for evaluating both the magnitude and the sign of pore surface charge densities. However, to use streaming currents to find values of the wall charge density which will be accurate enough to use in the model to predict the other electrokinetic experiments, the accuracy of experimental streaming current data needs improvement. At this point, pore fluid conductivity measurements and streaming potentials are considerably more accurate than streaming currents. The presence of electrical shielding around the electrokinetic cell and additional electronic circuitry to damp out current oscillations caused by the magnetic stirrer will probably solve some of the problems associated with the streaming current measurements. If the problems associated with the streaming current experiments are solved, we will have available to us an experimental method which would unambiguously indicate both the magnitude and the sign of the pore wall charge, something that we have had to rely on two different experiments to obtain until now. In addition, it is our intention to investigate the streaming current in more detail from a theoretical perspective in the near future.

The model predictions of the exclusion-diffusion potential data do not compare as favorably as do the streaming potential and the streaming current predictions and data, especially at low electrolyte concentrations. Our experiments have shown that a measured pH in the range 7-10 is required for a stable wall charge density. However, the amount of pH-determining electrolyte added can be a substantial fraction of the electrolyte present, especially at low concentrations, and its presence along with the high mobility of the OH^- ion can dramatically affect the electrical potential measured. Thus, the model needs to be extended to treat more than one electrolyte in solution in order to interpret the exclusion-diffusion potential results.

In summary, we have shown that the space-charge model is capable of describing electrokinetic transport in charged porous media in contact with dilute nonaqueous electrolyte solutions. The model performs well in predicting the results of independent electrokinetic experiments when the only unknown parameter (pore surface charge) is deduced from one experiment (pore fluid conductivity) and used to predict the results of other experiments (streaming potential and streaming current). This conclusion applies for LiCl concentrations in methanol up to 10^{-2} M and for pores with radii as small as 10.5 nm. Improve-ments need to be made in shielding the electrokinetic cell for streaming current experiments, and the theoretical model needs to be extended to more than one electrolyte in solution in order to be able to fully examine exclusion-diffusion potential results.

Other areas of future investigation include examining how electrolytes with coions other than Cl^- perform with respect to the model. While our experiments indicate that the Cl^- ion adsorbs on the mica pore wall, these ions are generally regarded as less likely to adsorb on surfaces than larger ions because of their small size and their high energy of solvation in polar solvents (57). Hence, the F^- ion would be a better choice than I^- or Br^- for future work in nonaqueous polar solvents. Another area of future research is testing the model with ions having different ionic valences, like $MgCl_2$. The first experiments with aqueous solutions of $MgCl_2$ (45) were not very successful; streaming potential experiments indicated that the Mg^{++} ions adsorbed strongly on the mica pore wall. Hence, other bivalent ions must be tried. Moreover, the electrokinetic behavior of charged porous media in contact with other solvent types must be pursued. Methanol and water are both hydrogen bonding solvents, and the electrokinetic behavior of other types of solvents (basic, neutral, and acidic (50)) needs to be investigated. Finally, the model should be extended to cover porous media with nonidentical pore sizes, but with a known pore size distribution. This situation is not difficult to model mathematically, and can be easily attained experimentally with track-etched mica membranes by sequential exposure of the membrane to the radiation source with new tracks and old pores etched to a desired new size during the time between exposures.

APPENDIX A
NUMERICAL SOLUTION OF THE POISSON-BOLTZMANN EQUATION

This Appendix presents the fourth order Runge-Kutta routine used to obtain the intrapore potential profile from the Poisson-Boltzmann equation in both the cylindrical pore and the infinite slit cases.

Runge-Kutta Routine

The numerical technique to solve the Poisson-Boltzmann equation was a fourth order Runge-Kutta method with a Newton-Raphson shoot to help converge the guessed value of the centerline potential G_i at the i^{th} iteration to its correct value (58). In all cases the Runge-Kutta subroutine contained four functions

$$F_i = \frac{dY_i}{dx_p} \tag{A-1}$$

The Y_i have the following form for the cylindrical pore

$$Y_1 = \Psi \qquad\qquad Y_3 = \frac{\partial Y_1}{\partial G_i} \tag{A-2}$$

$$Y_2 = x_p \frac{\partial Y_1}{\partial x_p} \qquad\qquad Y_4 = \frac{\partial Y_2}{\partial G_i}$$

and the following for the slit pore

$$Y_1 = \Psi \qquad\qquad Y_3 = \frac{\partial Y_1}{\partial G_i} \tag{A-3}$$

$$Y_2 = \frac{\partial Y_1}{\partial x_p} \qquad\qquad Y_4 = \frac{\partial Y_2}{\partial G_i}$$

The initial conditions for the functions at the pore centerline ($x_p = 0$) for the i^{th} iteration are

$$Y_i = G_i \tag{A-4}$$

$$Y_2 = 0$$

$$Y_3 = 1$$

$$Y_4 = 0$$

The Newton-Raphson shoot for estimating the $(i+1)^{th}$ guess for the centerline potential from G_i is

$$G_{i+1} = G_i - \frac{Y_2(1) - S_w}{Y_4(1)} \tag{A-5a}$$

when the wall potential boundary is used, and

$$G_{i+1} = G_i - \frac{Y_1(1) - \psi(1)}{Y_3(1)} \qquad \text{(A-5b)}$$

when the wall potential boundary condition is used.

The Runge-Kutta routine was considered to have converged when $(G_{i+1} - G_i)/G_{i+1} < EPS$ where $EPS = 10^{-7}$ was the required numerical accuracy. As long as there was a good first estimate for the routine there were no problems of convergence, unless the potential profile was nearly flat. In that case, an increase of the number of steps or an increase of the value of EPS usually resulted in convergence.

Computer Output

Besides the potential profile, the output of the computer programs written for our calculations included the integrals necessary to calculate the coefficients of the electrokinetic fluxes (equations (2-12)), as well as estimates for the pore fluid conductivity, the streaming potential, the streaming current, and the exclusion-diffusion potential for the combination of wall charge (or wall potential) and a/D for which the profile was calculated.

As an example of the computer programs written to solve the Poisson-Boltzmann equation in the various cases examined, we give below the program that solves the Poisson-Boltzmann equation in a cylindrical pore with the wall charge boundary condition used. The first part of the program uses the equations in Appendix C to calculate an estimate for the centerline potential which is fed to the Runge-Kutta routine.

The routine gave a very good estimate of the centerline potential in most cases. We should note that the subroutines "mmbsi0" and "mmbsi1" that are called in the program are the IMSL subroutines for calculating the Bessel functions I_0 and I_1. These routines are not included below.

Algorithm for the Numerical Solution of the Poisson-Boltzmann Equation

```
      implicit real*8(a-h,o-z)
c     this is program negch.f on unix
c     it deals with negative walls
c     it uses neumann condition at the pore wall
c     it requires a value for the wall charge 'so.'
c     it uses the electrostatic potential profile found by our
c     approximate solutions in Appendix C as
c     a first guess for the runge-kutta solution
c
      double precision mmbsi0,mmbsi1,f,g,gold,delg
      integer i,ier,iero,ier1,iopt,m,ma,n
      dimension yl(45),yh(45),ya(45)
      dimension yi(4),y(4,45),f1(4),f2(4),f3(4),f4(4),
     &p(4,45),rad(45)
      double precision yi,y,f1,f2,f3,f4,yl,p,rad,yl,yh,ya,umi,upi
      double precision so,al,arg,p,strmpl,poco1,pomig,pocon,porat
      double precision dabs, dexp, datan, dlog, dsqrt,strcu,strcul
      double precision yl1,yl2,yl3,yl4,yl5,yl41,yl51,pocon1,pomig1,
     &porat1
      common /st/p,1
      common /ida/iopt,ier
      common /da/so,al,arg
      open (4,file='dawch',status='old')
c     open (7,file='output',status='new')
      open (7,file='sdata',status='new')
      open (8,file='wchout',status='new')
c     open (9,file='pocon',status='new')
      open (1,file='dawchx',status='new')
      open (2,file='dawchye',status='new')
      open (3,file='dawchyn',status='new')
      rewind 4
c-----------------------------------------------------------------
      iopt=1
c     valences of ions:
c     negative
      zm=-1.0d+00
c     positive
      zp=+1.0d00
c-----------------------------------------------
c     put comments later on
c     al in the approximate solution is the same as ak in the
c     runge-kutta solution
c     they are both defined as the pore radious over the
c     debye length (classical definition)
c     al in the runge-kutta is the pore radius over the debye
c     length (our model definition; without division by the sum
c     of the valences)
c     we need that definition of al for the runge-kutta
c     the plots and presentations are with respect to the
```

```
c     classical definition
c
c-----------------------------------------------------
c
c     por : pore radius in angstrom
c     upi : cation mobility in m2/sV
c     umi : anion mobility in m2/sV
c
      read (4,412) por,upi,umi
  412 format(3f15.8)
  413 read(4,414,end=114) so,am,eps,m
  414 format(3f16.4,i3)
c     write (6,415) so,am,eps,m
  415 format(2x,3f16.7,i3)
      al=am
c     interval size in r:
      h=1.d+00/dble(float(m))
c     number of points along r:
      n=m+1
c     parameter to support calculations
      ma=m+2
c------------------------------------------------------------
c     approximate solution
c     in the following we use bisection to find rc:critical radius
c     r: rcl and rcr, limits for bisection
c     err: error in r-critical evaluation
      err=1.0d-03
c     yl1: low potential approximate profile at the pore wall
c     yl0: low potential approximate profile at the center line
c     yh0: high potential approximate profile at the pore wall
      yl1=(so/al)*(mmbsi0(iopt,al,ier)/mmbsi1(iopt,al,ier))
      yl0=(so/al)*(1.d+00/mmbsi1(iopt,al,ier))
      yh0=dlog((al**2)*(so-4.d+00)/(16.d+00*so))
c     write (6,879) yl1,yl0,yh0
  879 format(3x,3(d16.9,4x))
      if (dabs(yl1) .lt. 1.d+00) goto 20
      if ((dabs(yl0) .gt. 1.d+00) .and. (dabs(yh0) .gt. 1.d+00))goto 22
      if ((2.158/al) .lt. 1.d+00) goto 123
c     r-critical evaluation for positive gamma
c     subdomain iib
  111 rcl=0.0d+00
      rcr=1.0d+00
      if ((2.158/al) .lt. 1.d+00) rcr=2.158/al
   60 gaml=(al*rcl*(mmbsi1(iopt,al*rcl,ierl)/
     &mmbsi0(iopt,al*rcl,ierl))+2.d+00)
     &**2-(al*rcl)**2*dexp(1.0d+00)
      gamr=(al*rcr*(mmbsi1(iopt,al*rcr,ierr)/
     &mmbsi0(iopt,al*rcr,ierr))+2.d+00)
     &**2-(al*rcr)**2*dexp(1.d+00)
c     write (6,800) gaml,gamr,rcl,rcr
  800 format(2x,'gaml= ',d16.9,3x,'gamr= ',d16.9,2(2x,f10.4))
      all=dsqrt(gaml)
      alr=dsqrt(gamr)
      anl=(al*rcl*((so-2.d+00+all)*rcl**all-(so-2.d+00-all)))**2
      adl=4.d+00*all**2*rcl**all*(so-2.d+00+all)*(so-2.d+00-all)
      if (rcl .lt. 1.d-03) goto 66
      yhl=dlog(anl/adl)+1.d+00
      goto 67
   66 yhl=dlog((al**2)*(so-4.d+00)/(16.d+00*so))+1.d+00
   67 anr=(al*rcr*((so-2.d+00+alr)*rcr**alr-(so-2.d+00-alr)))**2
      adr=4.d+00*alr**2*rcr**alr*(so-2.d+00+alr)*(so-2.d+00-alr)
      yhr=dlog(anr/adr)+1.d+00
      if ((yhl*yhr) .gt. 0.d+00) goto 61
      if ((rcr-rcl) .lt. 2.d+00*err) goto 62
      temp=rcl
      rcl=(rcl+rcr)/2.d+00
      goto 60
   61 rcr=rcl
      rcl=temp
      rcl=(rcl+rcr)/2.d+00
      goto 60
   62 rc=(rcl+rcr)/2.d+00
      gam=(gaml+gamr)/2.d+00
      goto 122
c
c     the following procedure might create some problems
c     when al=2.158 or very close to this value.
c     this is because gam=0 in this case.
c
c     r1c: critical radius to ck in which subdomain we
c          are in; if at r=r1c
c          pot gt 1 => subdomain iib
c          pot lt 1 => subdomain iia
c          pot  = 1 => junction of iia and iib
c     y1c: potential at r1c
c     gamr1c: gamma value at r1c, it should be around zero
c
  123 r1c=2.158d+00/al
      gamr1c=(al*r1c*(mmbsi1(iopt,al*r1c,ierl)/
     &mmbsi0(iopt,al*r1c,ierl))+2.d+00)
     &**2-(al*r1c)**2*dexp(1.0d+00)
      y1c=dlog(((al*r1c)/(2.d+00-so)-al*(r1c/2.d+00)
     &*dlog(r1c))**2)
c     write (7,789) r1c,gamr1c,y1c
  789 format(5x,'r1c=',d15.8,1x,'gamr1c=',d15.8,1x,'y1c=',d15.8)
c     the equation for y1c will give positive potentials for
c     negative 'so' values at large 'al.'
c     but at large 'al' we will probably be in subdomain 'iia'
c     that is 'gam .lt. 0', so try
      if (y1c .gt. 0d+00) goto 68
      if (dabs(y1c) .gt. 1.d+00) goto 111
   68 rcl=2.158d+00/al
c     need r*>2.158:al for negative gamma,subdomain iia
      rcr=1.d+00
      err=1.d-03
   70 gaml=(al*rcl*(mmbsi1(iopt,al*rcl,ierl)/
     &mmbsi0(iopt,al*rcl,ierl))+2.d+00)
     &**2-(al*rcl)**2*dexp(1.0d+00)
      gamr=(al*rcr*(mmbsi1(iopt,al*rcr,ierr)/
     &mmbsi0(iopt,al*rcr,ierr))+2.d+00)
     &**2-(al*rcr)**2*dexp(1.d+00)
      if (gaml .gt. 0.d+00) gaml=-gaml
      if (gamr .gt. 0.d+00) gamr=-gamr
      all=dsqrt(-1.d+00*gaml)
      alr=dsqrt(-1.d+00*gamr)
      if (rcl .lt. err) goto 76
      yhl=dlog(((al*rcl*dcos((all/2.d+00)*dlog(rcl)+
     &datan((2.d+00-so)/all)))/all)**2)+1.d+00
      goto 77
   76 yhl=dlog((al**2)*(so-4.d+00)/(16.d+00*so))+1.d+00
   77 yhr=dlog(((al*rcr*dcos((alr/2.d+00)*dlog(rcr)+
     &datan((2.d+00-so)/alr)))/alr)**2)+1.d+00
      if ((yhl*yhr) .gt. 0.d+00) goto 71
      if ((rcr-rcl) .lt. 2.d+00*err) goto 72
      temp=rcl
      rcl=(rcl+rcr)/2.d+00
      goto 70
   71 rcr=rcl
      rcl=temp
      rcl=(rcl+rcr)/2.d+00
      goto 70
   72 rc=(rcl+rcr)/2.d+00
      gam=(gaml+gamr)/2.d+00
  122 if (dabs(gam) .lt. 1.d-04) gam=0.d+00
c     write (7,32) so,al,gam,rc
   32 format(16x,'mixed potential approximation profile'/
     &9x,51(1h-)/10x,'so= ',d16.9,5x,'al= ',d16.9/
     &10x,'gamma costant= ',d16.9/
     &10x,'critical radius= ',d16.9/
     &16x,'position',12x,'profile',7x,'ier1',1x,'ier2')
      do 50 ji=2,ma
      r=dble(float(ji-2))*h
      if (r .gt. rc) goto 51
      ya(ji)=(-1.d+00)*(mmbsi0(iopt,al*r,ier1)/
     &mmbsi0(iopt,al*rc,ier2))
c     write (7,24) r,ya(ji),ier1,ier2
      goto 50
   51 if (gam .lt. 0.d+00) goto 52
      if (gam .gt. 0.d+00) goto 53
c     if gam .eq. 0.d+00 continue
      ya(ji)=2.d+00*dlog((r/rc)*dexp(-1.d+00*.5d+00)-al*
     &(r/2.d+00)*dlog(r/rc))
c     write (7,24) r,ya(ji),ier1,ier2
      goto 50
   52 alfa=dsqrt(-1.d+00*gam)
      ya(ji)=dlog(((al*r*dcos((alfa/2.d+00)*dlog(r)+
     &datan((2.d+00-so)/alfa)))/alfa)**2)
c     write (7,24) r,ya(ji),ier1,ier2
      goto 50
   53 alfa=dsqrt(gam)
      anom=(al*r*((so-2.d+00+alfa)*(r**alfa)-(so-2.d+00-alfa)))**2
      adenom=4.d+00*(alfa**2)*(r**alfa)*(so-2.d+00+alfa)*
     &(so-2.d+00-alfa)
      ya(ji)=dlog(anom/adenom)
c     write (7,24) r,ya(ji),ier1,ier2
   50 continue
      goto 12
   20 continue
c     write (7,25) so,al
   25 format(17x,'low potential approximation profile'/
     &9x,51(1h-)/
     &10x,'so= ',d16.9,5x,'al= ',d16.9/
     &10x,'      position',12x,'profile',7x,
     &'ier0',1x,'ier1')
      do 23 i=2,ma
      r=dble(float(i-2))*h
      yl(i)=(so/al)*(mmbsi0(iopt,al*r,ier0)/mmbsi1(iopt,al,ier1))
      ya(i)=yl(i)
c     write (7,24) r,yl(i),ier0,ier1
   23 continue
   24 format(10x,2(d16.9,4x),2(i3,2x))
      goto 12
   22 rc=0.d+00
      as1=mmbsi1(iopt,al*rc,ier)
      as0=mmbsi0(iopt,al*rc,ier)
      gam=(al*rc*(as1/as0)+2.d+00)**2-
     &al**2*rc**2*dexp(1.d+00)
c     write (7,30) so,al,gam
   30 format(16x,'high potential approximation profile'/
     &9x,51(1h-)/10x,'so= ',d16.9,5x,'al= ',d16.9/
     &10x,'gamma constant= ',d16.9/
     &16x,'position',12x,'profile',7x,'ier0',1x,'ier1')
      do 31 j=2,ma
      r=dble(float(j-2))*h
      yh(j)=dlog((al**2*(so-4.d+00)*(r**2*(so/(so-4.d+00))-1.d+00)
     &**2)/(16.d+00*so))
      ya(j)=yh(j)
      ier0=0.d+00
      ier1=0.d+00
c     write (7,24) r, yh(j),ier0,ier1
   31 continue
   12 continue
c     write (7,21) yl1,yl0
   21 format(10x,'yl(r=1)= ',d16.9,5x,'yl(r=0)= ',d16.9/
     &10x,'program terminates')
      ipart=1
      mb=ma-1
      do 26 jc=1,mb
      if (dabs(ya(jc+1)) .lt. dabs(ya(jc))) goto 104
      if (ya(jc+1) .gt. 0.d+00) goto 104
   26 continue
   27 do 33 jb=1,ma
   33 y(1,jb)=ya(jb+1)
      ipart=1
c     goto 121
  120 ipart=10
c
c----------------------------------------------------------
c
      yi(2)=0.d+00
      yi(3)=1.d+00
      yi(4)=0.d+00
c     initially choose only one ak value
c     ak in runge-kutta is the al in the approximating solution
      ak=al
c     initial guess of center potential psi(r=0):
      g=ya(2)
c     write (6,321) g
  321 format(10x,'g= ',d16.9)
c     number of iterations: it
      it=0
c
  222 yi(1)=g
      gold=g
c     number of intervals in r: m
c     interval size in r:
      h=1.d+00/dble(float(m))
c     number of positions along r:
      n=m+1
c     maximum allowed number of iterations:
      itemax=100
c     allowed error in surface potential psi(r=1): eps
c------------------------------------------------------------------
      it=it+1
c     call runge-kutta for each ak;
      al=ak/dsqrt(zp-zm)
      if (g .gt. 0.d+00) g=0.d+00
      call runge(yi,y,h,zp,zm,al,m)
      goto 999
c
  101 continue
c     write (7,400) zp,zm
  400 format(5x,' ion valences: positive= ',f5.2,3x,
     &'negative= ',f5.2)
      alfa=al*dsqrt(zp-zm)
c     write (7,401) so,alfa
  401 format(5x,'so= ',f11.6,3x,'pore radius over deb. length= ',f10.6)
c     write (7,402) m,eps
  402 format(5x,'no. of intervals: ',i3,8x,'allowed error in',1x,
     &'psi(w)= ',d12.5)
```

```
c     write (7,403)
  403 format(11x,'position',16x,'psi',16x,' rdy/dr')
      goto 102
c
c     new newton-raphson estimate os phi(r=1)
  999 g=gold-(y(2,n)-so)/y(4,n)
c
c     write (7,405) gold,g
  405 format(5x,'old guess=',d15.8,3x,'new guess=',d15.8)
c     aid to convergence
      if (g .gt. 0.d+00) g=-(gold**2)
c     is gold good enough?
      delg=dabs((g-gold)/g)
      if (delg .lt. eps .or. it .gt. itemax) goto 101
      goto 222
c
  102 if (it .lt. itemax) goto 103
c     write (7,500) it
  500 format(5x,'guessed psi(r=0) did not converge after ',i4,1x,
     &'iterations'/4x,53('-'))
      goto 104
  103 continue
c 103 do 43 ja=1,n
c     ra=dble(float(ja-1))*h
c  43 write (7,404) ra,(y(la,ja),la=1,2)
c     write (7,439)
  439 format(8x,65(1h-)/10x,'position',16x,'y13',16x,'  y14')
c     do 435 ja=1,n
c     ra=dble(float(ja-1))*h
c 435 write (7,404) ra,(y(la,ja),la=3,4)
  404 format(7x,d16.8,2x,2(3x,d17.8))
c
c     call simpsons rule
c     simpsons rule integration of:
c     sm1:   r*em*dr
c     sm2:   r*(psi(w)-psi(r))*dr
c     sp1:   r*ep*dr
c     sp2:   r*(psi(w)-psi(r))*dr
c     psiav: 2*r*psi*dr
c     integrals are from 0 to 1 w.r.t. r, where
c     em=exp(-zm*psi)
c     ep=exp(-zp*psi)
c
  121 do 105 is=1,n
  105 rad(is)=dble(float(is-1))*h
      call sim(y,rad,m,h,zp,zm,sm1,sp1,sm2,sp2,psiav)
c     write (7,406) sm1,sm2,sp1,sp2,psiav
  406 format(25x,'sm1= ',d19.8/25x,'sm2= ',d19.8/25x,'sp1= ',d19.8/
     &25x,'sp2= ',d19.8/25x,'psiav= ',d17.8/23x,27(1h-))
c     write (7,410)
  410 format(11x,'position',15x,'dy/dg',13x,'dydy/drdg')
c     do 106 ja=1,n
```

```
c     ra=dble(float(ja-1))*h
c 106 write (7,404) ra,(y(la,ja),la=3,4)
c
c     calculate needed quantities;
      yl1=y(1,n)-psiav
      yl2=sp2-sm2
      yl3=(sp2/zp)-(sm2/zm)
c     need to give ionic mobilities;
c     up,um, m2/sec*volt
c     up1,um1 in m2*mol/J*sec
      do 888 ias=1,2
      um=umi
      up=upi
c     if (ias .eq. 2) up=up/2.d+00
      if (ias .eq. 2) up=up
      up1=up/9.6487d+04
      um1=um/9.6487d+04
      yl4=up1*sp1-um1*sm1
      yl5=zp*up1*sp1-zm*um1*sm1
      if (ias .eq. 1) yl41=yl4
      if (ias .eq. 1) yl51=yl5
c     write (7,407) yl1,yl2,yl3,yl4,yl5
  407 format(10x,'yl1=',d19.8/10x,'yl2=',d19.8/10x,'yl3=',d19.8/
     &10x,'yl4=',d19.8/10x,'yl5=',d19.8)
c
      if (ipart .eq. 1) ak=al
      die=32.62d+00
      e=8.854d-12*die
      tem=0.29816d+03
      vi=0.5421d-03
      rg=0.8314d+01
      c1=e*rg*tem/vi
      far=9.6487d+04
      ef=far**2
      con=(((ak/5.029d+01)/por)**2)*(die*tem)
      poco=-(2.d+04)*con*(c1*yl2-ef*yl5)
c     pomig is the pore conductivity due to migration.
c     pocon is the pore conductivity due to convection,
c     i.e., electroosmosis.
c     porat is the ratio of the two contributions
      pomig=-(2.d+04)*con*(-ef*yl5)
      pocon=-(2.d+04)*con*c1*yl2
      porat=pomig/pocon
      if (ias .eq. 1) porat1=porat
      if (ias .eq. 1) pomig1=pomig
      if (ias .eq. 1) pocon1=pocon
      omega=2.d+00*(-ef*yl4+c1*(yl3-yl1))/(-ef*yl5+c1*yl2)
      strmp=((10.d+00*e*rg*tem)/(far*vi*poco))*yl1
c     wm: membrane width; m
c     strcu=(strmp*poco/10.d+00)*wm
c     pora: pore radius in m
c     np: number of pores
```

```
      pi=3.14159d+00
      pora=por*(1.d-10)
      wm=7.697d-06
      np=75071
      ap=((float(np))*pi*(pora**2))/wm
      strcu=((e*rg*tem)/(far*vi))*y11*ap
      if (ias .eq. 1) strcul=strcu
      if (ias .eq. 1) pocol=poco
      if (ias .eq. 1) strmpl=strmp
c     write (7,409) up,um,die,vi
  409 format(10x,'up=',d19.8,2x,'um=',d19.8,2x,'m2/(s*v)'/9x,
     &'die=',d19.8,2x,'vi=',d19.8,2x,'pa*s')
c     write (7,411) por,con
  411 format(15x,'pore radius=',d16.9,2x,'a'/
     &15x,'concentration=',d16.9,2x,'mol/lt')
c     write (7,408) cl,poco,omega,strmp
  408 format (15x,'cl=',d19.8/
     &15x,'pore cond.=',d19.8,2x,'ms/cm'/
     &15x,'capital omega=',d19.8/
     &15x,'stream. pot.=',d19.8,2x,'v/pa'/8x,62(1h-))
      if (ias .eq. 1) omegal=omega
c     if (ias .eq. 1) write (9,423) so,ak,omega
c     if (ias .eq. 2) write (10,423) so,ak,omega
  888 continue
  423 format(d16.9,',',d16.9,',',d16.9)
      allog=dlog10(ak)
      write (8,422) so,ak,allog,g,y(1,n),por,con,m,pocol,poco,
     &strmpl,strmp,strcul,strcu,omegal,omega
      write (8,436) sml,sm2,spl,sp2,psiav,y11,y12,y13,
     &y141,y14,y151,y15,poconl,pocon,pomigl,pomig,poratl,porat
c     write (9,424) so,ak,allog,sml,sm2,spl,sp2,psiav,y11,y12,y13,
c     &y141,y14,y151,y15,poconl,pocon,pomigl,pomig
      write (1,437) ak
      write (2,437) pocol
      write (3,437) poco
  437 format (d15.8)
  422 format (12x,'so= ',d16.9/12x,
     &'pore radius over debye length= ',d16.9/
     &12x,'log10(dl)= ',d16.9/12x,'initial guess of psi(r=0): ',d16.9/
     &12x,'value of the wall potential: ',d16.9/
     &12x,'pore radius= ',d16.9,' a'/12x,'bulk concen. ',d16.9,2x,
     &'mol/lt'/
     &30x,'number of steps: m= ',i5/40x,'up=um',15x,'up<um'/
     &12x,'pore conductivity    ',d16.9,5x,d16.9,' ms/cm'/
     &12x,'streaming potential  ',d16.9,5x,d16.9,' v/pa'/
     &12x,'streaming current    ',d16.9,5x,d16.9,' a/pa'/
     &12x,'capital omega        ',d16.9,5x,d16.9/10x,66(1h-))
  424 format(12x,'so= ',d16.9/
     &12x,'pore radius over debye length: ',d16.9/
     &12x,'log10(deb. length): ',d16.9/
     &12x,'sml= ',d16.9,5x,'sm2= ',d16.9/
     &12x,'spl= ',d16.9,5x,'sp2= ',d16.9/
     &12x,'psiav= ',d16.9/
     &12x,'y11=',d16.9,2x,'y12=',d16.9,2x,'y13=',d16.9/
     &40x,'up=um',15x,'up<um'/
     &12x,'y14 for              ',d16.9,5x,d16.9/
     &12x,'y15 for              ',d16.9,5x,d16.9/
     &12x,'pore con. from convn ',d16.9,5x,d16.9/
     &12x,'pore con. from migr. ',d16.9,5x,d16.9/10x,67(1h-))
  436 format(/
     &12x,'sm1= ',d16.9,5x,'sm2= ',d16.9/
     &12x,'sp1= ',d16.9,5x,'sp2= ',d16.9/
     &12x,'psiav= ',d16.9/
     &12x,'y11=',d16.9,2x,'y12=',d16.9,2x,'y13=',d16.9/
     &40x,'up=um',15x,'up<um'/
     &12x,'y14 for              ',d16.9,5x,d16.9/
     &12x,'y15 for              ',d16.9,5x,d16.9/
     &12x,'pore con. from convn ',d16.9,5x,d16.9/
     &12x,'pore con. from migr. ',d16.9,5x,d16.9/
     &12x,'ratio migr:conv term ',d16.9,5x,d16.9/10x,67(1h*))
      write (7,444) so,ak,omega1
  444 format(d17.8,2(',',d17.8))
      if (ipart .eq. 1) goto 120
      goto 413
  104 continue
c     write (7,399) am,ak,so
      write (8,399) am,ak,so
  399 format(15x,'the program is forced to terminate'/10x,'dble am=',
     &d15.7,5x,'dble ak=',d15.7,5x,'so= ',d15.7/10x,67(1h*))
c     if (ipart .eq. 1) goto 27
      goto 413
  114 stop
      end
c--------------------------------------------------------------------
c     subroutine runge-kutta
      subroutine runge(yi,y,h,zp,zm,a1,m)
      implicit real*8(a-h,o-z)
      dimension y(4,45),yi(4),rk(4,4),p(4,45)
      double precision y,yi,rk,p,r,h,f,a1,zp,zm
      integer i,j,l,m,ma
      common /st/p,l
      do 20 j=1,4
   20 y(j,1)=yi(j)
      ma=m+2
      do 21 i=2,ma
      l=i-1
      r=dble(float(i-2))*h
      do 22 j=1,4
   22 p(j,l)=y(j,l)
      do 23 j=1,4
   23 rk(j,1)=h*f(r,j,zp,zm,a1)
      do 24 j=1,4
   24 p(j,l)=y(j,l)+rk(j,1)/2.d+00
      do 25 j=1,4
   25 rk(j,2)=h*f(r+h/2.d+00,j,zp,zm,al)
      do 26 j=1,4
   26 p(j,l)=y(j,l)+rk(j,2)/2.d+00
      do 27 j=1,4
   27 rk(j,3)=h*f(r+h/2.d+00,j,zp,zm,al)
      do 28 j=1,4
   28 p(j,l)=y(j,l)+rk(j,3)
      do 29 j=1,4
   29 rk(j,4)=h*f(r+h,j,zp,zm,al)
      do 30 j=1,4
   30 y(j,i)=y(j,l)+(1.d+00/6.d+00)*(rk(j,1)+2.d+00*rk(j,2)+
     &2.d+00*rk(j,3)+rk(j,4))
   21 continue
      return
      end
c-------------------------------------------------------------
c     function f
      double precision function f(r,j,zp,zm,al)
      implicit real*8(a-h,o-z)
      dimension p(4,45)
      double precision r,zp,zm,al,p,ap,ep,am,em
      double precision dexp
      integer l,j
      common /st/p,l
      ap=(-1.d+00)*zp*p(1,l)
      ep=dexp(ap)
c     ep=1.d+00/dexp((-1.d+00)*ap)
      am=(-1.d+00)*zm*p(1,l)
      em=dexp(am)
      if (r .lt. 1.d-04) goto 30
    5 goto (9,10,11,12),j
      f=j
    9 f=p(2,l)/r
      goto 20
   10 f=r*(al**2)*(em-ep)
      goto 20
   11 f=p(4,l)/r
      goto 20
   12 f=r*p(3,l)*(al**2)*(zp*ep-zm*em)
      goto 20
   30 if (j .eq. 1 .or. j .eq. 3) goto 31
      goto 5
   31 f=0.d+00
   20 return
      end
c-------------------------------------------------------------
c     simpsons subroutine
      subroutine sim(y,rad,m,h,zp,zm,sm1,sp1,sm2,sp2,psiav)
      implicit real*8(a-h,o-z)
      dimension y(4,45),rad(45)
      double precision y,rad,zp,zm,sp1,sp2,sm1,sm2,psiav,h
      double precision emj,emk,epj,epk,epw,emw
      double precision dexp
      integer m,itsimp,n,i,j,k
c
c     initialize sums:
      sm1=0.d+00
      sp1=0.d+00
      sm2=0.d+00
      sp2=0.d+00
      psiav=0.d+00
c
c     number of simpson's rule steps:
      itsimp=m/2.d+00
c     index of wall potential (psi(n)):
      n=m+1
c
c     start integration
      do 100 i=1,itsimp
      j=2*i
      k=j-1
      emj=dexp((-1.d+00)*zm*y(1,j))
      emk=dexp((-1.d+00)*zm*y(1,k))
      epj=dexp((-1.d+00)*zp*y(1,j))
      epk=dexp((-1.d+00)*zp*y(1,k))
      sm1=sm1+4.d+00*rad(j)*emj+2.d+00*rad(k)*emk
      sm2=sm2+4.d+00*rad(j)*(y(1,n)-y(1,j))*emj+
     &2.d+00*rad(k)*(y(1,n)-y(1,k))*emk
      sp1=sp1+4.d+00*rad(j)*epj+2.d+00*rad(k)*epk
      sp2=sp2+4.d+00*rad(j)*(y(1,n)-y(1,j))*epj+
     &2.d+00*rad(k)*(y(1,n)-y(1,k))*epk
      psiav=psiav+4.d+00*rad(j)*y(1,j)+2.d+00*rad(k)*y(1,k)
  100 continue
c
      emw=dexp((-1.d+00)*zm*y(1,n))
      epw=dexp((-1.d+00)*zp*y(1,n))
      sm1=(sm1+rad(n)*emw)*(h/3.d+00)
      sm2=sm2*(h/3.d+00)
      sp1=(sp1+rad(n)*epw)*(h/3.d+00)
      sp2=sp2*(h/3.d+00)
      psiav=(psiav+rad(n)*y(1,n))*(h/3.d+00)*2.d+00
      return
      end
```

APPENDIX B
MODEL COEFFICIENTS

The coefficients for the equations (2-12) are presented below. They are written as area averages over the pore cross section. The area average of a quantity Q is defined as

$$< Q > = 2\int_0^1 x_p Q dx_p \qquad \text{(B-1)}$$

for a cylindrical pore, and, as

$$< Q > = \int_0^1 Q dx_p \qquad \text{(B-2)}$$

for an infinite slit pore. The coefficients in equations (2-12) are as follows

$$L_{11} = -\frac{L^2}{8\eta} \qquad \text{(B-3a)} \quad \text{(Cylinder)}$$

$$L_{11} = -\frac{L^2}{3\eta} \qquad \text{(B-3b)} \quad \text{(Slit)}$$

$$L_{12} = -\frac{C_b L^2}{4\eta}\left\langle\left[\frac{\exp(-z_+\Psi)}{z_+} - \frac{\exp(-z_-\Psi)}{z_-}\right]\left[1-x_p^2\right]\right\rangle \qquad \text{(B-4a)} \quad \text{(Cylinder)}$$

$$+\frac{C_b L^2}{8\eta}\left[\frac{1}{z_+} - \frac{1}{z_-}\right]$$

$$L_{12} = -\frac{C_b L^2}{4\eta}\left\langle\left[\frac{\exp(-z_+\Psi)}{z_+} - \frac{\exp(-z_-\Psi)}{z_-}\right]\left[1-x_p^2\right]\right\rangle \qquad \text{(B-4b)} \quad \text{(Slit)}$$

$$+\frac{C_b L^2}{3\eta}\left[\frac{1}{z_+} - \frac{1}{z_-}\right]$$

$$L_{13} = \frac{\varepsilon kT}{e\eta}\left[\Psi(1) - <\Psi>\right] \qquad \text{(B-5)} \quad \text{(Cylinder or Slit)}$$

$$L_{21} = -\frac{C_b L^2}{4\eta}\left\langle\left[\frac{\exp(-z_+\Psi)}{z_+} - \frac{\exp(-z_-\Psi)}{z_-}\right]\left[1-x_p^2\right]\right\rangle \qquad \text{(B-6a)} \quad \text{(Cylinder)}$$

$$L_{21} = -\frac{C_b L^2}{2\eta}\left\langle\left[\frac{\exp(-z_+\Psi)}{z_+} - \frac{\exp(-z_-\Psi)}{z_-}\right]\left[1-x_p^2\right]\right\rangle \tag{B-6b}$$

(Slit)

$$L_{22} = C_b\left\langle -U_+\frac{\exp(-z_+\Psi)}{z_+} + U_-\frac{\exp(-z_-\Psi)}{z_-}\right\rangle \tag{B-7a}$$

(Cylinder)

$$-\frac{C_b^2 L^2}{\eta}\left\langle\left[\frac{\exp(-z_+\Psi)}{z_+} - \frac{\exp(-z_-\Psi)}{z_-}\right]\right.$$

$$\left.\int_{\xi}^{1}\frac{1}{\xi_2}\int_0^{\xi_2}\xi_1\left[\frac{\exp(-z_+\Psi)}{z_+} - \frac{\exp(-z_-\Psi)}{z_-}\right]d\xi_1 d\xi_2\right\rangle$$

$$+\frac{C_b^2 L^2}{4\eta}\left[\frac{1}{z_+} - \frac{1}{z_-}\right]\left\langle\left[\frac{\exp(-z_+\Psi)}{z_+} - \frac{\exp(-z_-\Psi)}{z_-}\right]\left[1-x_p^2\right]\right\rangle$$

$$L_{22} = C_b \left\langle -U_+ \frac{\exp(-z_+\Psi)}{z_+} + U_- \frac{\exp(-z_-\Psi)}{z_-} \right\rangle \qquad \begin{matrix}\text{(B-7b)}\\ \text{(Slit)}\end{matrix}$$

$$- \frac{C_b{}^2L^2}{\eta} \left\langle \left[\frac{\exp(-z_+\Psi)}{z_+} - \frac{\exp(-z_-\Psi)}{z_-} \right] \right.$$

$$\left. \int_{\xi}^{1} \int_{0}^{\xi_2} \left[\frac{\exp(-z_+\Psi)}{z_+} - \frac{\exp(-z_-\Psi)}{z_-} \right] d\xi_1 d\xi_2 \right\rangle$$

$$+ \frac{C_b^2L^2}{2\eta} \left[\frac{1}{z_+} - \frac{1}{z_-} \right] \left\langle \left[\frac{\exp(-z_+\Psi)}{z_+} - \frac{\exp(-z_-\Psi)}{z_-} \right] \left[1-x_p^2 \right] \right\rangle$$

$$L_{23} = - eC_b \left\langle U_+ \exp(-z_+\Psi) - U_- \exp(-z_-\Psi) \right\rangle$$

(B-8)
(Cylinder or Slit)

$$+ \frac{\varepsilon C_b kT}{e\eta} \left\langle \left[\Psi(1) - \Psi \right] \left[\frac{\exp(-z_+\Psi)}{z_+} - \frac{\exp(-z_-\Psi)}{z_-} \right] \right\rangle$$

$$L_{31} = \frac{\varepsilon \kappa T}{e\eta} \left[\Psi(1) - < \Psi > \right]$$

(B-9)
(Cylinder or Slit)

$$L_{32} = eC_b \left\langle -U_+ \exp(-z_+\Psi) + U_- \exp(-z_-\Psi) \right\rangle$$

(B-10)
(Cylinder or Slit)

$$+ \frac{\varepsilon C_b kT}{e\eta} \left\langle \left[\Psi(1) - \Psi \right] \left[\frac{\exp(-z_+\Psi)}{z_+} - \frac{\exp(-z_-\Psi)}{z_-} \right] \right\rangle$$

$$- \frac{\varepsilon C_b kT}{e\eta} \left[\frac{1}{z_+} - \frac{1}{z_-} \right] \left[\Psi(1) - < \Psi > \right]$$

$$L_{33} = -e^2 C_b \left\langle z_+ U_+ \exp(-z_+\Psi) \right. \qquad \text{(B-11)} \quad \text{(Cylinder or Slit)}$$

$$\left. -z_- U_- \exp(-z_-\Psi) \right\rangle$$

$$+ \frac{\varepsilon C_b kT}{n} \left\langle \left[\Psi(1) - \Psi \right] \left[\exp(-z_+\Psi) - \exp(-z_-\Psi) \right] \right\rangle$$

where L and x_p have been defined in chapter 2. Notice that the above coefficients do not follow Onsager's relations, that is $L_{ij} \neq L_{ji}$. The coefficients of a new set of fluxes defined as

$$q^* = q \qquad \text{(B-12a)}$$

$$J_s^* = J_s - C_b \left[\frac{1}{z_+} - \frac{1}{z_-} \right] q \qquad \text{(B-12b)}$$

$$I_x^* = I_x \qquad \text{(B-12c)}$$

do follow Onsager's relations.

APPENDIX C
APPROXIMATE SOLUTIONS TO THE POISSON-BOLTZMANN EQUATION IN CYLINDRICAL PORES

The charged cylindrical capillary is visualized as containing two concentric regions, the outer with $|\Psi| > 1$, and the inner with $|\Psi| < 1$, such that at their junction $R = R_1$, the potential is unity, $|\Psi(R_1)| = 1$ (see Figure C-1). Here R is the dimensionless pore radius, $R = r/a$. To ensure the continuity of the approximating equations (2-10a) and (2-10b) in the neighborhood of $R = R_1$, the following additional conditions are introduced

$$R = R_1: \qquad \Psi_L = \Psi_H = -1 \qquad \text{(C-1)}$$

$$\frac{\partial \Psi_L}{\partial R} = \frac{\partial \Psi_H}{\partial R} \qquad \text{(C-2)}$$

Hence, the approximating solutions to the Poisson-Boltzmann equation fall into three subdomains: (i) the low potential approximation in which $|\Psi| < 1$ throughout the pore (subdomain I), (ii) a matching solution in which the high and low potential approximations apply in different parts of the pore (subdomains IIA and IIB), and (iii) the high potential approximation in which $|\Psi| > 1$ throughout the pore (subdomain III). Note that the conditions (C-1) and (C-2) must be invoked only in subdomain II.

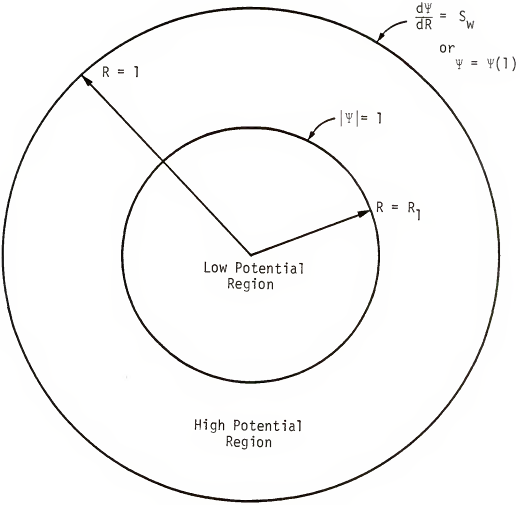

Figure C-1 Cross-section of charged capillary showing low and high potential regions whose junction is $R = R_1$

C-1 Subdomain I

In subdomain I the low potential region fills the whole pore, $|\Psi_L(R)| < 1$. Equation (2-10a) is a modified Bessel equation which can be solved subject to the wall boundary condition used, equation (2-7a) or (2-7b). Depending on the wall boundary condition used we obtain

Wall Potential Boundary Condition

$$\Psi_L = \Psi(1)\frac{I_0(Ra/D)}{I_0(a/D)} \tag{C-3}$$

where I_j is a modified Bessel function of the first kind of order "j". Equation (C-3) requires $|\Psi(1)| < 1$.

Wall Charge Boundary Condition

$$\Psi_L(R) = \frac{S_w}{a/D}\,\frac{I_0(Ra/D)}{I_1(a/D)} \tag{C-4a}$$

Equation (C-4a) is subject to

$$\frac{a}{D}\,\frac{I_1(a/D)}{I_0(a/D)} \geq -\,S_w \tag{C-4b}$$

C-2 Subdomain II

If $\Psi(R = 1) < -1$ and $\Psi(0) > -1$, at some point R_1 inside the pore the potential is equal to unity. For R less than R_1 the low potential approximation (equation (2-10a)) subject to equation (C-1) gives

$$\Psi_L(R \leq R_1) = -\frac{I_0(Ra/D)}{I_0(R_1 a/D)} \qquad \text{(C-5)}$$

For the rest of the pore ($R_1 \leq R \leq 1$) high potential approximation (equation (2-10b)) must be used. If the following variables are introduced

$$q = \ln R$$

$$t = \Psi_H(R) - 2\ln R$$

equation (2-10b) takes the form

$$\frac{\partial}{\partial q}\left(\frac{\partial t}{\partial q}\right)^2 = \left(\frac{a}{D}\right)^2 \frac{\partial}{\partial q}\exp(-t) \qquad \text{(C-6)}$$

equation (C-6) has a first integral that can be written

$$R\frac{d\Psi_H}{dR} - 2 = \pm \left\{\left(\frac{a}{D}\right)^2 R^2 \exp(-\Psi_H) + \Gamma\right\}^{\frac{1}{2}} \qquad \text{(C-7)}$$

where Γ is a constant of integration. Equation (C-1) for $\Psi_H = -1$, (C-2) for $\partial\Psi_H/\partial R$, and (C-5) for $\partial\Psi_L/\partial R$ can be used to find Γ

$$\Gamma = \left\{\frac{a}{D} R_1 \frac{I_1(R_1 a/D)}{I_0(R_1 a/D)} + 2\right\}^2 - (R_1 a/D)^2 \exp(1) \qquad \text{(C-8)}$$

Γ can assume a wide range of values depending on the value of R_1

1. $\Gamma < 0$ for $R_1 a/D > 2.158$ (subdomain IIA).

2. $\Gamma = 0$ for $R_1 a/D = 2.158$ (junction of subdomains IIA and IIB).

3. $0 < \Gamma < 4$ for $R_1 a/D < 2.158$ (subdomain IIB).

4. $\Gamma = 4$ for $R_1 = 0$ (subdomain III).

R_1 can be determined using a half-interval method to find $|\Psi_H(R_1)| = 1$. This determination of R_1 is complicated slightly by the fact that one does not know before R_1 is determined whether Ψ_H from (C-9) or (C-11) (subdomain IIA) or (C-13) or (C-14) (subdomain IIB) below should be used. However, Γ varies monotonically with R_1 for a particular a/D, so determining R_1 and Γ is not too difficult. The junction of subdomains IIA and IIB was never encountered in our calculations.

For real values of $d\Psi_H/dR$ to be obtained, equation (C-7) requires that

$$(Ra/D)^2 \exp(-\Psi_H) + \Gamma \geq 0$$

From the conditions at $R = R_1$ (equations (C-1) and (C-2)) it can be shown that only the negative square root of (C-7) can be chosen. In what follows, equation (C-7) is integrated to determine Ψ_H in various subdomains, depending on the value of Γ.

C-3 Subdomain IIA ($\Gamma < 0$)

Integration of equation (C-7) with negative Γ, that is, with $\Gamma = -\alpha^2$ where α is a real positive number, subject to equations (2-7a) and (2-7b) leads to

Wall Potential Boundary Condition

$$\Psi_H(R) = 2\ln\left[\frac{(a/D)R\cos\left[(\alpha/2)\ln R + \cos^{-1}\left\{(\alpha/(a/D))\ (\exp\Psi(1))^{\frac{1}{2}}\right\}\right]}{\alpha}\right] \le -1 \qquad \text{(C-9)}$$

Notice that equation (C-9) requires R≥0 and that

$$(\alpha/2)\ln R + \cos^{-1}\left[(\alpha/(a/D))\ (\exp\Psi(1))^{\frac{1}{2}}\right] \neq n\pi + \frac{\pi}{2} \qquad \text{(C-10)}$$

where n is an integer.

Wall Charge Boundary Condition

$$\Psi_H(R) = \ln\left[\frac{(a/D)R\cos\left(\frac{\alpha}{2}\ln R + \tan^{-1}\left(\frac{2 - S_w}{\alpha}\right)\right)}{\alpha}\right]^2 \le -1 \qquad \text{(C-11)}$$

Notice that equation (C-11) has a singularity at

$$R_L = \exp\left[\frac{2}{\alpha}\left(n\pi + \frac{\pi}{2} - \tan^{-1}\left(\frac{2 - S_w}{\alpha}\right)\right)\right] \qquad \text{(C-12)}$$

C-4 Junction of Subdomains IIA and IIB

If $\Gamma = 0$, that is, if $R_1 a/D = 2.158$, equation (C-7) is integrated subject to equations (2-7a) or (2-7b) to obtain

Wall Potential Boundary Condition

$$\Psi_H(R) = \ln\left[R\exp\frac{\Psi(1)}{2} - \frac{a}{D}\frac{R}{2}\ln R\right]^2 \leq -1 \qquad \text{(C-13)}$$

which requires $R \neq 0$.

Wall Charge Boundary Condition

$$\Psi_H(R) = \ln\left[\frac{(a/D)R}{2 - S_w} - \frac{a}{D}\frac{R}{2}\ln R\right]^2 \leq -1 \qquad \text{(C-14)}$$

which requires that R and a/D are not zero. It must be kept in mind that equations (C-13) and (C-14) do not satisfy the boundary condition (C-1), but they do satisfy equations (2-7a) or (2-7b). We have chosen to use this form of these equations because they incorporate the surface charge or the surface potential condition.

C-5 Subdomain IIB ($4 > \Gamma > 0$)

The integration of equation (C-7) with positive Γ, that is, with $\Gamma = \alpha^2$ where α is a real positive number, subject to equations (2-7a) or (2-7b) leads to

Wall Potential Boundary Condition

$$\Psi_H(R) = \ln \frac{(a/D)^2R^2}{4\alpha^2R^\alpha}\frac{(R^\alpha - A_1)^2}{A_1} \leq -1 \qquad \text{(C-15)}$$

where

$$A_1 = \frac{[\alpha^2 \exp(\Psi(1)) + (a/D)^2]^{\frac{1}{2}} + \alpha(\exp(\Psi(1)))^{\frac{1}{2}}}{[\alpha^2 \exp(\Psi(1)) + (a/D)^2]^{\frac{1}{2}} - \alpha(\exp(\Psi(1)))^{\frac{1}{2}}} \qquad \text{(C-16)}$$

Wall Charge Boundary Condition

$$\Psi_H(R) = \ln \frac{(a/D)^2 R^2 [(S_w + \alpha - 2)R^\alpha - (S_w - \alpha - 2)]^2}{4\alpha^2 R^\alpha (S_w + \alpha - 2)(S_w - \alpha - 2)} \leq -1 \qquad \text{(C-17)}$$

where $|S_w| \geq 2$.

C-6 Subdomain III

Here we have $\Gamma = 4$ and the integration of equation (C-7) subject to equations (2-7a) and (2-7b) gives

Wall Potential Boundary Condition

$$\Psi_H(R) = \ln \left[\frac{(a/D)^2}{16} \frac{(R^2 - B)^2}{B} \right] \leq -1 \qquad \text{(C-18)}$$

where B has been defined in equation (4-4b). Equation (C-18) requires

$$\frac{a}{D} \leq \frac{2.462}{B^{\frac{1}{2}}} \qquad \text{(C-19)}$$

Wall Charge Boundary Condition

$$\Psi_H(R) = \Psi_H(0) + 2\ln\left[\frac{S_w}{S_w - 4}R^2 - 1\right] \qquad \text{(C-20)}$$

where

$$\Psi(0) = \ln\frac{(a/D)^2(S_w - 4)}{16S_w} \leq -1 \qquad \text{(C-21)}$$

equation (C-21) implies that the high potential approximation cannot be used for $a/D > 2.462\left[S_w/(S_w - 4)\right]^{\frac{1}{2}}$, since $|\Psi(0)|$ must be greater than unity for the high potential approximation to apply.

APPENDIX D
MICA MEMBRANE PREPARATION

Sheets of muscovite mica 7-8 μm thick from Asheville Schoonmaker Inc. (Newport News, Va.) were placed under a heavy aluminum rod and cut into discs of 4.76 cm (1.875 in.) diameter. The discs were washed with deionized water and acetone and were allowed to dry. The actual thickness of a mica disc was determined from its weight, found with an analytical balance and from the density of mica (59).

Mica Membrane Irradiation

The mica discs were exposed to a Cf^{252} fission fragment source in a chamber designed to evacuate below 0.1 Torr (47). Since it took many hours to reach this vacuum we usually irradiated at a somewhat lower vacuum. An externally switched solenoid controlled the time of direct exposure to the source, which was 11.6 cm from the membrane. A mica membrane area 0.81 cm in diameter was exposed to the source. The irradiated area was shielded from uncollimated, background radiation by a tapered Plexiglass® collimator (3.73 cm long). Under these conditions we found only negligible background radiation, that is, of order 0.1 tracks/cm^2min when a membrane (40CT4BAC) was left in the chamber overnight at a vacuum of 0.15 Torr. However, we found that there were natural pores (1130 pores/cm^2 on membrane 27SEP4BL) on the mica sheets that we had. To minimize the effect of the natural pores on our measurements we irradiated the membrane long enough so that at least 95% of of all the pores were made by direct irradiation. This gives a maximum uncertainty in the pore sizes determined by the membrane resistance method (Chapter 6) of 5.2%. This is a maximum uncertainty since only a fraction (of order 50%) of the natural pores penetrate a membrane.

Mica Membrane Etching

All the membranes were etched in 10% (w/w) aqueous hydrofluoric acid solutions at 30.8 °C. When two membranes were irradiated together, one on top of the other, the top membrane was etched overnight in order to find the number of pores penetrating the bottom membrane, while the bottom one was etched for a controlled period of time in order to determine the pore size, and therefore the etching rate. Two different batches of hydrofluoric acid were used. The first batch, used on membranes up to number 19NOV4, had been in storage for about one year. The second batch, purchased more recently, was used with membranes beginning with number 21DEC4. The more recent membranes had a higher etching rate, as expected (1.6 to 2.5 nm/min which is in the range expected from work by others, that is 2.2 nm/min (45)). Hence, at this point we do not have enough data to calculate a reliable etching rate. Table D-1 contains all the information available from the mica membranes we prepared. A least squares fit to the irradiation rate data for membranes exposed directly to the source (the bottom membranes, denoted by "B" in Table D-1) gives

$$n = 2610 \exp(-t/6.52) \tag{D-1}$$

where t is in years, and n is in pores/cm^{2}min. This gives a half-life of 4.52 years, and with the short period spanned by the data in Table D-1, this compares favorably with the literature value of 2.65 years for the half-life (60).

Table D-1
Membrane Irradiation and Etching Data

Membrane Number	Membrane Weight (gm x 10^2)	Vacuum (Torr)	Irradiation Time (sec)	Etching Time (sec)	Track Formation Rate (#/cm^2/min)	Pore Size (nm)	Penetration Rate (%)	Notes
30SEP4B	3.783	0.19	1801.0	Overnight	2584.0	-	-	
30SEP4T	3.749	0.19	1801.0	Overnight	1999.0	-	77.0	
8OCT4B	3.825	0.18	3602.1	436.2	2670.0	12.95	-	
8OCT4T	4.055	0.18	3602.1	Overnight	2390.0	-	90.0	
17NOV4B	3.701	0.24	3601.4	5036.1	2586.0	147.4	-	pH
17NOV4T	3.059	0.24	3601.4	Overnight	2470.0	-	95.5	Expts.
19NOV4B	3.850	0.15	3607.6	386.1	2570.0	11.06	-	
19NOV4T	3.872	0.15	3607.6	Overnight	2466.0	-	96.0	
21DEC4B	3.905	0.22	3607.4	Overnight	2402.0	-	-	
21DEC4T	3.85	0.22	3607.4	Overnight	2330.0	-	97.0	
22DEC4B	3.994	0.15	3601.7	357.6	2519.0	15.07	-	
22DEC4T	3.910	0.15	3601.7	Overnight	2256.0	-	89.6	
28DEC4B	4.063	0.18	3603.5	Overnight	2380.0	-	-	
28DEC4T	3.966	0.18	3603.5	Overnight	2204.0	-	92.6	
11JAN5B	3.936	0.08	3672.5	Overnight	2512.0	-	-	
11JAN5T	3.971	0.08	3672.5	Overnight	2322.0	-	92.5	
15JAN5B	3.882	0.07	3601.3	388.15	2684.0	10.53	-	Methanol
15JAN5T	4.030	0.07	3601.3	Overnight	2444.0	-	90.2	Expts.

REFERENCES

1. L. Dresner, *J. Phys. Chem.*, *67*, 1635 (1963).

2. G. B. Westermann-Clark and J. L. Anderson, *J. Electrochem. Soc.*, *130*, 839 (1983).

3. G. B. Westermann-Clark and C. C. Christoforou, "Electrokinetic Effects in Charged Microporous Membranes for Electrolytes with Unequal Ionic Mobilities," submitted for publication (1984).

4. F. A. Morrison, Jr., and J. F. Osterle, *J. Chem. Phys.*, *43*, 2111 (1965).

5. R. J. Gross and J. F. Osterle, *J. Chem. Phys.*, *49*, 228 (1968).

6. J. C. Fair and J. F. Osterle, *J. Chem. Phys.*, *54*, 3307 (1971).

7. Y. Kobatake, Y. Toyoshima, and N. Takeguchi, *J. Phys. Chem.*, *70*, 1187 (1966).

8. K. H. Meyer and J. F. Sievers, *Helv. Chim. Acta.*, *19*, 649 (1936).

9. K. H. Meyer and J. F. Sievers, *Helv. Chim. Acta.*, *19*, 665 (1936).

10. K. H. Meyer, H. Hauptmann, and J. F. Sievers, *Helv. Chim. Acta.*, *19*, 948 (1936).

11. K. H. Meyer and J. F. Sievers, *Helv. Chim. Acta.*, *19*, 987 (1936).

12. S. Levine, J. R. Marriott, G. Neale, and N. Epstein, *J. Colloid Interface Sci.*, *52*, 136 (1975).

13. J. R. Philip and R. A. Wooding, *J. Chem. Phys.*, *52*, 953 (1970).

14. C. C. Christoforou, G. B. Westermann-Clark, and J. L. Anderson, *J. Colloid Interface Sci.* (In Press).

15. G. B. Westermann-Clark and C. C. Christoforou, *J. Mem. Sci.*, *20*, 325 (1984).

16. D. A. MacInnes, *Principles of Electrochemistry*, Reinhold, New York (1939). Chapter 13

17. K. J. Vetter, *Electrochemical Kinetics*, Academic Press, New York (1967).

18. J. J. Bikerman, *Z. Physik. Chem.*, *163A*, 378 (1933).

19. J. Th. G. Overbeek, "Electrokinetic Phenomena," in *Colloid Science*, ed. by H. R. Kruyt, vol. 1, pp. 194-243, Elsevier Publ. Co., New York (1952).

20. F. Urban, H. L. White, and E. A. Strassner, *J. Phys. Chem.*, *39*, 311 (1935).

21. F. Urban and H. L. White, *J. Phys. Chem.*, *36*, 3157 (1932).

22. J. T. Davies and E. K. Rideal, *Interfacial Phenomena*, Academic Press, New York (1963). 2nd ed., Chapter 3

23. G. Schmid, *Z. Elektochem.*, *56*, 181 (1952).

24. R. Schlögl, *Stofftransport durch Membranen*, Dr. Dietrich Steinkopff Verlag, Darmstadt (1964). p.75

25. B. Klump and D. Woermann, *Ber. Bunsenges. Phys. Chem.*, *81*, 92 (1977).

26. Y. Toyoshima, M Yuasa, Y. Kobatake, and H. Fujita, *Trans. Far. Soc.*, *63*, 2803 (1967).

27. W. Drost-Hansen, *Ind. Eng. Chem.*, *61*, 10 (1969).

28. J. A. Schufle, C-T. Huang, and W. Drost-Hansen, *J. Colloid Interface Sci.*, *54*, 184 (1976).

29. S. L. Carnie and D. Y. C. Chan, *J. Chem. Phys.*, *73*, 2949 (1980).

30. J. L. Anderson and J. A. Quinn, *J. Chem Soc., Far. Trans. I*, *68*, 744 (1972).

31. C. P. Bean, "The Physics of Porous Membranes -- Neutral Pores," in *Membranes*, ed. by G. Eisenman, vol. 1, pp. 1-55, Marcel Dekker, New York (1972).

32. J. L. Anderson and W.-H. Koh, *J. Colloid Interface Sci.*, *59*, 149 (1977).

33. A. G. Van der Put and B. H. Bijsterbosch, *J. Colloid Interface Sci.*, *92*, 499 (1983).

34. G. B. Westermann-Clark and C. C. Christoforou, "The Exclusion-Diffusion Potential in Charged Microporous Membranes," submitted for publication (1984).

35. G. Jacazio, R. F. Probstein, A. A. Sonin, and D. Yung, J. Phys. Chem., 76, 4015 (1972).

36. D. R. Briggs, J. Am. Chem. Soc., 50, 2358 (1928).

37. H. A. Abramson, J. Am. Chem. Soc., 50, 390 (1928).

38. W.-H. Koh, J. Colloid Interface Sci., 71, 613 (1979).

39. R. P. Abendroth, J. Phys. Chem., 76, 2547 (1972).

40. W.-H. Koh and J. L. Anderson, AIChE J., 21, 1176 (1975).

41. J. A. Quinn, J. L. Anderson, W. S. Ho, and W. J. Petzny, Biophys. J., 12, 990 (1972).

42. C. L. Baker, Diffusion of Hydrocarbons in Mica Pores, M. S. Thesis, Cornell University (1978).

43. W. D. Munch, The Ultrafiltration of Bovine Serum Albumen, M. S. Thesis, Cornell University (1977).

44. D. M. Malone and J. L. Anderson, AIChE J., 23, 177 (1977).

45. G. B. Westermann-Clark, Ion Transport in Charged Porous Media. Theory and Experiments, Ph. D. Dissertation, Carnegie-Mellon University (1981).

46. G. J. Janz, "Silver-Silver Halide Electrodes," in Reference Electrodes, Theory and Practice, ed. by D. J. G. Ives and G. J. Janz, pp. 179-230, Academic Press, New York (1961).

47. G. B. Westermann-Clark, Studies of Electrokinetic Effects in Mica Membranes, M. S. Thesis, Carnegie-Mellon University (1979).

48. R. G. Bates, Determination of pH, Theory and Practice, John Wiley and Sons, New York (1973). 2nd ed., Chapter 8

49. N. Bjerrum, Kgl. Danske Videnskab. Selskab, 7, 9 (1926).

50. R. L. Kay, D. F. Evans, and M. A. Matesich, "Evaluation of Ion-Solvent Interactions from Transport Properties," in Solute-Solvent Interactions, ed. by J. F. Coetzee and C. D. Ritchie, vol. 2, pp. 105-153, Marcel Dekker, New York (1976).

51. G. J. Janz and R. P. T. Tomkins, Nonaqueous Electrolyte Handbook, vols. 1 and 2, Academic Press, New York (1973).

52. R. M. Fuoss and F. Accascina, Electrolytic Conductance, Interscience Publishers, New York (1959).

53. E. Renard and J. C. Justice, J. Solution Chem., 3, 633 (1974).

54. J. C. Justice, *Electrochim. Acta*, *16*, 701 (1971).

55. G. A. Vidulich, G. P. Cunningham, and R. L. Kay, *J. Solution Chem.*, *2*, 23 (1973).

56. A. G. Van der Put, *Electrokinetic Investigations on the System Polystyrene/Aqueous Electrolyte Solution*, Ph. D. Dissertation, Agricultural University, Wageningen, The Netherlands (1980). English ed., Chapter 4

57. P. C. Hiemenz, *Principles of Colloid and Surface Chemistry*, Marcel Dekker, New York (1977).

58. B. Carnahan, H. A. Luther, and J. O. Wilkes, *Applied Numerical Methods*, John Wiley and Sons, New York (1969).

59. R. A. Robie, P. M. Bethke, and K. M. Beardsley, *Selected X-ray Crystallographic Data, Molar Volumes, and Densities of Minerals and Related Substances*, U.S. Geological Survey Bulletin, No. 1248, U.S. Government Printing Office, Washington, D.C. 20402 (1967).

60. *Guide for Fubricating and Handling Cf-252 Sources*, U.S. Atomic Energy Commission, Savannah River Operations Office, Aiken, South Carolina 29801 (1971).

BIOGRAPHICAL SKETCH

Christoforos C. Christoforou was born on January 20, 1957, in Athens, Greece. He received his degree of Bachelor of Science in Chemical Engineeering from the National Technical University, Athens, Greece, in June 1980. He started his graduate studies at the Chemical Engineering Department of the University of Florida in September 1980. He received his Master of Science degree from the same university in August, 1981.

I certify that I have read this study and that in my opinion it conforms to acceptable standards of scholarly presentation and is fully adequate, in scope and in quality, as a dissertation for the degree of Doctor of Philosophy.

Dinesh O. Shah

Dinesh O. Shah, Chairman
Professor of Chemical Engineering

I certify that I have read this study and that in my opinion it conforms to acceptable standards of scholarly presentation and is fully adequate, in scope and in quality, as a dissertation for the degree of Doctor of Philosophy.

Gerald B. Westermann-Clark

Gerald B. Westermann-Clark, Cochairman
Assistant Professor of Chemical Engineering

I certify that I have read this study and that in my opinion it conforms to acceptable standards of scholarly presentation and is fully adequate, in scope and in quality, as a dissertation for the degree of Doctor of Philosophy.

John P O'Connell

John P. O'Connell
Professor of Chemical Engineering

I certify that I have read this study and that in my opinion it conforms to acceptable standards of scholarly presentation and is fully adequate, in scope and in quality, as a dissertation for the degree of Doctor of Philosophy.

Thieo E Hogen Esch

Thieo E. Hogen Esch
Professor of Chemistry

This dissertation was submitted to the Graduate Faculty of the College of Engineering and to the Graduate School and was accepted as partial fulfillment of the requirements for the degree of Doctor of Philosophy.

May, 1985

Hubert A. Bevis

Dean, College of Engineering

Dean, Graduate School